Modeling Mechanisms of Water Affinity and Condensation on Si-based Surfaces via Experiments and Applications

by

Qian Xing

A Dissertation Presented in Partial Fulfillment
of the Requirements for the Degree
Doctor of Philosophy

Approved April 2011 by the
Graduate Supervisory Committee:

Nicole Herbots, Co-Chair
Robert Culbertson, Co-Chair
Ralph Chamberlin
Michael Treacy
David Smith

ARIZONA STATE UNIVERSITY

May 2011

ABSTRACT

Water affinity and condensation on Si-based surfaces is investigated to address the problem of fogging on silicone intraocular lenses (IOL) during cataract surgery, using Si(100), silica (SiO_2) and polydimethylsiloxane (PDMS) silicone $(SiOC_2H_6)_n$. Condensation is described by two step nucleation and growth where roughness controls heterogeneous nucleation of droplets followed by Ostwald ripening. Wetting on hydrophilic surfaces consists of continuous aqueous films while hydrophobic surfaces exhibit fogging with discrete droplets. Si-based surfaces with wavelength above 200 nm exhibit fogging during condensation. Below 200 nm, surfaces are found to wet during condensation. Water affinity of Si-based surfaces is quantified via the surface free energy (SFE) using Sessile drop contact angle analysis, the Young-Dupré equation, and Van Oss theory. Topography is analyzed using tapping mode atomic force microscopy (TMAFM).

Polymer adsorption and ion beam modification of materials (IBMM) can modify surface topography, composition, and SFE, and alter water affinity of the Si-based surfaces we studied. Wet adsorption of hydroxypropyl methylcellulose (HPMC) $C_{32}H_{60}O_{19}$ with areal densities ranging from 10^{18} atom/cm^2 to 10^{19} atom/cm^2 characterized via Rutherford backscattering spectrometry (RBS), allows for the substrate to adopt the topography of the HPMC film and its hydrophilic properties. The HPMC surface composition maintains a bulk stoichiometric ratio as confirmed by 4.265 MeV $^{12}C(\alpha, \alpha)^{12}C$ and 3.045 MeV $^{16}O(\alpha, \alpha)^{16}O$, and 2.8 MeV He^{++} elastic recoil detection (ERD) of hydrogen. Both PIXE and RBS

methods give comparable areal density results of polymer films on Si(100), silica, and PDMS silicone substrates.

The SFE and topography of PDMS silicone polymers used for IOLs can also be modified by IBMM. IBMM of HPMC cellulose occurs during IBA as well. Damage curves and ERD are shown to characterize surface desorption accurately during IBMM so that ion beam damage can be accounted for during analysis of polymer areal density and composition. IBMM of Si(100)-SiO_2 ordered interfaces also induces changes of SFE, as ions disorder surface atoms. The SFE converges for all surfaces, hydrophobic and hydrophilic, as ions alter electrochemical properties of the surface via atomic and electronic displacements.

ACKNOWLEDGMENTS

The writer gratefully acknowledges the various people who assisted in the research and experience in undertaking this dissertation.

Firstly, special thanks go to my advisors, Dr. Nicole Herbots and Dr. Robert Culbertson who supported me without reserve during the study. I also wish to thank my committee members for their support and encouragement. This includes Dr. Michael Treacy, Dr. David Smith, Dr. Ralph Chamberlin, and Dr. Jose Menendez.

My closest coworkers are here gratefully acknowledged for their help throughout most of the experimental portion of this work, Murdock Hart and Dr. James D. Bradley. I also wish to acknowledge the contributions of David Sell, research undergraduate, in helping to set up the initial condensation experiments, as well as Weisi Song and Shawn Whaley who were involved in initial experimental approaches, and Clarizza Watson who coordinated supplies and equipments.

The following academic professionals are greatly appreciated for their technical assistance, Barry Wilkens and Ken Mossman, both within the Leroy Eyring Center for Solid State Science.

Finally, input, guidance and assistance on the medical issues and testing addressed in this research by Clive Sell MD, and Mark Kwong MD were greatly appreciated.

Support from financial donations from Bausch & Lomb, Associated Retina Consultants, a seed grant from the ASU Emeritus College, royalties from

Intel Corp for patent 6,613,677, donations from SiO2 Associates L.L.C. and SiO2 Nanotech Corp. made this research possible, as did material and supplies donations from Bausch & Lomb, Associated Retina Consultants, Dr. Sell and Dr. Kwong, Oakley Corporation, and Under Armor Corporation.

TABLE OF CONTENTS

Page

CHAPTER Page

CHAPTER Page

CHAPTER Page

CHAPTER Page

APPENDIX

LIST OF TABLES

Table Page

Table Page

LIST OF FIGURES

Figure Page

Figure Page

Figure Page

Figure Page

Figure Page

Figure Page

Figure Page

Figure Page

CHAPTER 1

MOTIVATION, APPROACH, AND OUTLINE

1.1 Dissertation Outline

Chapter 1 introduces the problem of fogging during condensation and the motivation to solve this issue, and initiates discussion on the approach to solve this problem.

Chapter 2 introduces the background on physics of water affinity and condensation, as well as insights in the mechanisms linking water affinity to condensation.

Chapter 3 describes how surfaces and molecular films are prepared, based on the initial model to test the connection of water affinity and condensation, condensation experimental design, and materials used.

The specific experimental methods we used or developed for this work, background, experiment design, and data analysis are then discussed from Chapter 4 to 7.

Chapter 4 describes the ion beam analysis (IBA) methods, RBS, nuclear resonance scattering, and ERD.

Chapter 5 describes IBA method PIXE.

Chapter 6 describes the determination of the SFE from contact angle measurements.

Chapter 7 describes topography characterization by TMAFM.

Chapter 8 presents the results and discussion in light of the problems and goals presented in the introduction.

Finally Chapter 9 summarizes our conclusions and suggestions for future work.

1.2 Motivation for the Need to Understand and Control Water Affinity of Si-Based Surfaces

The hydrophobic or hydrophilic properties of a surface, also known as the surface water affinity, play an integral role in defining and determining its physical and chemical properties. An understanding of water affinity can in turn enable us to modify it and use it in solving problems in science and engineering. Furthermore, such understanding on how to modify and control the water affinity of surfaces can lead to new nanoscale applications. The primary physical systems investigated in this work are,

(a) the water affinity of Si-based surfaces as we specifically studied the progression in chemical inertness of surfaces of elemental silicon (Si), silicon oxides (SiO_2), and PDMS silicone ($SiOC_2H_6$), and

(b) the modification of these Si-based surfaces to control their interaction with bio-compatible, benign molecular adsorbates including, single molecular hydroxylates to form OH-based passivation layers in the form of nanofilms and hydrophilic polymer chains rich in hydroxyl groups such as cellulose, the most common organic compound on earth. This polysaccharide of simple formulation consists of multiple linear chains.

Three direct applications drive the motivation for understanding Si-based surfaces, water affinity and controlling the water condensation behavior,

(a) water affinity and surface modification of PDMS silicone ($SiOC_2H_6$) as applied to IOLs implanted during cataract surgery [1],

(b) surface modification of Si-based surfaces for more broad applications such as visionwear by the application of bio-compatible, benign polymers, specifically from the class of viscoelastic polymers commonly used in eye surgery and eye care including hydroxylated, hydrophilic polysaccharides, specifically HPMC cellulose ($C_{32}H_{60}O_{19}$), and

(c) water affinity and surface modification of Si(100) leading to the nucleation of β-cristobalite (β-SiO_2) interphase layer for semiconductor applications such as high performance MOS gates and wafer bonding [2, 3].

1.2.1 Fogging Problem during Retinal Surgery with PDMS Silicone IOL

Water condensation can obscure an ophthalmological surgeon's critical vision into the patient's eyeball when droplets form at the liquid-air interface of an intraocular implant during retinal surgery. Such surgery on the eye involves removing the vitreous humor so the surgeon can operate on the retina, as shown in the anatomy of the eye depicted in Figure 1. The surgeon's loss of the capability of seeing what he or she is doing in surgery within the eye is catastrophic and can occur after a cataract has been extracted and replaced by an IOL implant.

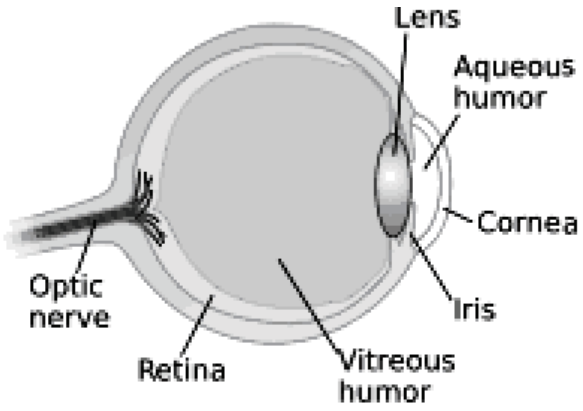

Figure 1.

Anatomy of the eye. Retinal surgery involves the evacuation of the vitreous humor, a clear gel-like substance that gives the eye its shape and support, to repair the retina. The retina is shown above, and is a membrane that encompasses over half of the inside of the eye cavity. When the vitreous humor is evacuated, an inert gas such as SF_6, pioneered by Clive Sell MD, one of our collaborators, replaces it to keep the eye from collapsing. This creates an air-liquid interface with the lens; it is this lens which was removed and replaced with an IOL. The damp, moist environment within the eye can lead to fogging on the IOL, making it impossible for the surgeon to see his progress [4-6]. Figure used with permission in accordance to the GNU Free Document License, V1.2 [7, 8].

Figure 2, Figure 3, and Figure 4 illustrate how this problem occurs. Figure 2(a) shows the schematic anatomy of an eye with a diseased lens being removed and Figure 2(b) shows the diseased lens being replaced by an IOL. Figure 3 shows an artificial PDMS silicone IOL, one of several types investigated and used in this work as a model hydrophobic PDMS silicone surface due to its optical

perfection. It is artificial lenses such as these that are implanted to replace the natural lens during cataract surgery.

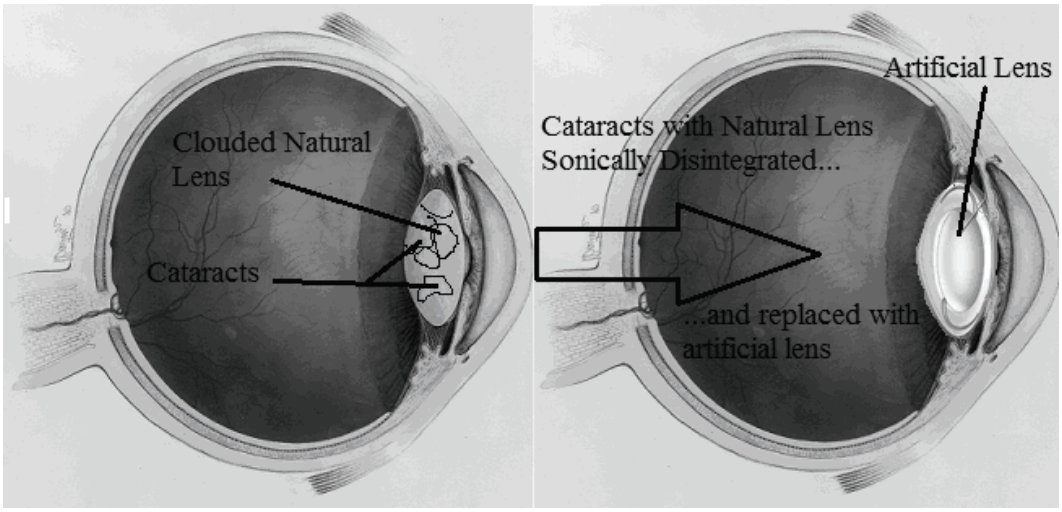

(a) (b)

Figure 2.

(a) The natural lens is removed via the ubiquitous, so-called "phacoemulsification" procedure: it consists of sonically disintegrating the cataract, and the hardened natural lens in the process and (b) An IOL is placed in its stead. Figure of eye use granted by the National Eye Institute, a division of the National Institute of Health under Public Domain Use: Ref#: NEA04 [9, 10]

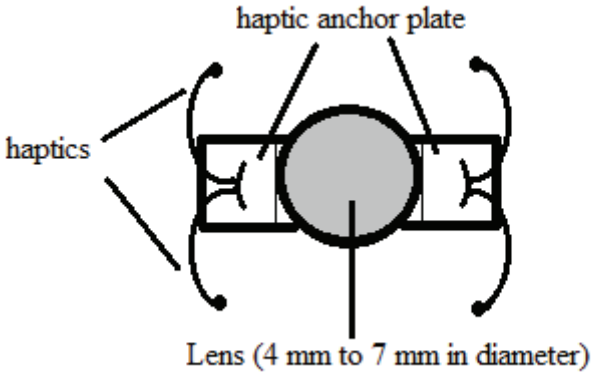

Figure 3.

One type of PDMS silicone IOL used to replace the diseased natural lens during cataract surgery, and used in the present work as condensation studies material. The circular lens disk, made from high purity, optical quality material, has a diameter ranging from 4 mm to 7 mm depending on the dimensions of a patient eye. It is anchored via the so-called “haptic-anchor-plate” with the mini-loops that are the haptics. Such IOL combines the lens with a pair of plates and loops to eliminate the risk of vitreous dislocation and to anchor the IOLs in the iris’ zonules. Zonules are muscles focusing natural eye lenses by increasing or decreasing its curvature. Anchoring enables the eye to focus the flexible IOL, resulting in what is called an accommodating lens, instead of fixed focus. The haptics were used in the present work to suspend the lens above the artificial eye cavity.

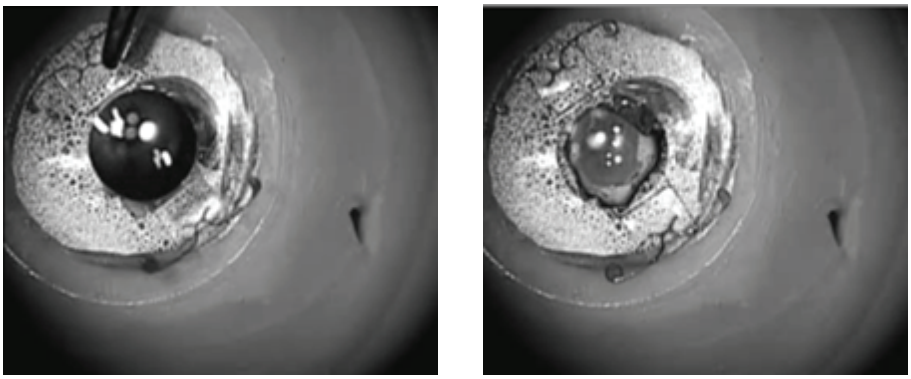

(a) (b)

Figure 4.

The severity of the problem when fogging occurs during condensation. (a) shows an IOL placed within 1 second onto an artificial eye partially filled with water heated to 38 °C to simulate the moist conditions within a real eye during retinal surgery, (b) shows fogging occurring after only 3 seconds of time elapsed from (a). Most surgeons describe it as instantaneous. As the lens is the only window into the eye which the eye surgeon can use to conduct his or her repairs of the retina, a fogged lens has a catastrophic impact and prevents the surgeon from effectively repairing the retina.

1.2.2 Reproduction of Fogging during Water Condensation on PDMS Silicone IOL

Figure 4 demonstrates the problem of fogging during condensation experiments in the present work completed on artificial eyes used for practice to train retinal surgeons on actual, surgical grade PDMS silicone IOLs. These experiments were conducted in collaboration with Associated Retina Consultants, Clive Sell, MD and H. M. Kwong, MD, who provided among other contributions the artificial eyes and implant grade IOLs. We reproduced in the laboratory and in

the doctors' operating room the phenomena of fogging, see Figure 4(a) and (b), to mimic the conditions during surgery (temperature, humidity, salinity, sterility) in order to study the physics of the problem, design a solution, and ensure a straightforward transfer of our findings back to the surgery environment. The latter ensured that the new understanding we developed in this work on water affinity mechanisms on Si-based surfaces and the solutions we derived from it were easily used in the medical field.

1.2.3 Impact and Scope of the Problem

The pictures taken of an artificial eye with an IOL as shown in Figure 4(b) shows how opaque the lens becomes due to condensation and subsequent fogging during surgery, and illustrates the striking loss of vision in conditions simulating retinal surgery on a commonly used PDMS silicone IOL. These specific PDMS silicone IOLs include about 30% of the PDMS silicone IOLs used in the US, where cataract removal is the most common surgery, and 3 million IOLs are inserted in aging or diseased eyes every year. This problem is not just restricted to PDMS silicone IOLs. These hydrophobic acrylic lenses are the latest accommodating lens approved by the federal food and drug administration in 2010 for cataract surgery. The key point highlighted in Figure 4(b) about the condensation problem during surgery is that, it is getting more and more common as more and more IOLs are implanted and the population ages. It is also not limited to one single type of material, but closely related to the hydrophobic character of these popular ocular implants.

The occurrence of fogging potentially manifesting itself during retinal surgery is ubiquitous. To put this issue in perspective, it can potentially affect any person who undergoes one or two of the 15 million cataract surgeries done annually throughout the world and subsequently receive the IOL which replaces removed natural lens. Roughly 25% of the IOL recipients eventually experience the development of "secondary cataract", when the sack that contained the natural lens (and now the IOL) begins to cloud. This is called "posterior capsular opacification" [11]. The solution to posterior capsular opacification requires a generally simple yet prolific procedure, YAG (Nd:YAG or neodymium-doped yttrium aluminum garnet; Nd:Y3Al5O12) laser surgery, where the laser is used to disintegrate the clouded part of the sack on the inner side of the eye. This surgery involves making a hole in the natural skin sack holding the eye lens and thus results in the artificial IOL being directly exposed to the vitreous humor (see Figure 1). 3.7 million YAG surgeries are conducted annually in the world. This procedure is the second highest Medicare reimbursement category after cataract surgery itself [12]. Unfortunately more than 1 in 50, or at least 2% of these YAG patients ultimately go on to require, for various reasons, subsequent retinal detachment surgery, by far the most common category for retinal surgery [13]. A 2% rate of retinal surgery results in 75,000 patients among the 3.7 millions per year YAG patients directly affected by the issue of condensation.

The study of fogging during water condensation at the well defined air-water interface of PDMS silicone ($SiOC_2H_6$) ocular implants during eye microsurgery naturally carries implications to water condensation on many types

of visionwear such as sports visors, eye glasses, goggles etc. Developing anti-fogging properties is a key interest in both science and engineering, based on the plethora of applications and products on the market and the research devoted to the prevention of condensation in sports and high technology.

1.3 Approaches and Backgrounds

1.3.1 Concept of Wetting Instead of Fogging during Condensation

The first step in fundamentally solving this medical problem is to describe and control the mechanism leading to fogging during condensation. In the introductory phase of this research, the key physical model we established describes the two steps leading to opacification: condensation of water vapor from moist tissue evaporation occurs on all surfaces during surgery; condensation on any surface either result in wetting or fogging during condensation depending on whether a continuous film is formed by water molecules interacting with a surface, which thus has to be hydrophilic surface; or individual droplets are nucleated and grow larger as more water molecules condense and interact with each other in a surface that has to be then hydrophobic. Further experiments to develop methods to render a hydrophobic surface hydrophilic will demonstrate that this is indeed the case, and that all truly hydrophobic surfaces exhibit fogging during condensation, and thus become opaque during surgery, while all truly hydrophilic exhibit complete wetting during condensation and remain transparent.

It is important to note that prior to this investigation, the PDMS silicone IOL fogging problem had not been fundamentally resolved. This problem has been pervasive for at least 15 years, as noted by the various ophthalmology

journal articles describing this problem [4-6, 14-16]. Furthermore, there is no comprehensive solution, again noted by the descriptions written about the problem, the attempted solutions, and the wide time frames these article have been written [4-6, 14-16]. Solutions have ranged from continuously wiping the condensation off of the IOL during surgery, considered very ineffective on the PDMS silicone IOLs, to applying a thick viscoelastic on the IOL during surgery, which increased the distortion of the retinal view and therefore was not effective for the surgeon [15]. Other solutions including increasing the temperature of the in the anterior of the eye (where the fluid-gas exchange takes place) to reduce the condensation on the IOL, and heat the irrigating solution used to moisten the eye during the surgery [16]. Both had limited effect, primarily because of the very specific and constrained environment in which the fogging is occurring during condensation, one cannot apply much heat when the human body is involved. Thus, to this day, there is no comprehensive solution that fundamentally resolves the IOL fogging problem during condensation.

1.3.2 Surface Modification Background

Understanding the properties that create this behavior on the surface is part of this investigation. Hence the physics of the problem is relevant to cataract and retinal surgery in general. Therefore, the issue of understanding condensation and controlling the fogging during retinal surgery is a key motivation for our study of Si-based surfaces of water affinity [4-6].

Examples of surface modification to change the surface properties include the application of a dual layer of nanoparticles composed of silicon and titanium

oxides that was engineered to resist condensation by making the surface more adsorbant and hydrophilic [17]. Super-hydrophobic (also labeled ultra-hydrophobic) surfaces have also been studied extensively for their water repellent characteristics [18]. Yet, studies have determined that the ultra-hydrophilic behavior of the surface in and of itself does not guarantee that its interaction with a liquid can be predicted [19]. While the free energy of a surface is clearly related to how a solution interacts with that surface [20], the combined effects of both SFE and its topography at the nanoscale level still needs to be understood. It is based on the nanophase, interphase, and nanofilm models and the expertise in designing and nucleating such nanophases, interphases, and films built in our combined ion and molecular deposition research group, class 100 clean rooms and our recently upgraded bio-safe laboratory. Previous work and observations in the research group on simple elemental Si and SiO_2 polymorphs and their water affinity for semiconductor applications provided insight into the present bio-medical research via a decade and a half of PhD theses [21-24]. To conduct the present research, this work built first on the models and experimental methods previously developed. The present work extended them and developed them further to manipulate the water affinity of the surface of PDMS silicone compounds (e.g. $SiOC_2H_6$) and brought our laboratory to bio-safety standards as well as new cleanroom processing standards.

1.3.3 Surface Modification via Wet Chemical Clean

Semiconductor devices, in particular MOSFET devices, are dependent on the microscopic configuration of the interface between silicon and silicon oxide

(also known as the Si(100)-SiO_2 interphase) in determining the efficiency and effectiveness of both electronic and optical operations. In particular, the silicon and silicon oxide interface (annotated here Si(100)-SiO_2 interface) is critical in order to control a variety of electrical parameters of operations, such as the fixed oxide charge and the carrier mobility [25]. In our previous experiments to planarize and passivate the Si(100)-SiO_2 interface, a modified RCA clean denoted as the Herbots-Atluri clean was developed, patented (2003) and licensed to Intel (2005) [26].

The Herbots-Atluri clean flattens the silicon surface and decreases the steps and terrace density at the nanoscale level over extended regions of several tens of nm, an order of magnitude greater in scale compared to a conventional RCA clean. It nucleates an OH terminated passivation to the silicon surface, creating a highly stable, inert surface that resists the formation of a native oxide [27]. Furthermore, the resultant surface allows for the growth of a new nanophase, a β-cristobalite epitaxial silicon oxide which extends 2 nm from the silicon surface. This was determined through matching experiment results with modeling of β-cristobalite on Si(100) [28-30]. This new nanophase, stable between OH(1x1)-Si(100) and amorphous Si(100) was recently patented and is called there an interphase, given its thickness of 2 nm [2].

Silicon surface cleaning processes and interfacial thin film nucleation are critical to the semiconductor industry, and the Herbots-Atluri clean directly affects the water affinity and SFE of the silicon at each step of the clean. Hence understanding the water affinity and surface modification behavior of silicon is a

second motivation for this work. Figure 5 is a step by step description of the Herbots-Atluri clean.

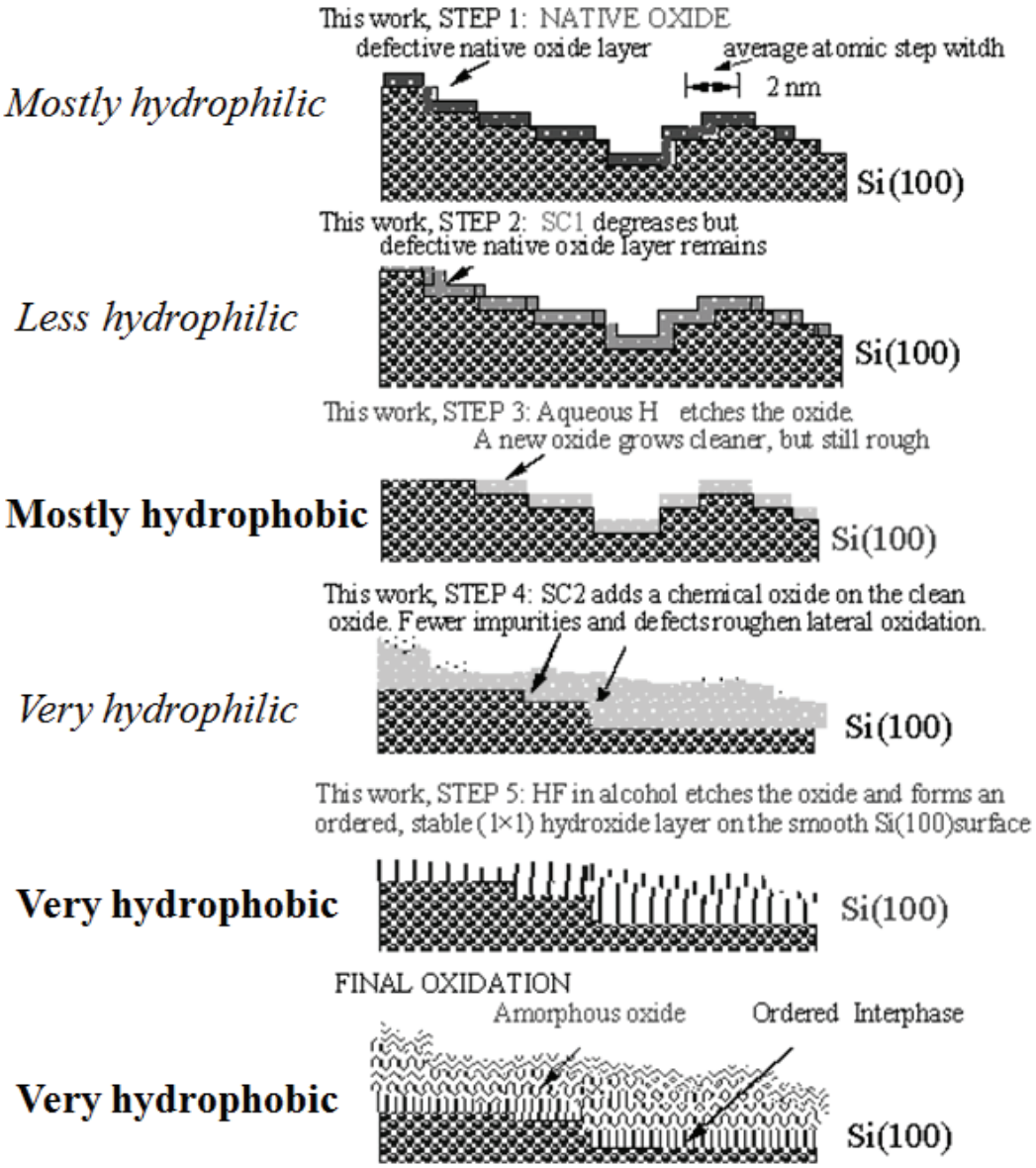

Figure 5.

Physical and chemical descriptions of the processing steps for the Herbots-Atluri clean.

One of the uses for the Herbots-Atluri clean is to clean and smoothing Si(100) wafers. After each step is a DI water rinse. Step one, above is the initial

state of the wafer upon receiving it. The surface will have a varying degree of contaminants and a defective native oxide layer. Step two dips the Si(100) wafer in an SC1 solution composed of $NH_4OH:H_2O_2:H_2O$ (1:1:4), which removes organics and hydrocarbons (i.e. a degreaser). Step three is initiated as a 60 second dip into aqueous 2% HF solution, which strips the defective native oxide off of the wafer. In step 4, the wafer is dipped into an SC2 solution composed of $HCl:H_2O_2:H_2O$ (1:1:4) which removes metallic contaminants and grows a fresh, chemical oxide layer on the surface. Step five is the final etch and passivation and involves dipping the wafer for 60 seconds into an HF (49%):CH_3OH (1:10) solution and then rinsing in methanol to passivate the surface. After this final step the surface is hydrophobic.

As the silicon surface undergoes the Herbots-Atluri clean, the silicon surface is modified, generally decreasing its SFE state with higher water affinity to a lower SFE state with a lower water affinity. This occurs as defects, impurities and defective layers are effectively etched. The increase in surface chemical homogeneity and reduction in defects and surface step density reduces the SFE. The termination of the surface silicon's dangling bonds with a hydroxyl group, leads to an inert, passivated, smoother silicon surface which is much less reactive than the initial silicon wafer surface. Previous research in our group has used a variety of surface characterization techniques which provided evidence that a new ordered β-cristobalite nanophase is formed. Surface and interphase analysis includes reflective high energy electron diffraction; high resolution transmission electron microscopy showed atomic terrace formation from every 2 nm

(conventional oxide) to extending to 20 nm due to the Herbots-Atluri clean [27]; Fourier Transform Infra-Red Spectroscopy, which detected a uniform, stable and unique absorption line with a single red shift in Si-O bond configuration through the 1 nm interface between the silicon and the new silicon oxide interphase nucleated on the Herbots-Atluri cleaned samples only [31]; ion IBA detected alignment and shadowing between silicon atoms in the Si(100) and the silicon atoms in the ordered silicon oxide through 2 nm of silicon dioxide before the 2 nm interphase is continued by an amorphous silicon dioxide [32].

As noted in the above applications, surface preparation is critical, and the present work has for the first time quantified the SFE on three types of samples generated by the Herbots-Atluri clean: as-received wafers, passivated wafers processed via the Herbots-Atluri clean and annealed wafers processed via the Herbots-Atluri clean, then annealed at 200 °C. These experiments provided not only a further quantitative characterization of hydrophilic and hydrophobic elemental Si(100) and SiO_2 surfaces of the Herbots-Atluri clean, but also a useful comparison to PDMS silicone surfaces and other SiO_2 polymorphs surfaces such as quartz silica and commercial silicate film glasses such as those found on eyeglasses. Furthermore, IBMM on these surfaces was researched and used as a probe to determine the relationship between the SFE and the ordering of the precursor of the interphase layer and how the SFE is modified as a result of disordering by IBMM.

1.3.4 Surface Modification via HPMC Cellulose Adsorption

Applying polymers to surfaces with the intent to alter the surface chemistry is well known and utilized for a variety of purposes. Porous polymer coatings have been used to create super-hydrophobic surfaces [33], while IOLs have been improved with surface modifications via PEG (poly(ethylene glycol)) [34]. The pharmaceutical industry extensively uses polymer coatings for drug delivery [35]. Polymer adsorption on surfaces is known to alter the surface chemistry [36].

To inhibit condensation on PDMS silicone IOLs that lead to fogging and the subsequent loss of the surgeon's ability to see during retinal surgery, the challenge is to modify the surface in the severely restricted and limited chemical environment of the human body, the IOL was implanted in the eye of a patient and cannot be removed nor can the saline solutions of tears, human tissues and humors such as the lipid films protecting eye, skin and cell membranes be even slightly affected. Also, most visionwear applications require an approach totally benign for human eye and skin tissues. Eye tissues have in fact the tightest pH requirements of all human tissue, ranging between 7.2 and 7.4, while saline solutions and tears have a well defined range of electrolyte composition as well. Hence the tight chemical control of the environment and the surface of the implanted lens during eye surgery provide well defined, similar conditions to study condensation for many, more general visionwear applications.

Hence, the present work focuses experiments and modeling on, polymer adsorption on PDMS silicone surfaces and how an alternative polymer layer alters

the surface topography and water affinity of the original PDMS silicone surface to affect water nucleation and condensation behaviors, specifically, this work investigates how the application of HPMC alters the surface topography and water affinity of the PDMS silicone surface as applied to PDMS silicone IOLs in an effort to prevent fogging during retinal surgery.

1.3.5 Surface Modification via IBMM

IBMM is also known to change the surface characteristics of polymers [37] as well as other surfaces [38]. Changes in the surface properties such as water condensation behavior were observed after ion beam exposure. Along with color changes of the respective surface, these changes indicate composition and structural changes to both the PDMS silicone IOLs and HPMC cellulose film have occurred. Furthermore, IBMM of polymers is also known to be affected by ion beam energy and flux density [39]. In particular, polyimide, (a combination of C double bonded with O, N, and H), which among other applications, is used in the semiconductor industry as a method to transfer the masking to the silicon, was analyzed using ERD and RBS simultaneously to ascertain the radiation damage this polymer experienced [40]. Additionally, HPMC cellulose was modified using electron beam irradiation [41]. IBMM of Si-based surfaces and polymers' water affinity change will be characterized in this work.

CHAPTER 2

PHYSICS OF WATER AFFINITY AND CONDENSATION, AND ITS APPLICATIONS TO SI-BASED SURFACES

A surface's hydrophobic or hydrophilic behavior can be described by how the electronic configurations of both the interacting surface and water molecules interact at the nanoscale level. At a more macroscopic scale, an understanding of how an entire surface interacts with a liquid can be described via the SFE and surface tension of the liquid. The SFE includes both the polar and apolar contributions of the molecules composing the surface. The SFE and the surface tension are thermodynamic quantities averaging the multiple microscopic interactions that can be identified at the nanoscale level.

Both microscopic and macroscopic descriptions are needed to gain insight into modeling and controlling hydrophilic and hydrophobic behaviors, and to manipulate experimentally and characterize these properties. Modeling at both scales helps separate the different properties of the surface and the liquid leading to a specific behavior.

2.1 Lifshitz-van der Waals Interaction

2.1.1 Microscopic Mechanism of Intermolecular Force

2.1.1.1 Polar and Apolar Molecules

The polar moment of a molecule is the result of the charge localization and separation in the electronic clouds distribution. The spatial distribution can yield a dipole or multipolar moment, of which we will focus only on the dipole while acknowledging the possibility and existence of higher order moments. Polar

molecules then interact with each other through dipole-dipole intermolecular forces. The polarity of a molecule depends on the difference in electro-negativity between constituent atoms, and the asymmetry of the molecule's electronic distribution [42]. Figure 6(a) and (b) show a hydrogen fluoride (HF) molecule with (a) the highly electronegative fluorine in darker shade and (b) the resulting qualitative local charge distribution, with the shaded area around the "-" being the negative charge bias and the shaded area around the "+" being the positive charge bias. The net dipole moment of HF is 6.38×10^{-30} C m. The water molecule, H_2O, has a relatively localized charge distribution shown in Figure 6(c) yielding a significant polar moment of 6.18×10^{-30} C m due to the asymmetric arrangement of the hydrogen atoms relative to the oxygen atom.

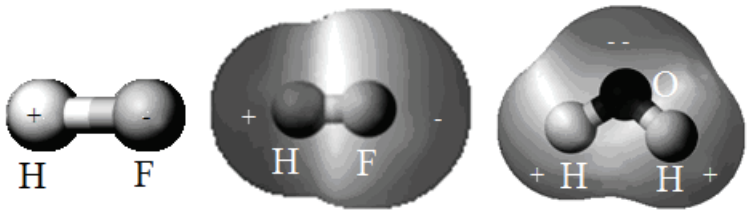

(a) HF (b) HF dipole (c) H_2O dipole

Figure 6.

The hydrogen fluorine (HF) molecule is highly polar. (a) shows the highly electronegative fluorine atom, (b) shows the relative local charge distribution, with darker gray representing the local polarized charges, (c) shows water (H_2O) being a polar molecule due to the asymmetric arrangement of the two hydrogen atoms relative to the oxygen atom.

Conversely, molecules that are electronically balanced, either through atomic symmetry or equivalent electro-negativity (such as the oxygen molecule, O_2) are apolar and thus do not exhibit a dipole moment. Figure 7(a) shows the localized electronic charge distribution of the symmetric atomic configuration of boron trifluoride, while Figure 7(b) is methane, representative of hydrocarbons, also an apolar molecule.

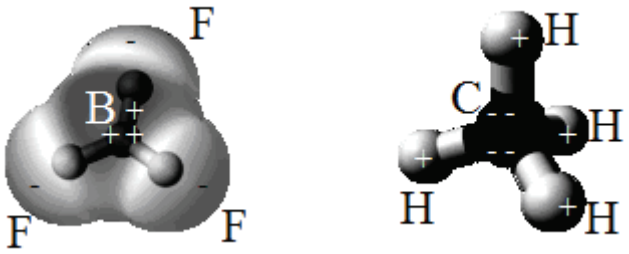

(a) BF_3 (b) CH_4

Figure 7.

Both apolar molecules (a) boron trifluoride and (b) methane, a hydrocarbon, exhibit a configurationally atomic symmetry so that the positive and negative centers of charges coincide. The electronic cloud distribution is balanced charge-wise and thus spherically symmetrical.

2.1.1.2 Polarity, Polarizability, and Dispersion Effects

Generally known as the van der Waals force, this intermolecular force is weak and describes how molecules can interact with each other regardless of their possessing a dipole moment [43-46]. The van der Waals force was determined to have three contributions [47].

First, a randomly orienting permanent dipole-permanent dipole interaction between two molecules was described by Keesom in the 1920's [47-49]. In this

case, each molecule possessed its own permanent dipole, which then interacts with the permanent dipole possessed by another molecule.

Second, a randomly orienting permanent dipole-induced dipole interaction was introduced by Debye at around the same time period [47, 50, 51]. In this case, molecule 1 possesses a permanent dipole, which induces a dipole in an apolar molecule 2 and induces a dipole on molecule 2. Thus, the polarity of a polar molecule combined with the polarizability of an apolar molecule results in an interaction.

The third contribution to the van der Waals force was the fluctuating dipole-induced dipole (dispersion) interactions, described by London nearly a decade later [43, 47]. The so-called London interaction is applicable to molecules that are neutral and therefore lack a permanent dipole moment. However, even a symmetrical, electro-negatively balanced molecule is neutral only on average. At any moment, the electronic configuration when captured as an instantaneous snapshot will show some spatial separation between its positive and negative charge distribution. This effect results in a location and time dependent charge separation and thus generates a dispersion force.

All three interaction energies between molecules decay quickly with distance between molecules. Of the above three components of intermolecular interactions, only London dispersion interaction prevails macroscopically in the condensed matter [47].

2.1.2 Macroscopic Mechanism of Intermolecular Force

Hamaker took an approach of pair-wise summation of the microscopic London dispersion forces theoretically and provided a long range interaction model for the macroscopic materials. The change of free energy ΔG is in terms of total attractive dispersion energies [52, 53]. To describe the van der Waals-London interaction, Hamaker looked at each pair of interacting molecules and determined their dispersion interaction via Hamake constant [52]. The surface tension (or SFE per unit area) γ, when dominated by the London dispersion forces, such as γ of n-alkanes, can now be related to the Hamaker constant through the work of cohesion $W = 2\gamma$ [54].

Lifshitz described another approach on macroscopic dispersion interaction. He used theory of quantum mechanics and electric magnetic fields subject to rapid time dependent fluctuations, and started out in a macroscopic framework [46, 55]. The subsequent development of this approach introduced the interfacial Lifshitz-van der Waals (LW) interactions, which included the interactions between apolar materials, leading to the explicit capability to derive the free energy change ΔG in terms of macroscopic properties such as dielectric constants or refractive indexes [56]. The Lifshitz approach is found to be more accurate compared to the Hamaker model, as it does not ignore the repulsive component as did in the Hamaker model. The derivation of Lifshitz model is beyond the scope of this work. Therefore, only the results are mentioned here.

The free energy change ΔG in the Lifshitz model is interpreted in terms of $\Delta G_{ii}^{LW} = -2\gamma_i^{LW}$ for surface type i. This can be viewed as the free energy

change is the energy required to create two separate surfaces from the bulk, each has increased surface energy with respect to the bulk (see Figure 8).

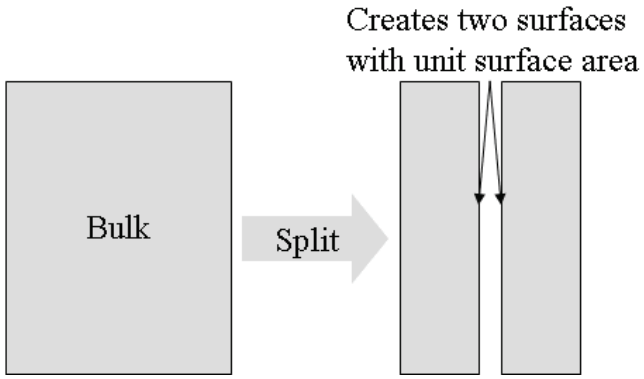

Figure 8.

Concept diagram showing free energy can be described as the energy required to create two surfaces.

Interfacial Lifshitz-van der Waals dispersion interactions between two condensed matter types i and j are given by the Dupré equation. The free energy change $\Delta G_{ij}^{LW} = \gamma_{ij}^{LW} - \gamma_i^{LW} - \gamma_j^{LW}$, where γ_{ij}^{LW} is the surface tension between surface types i and j and $\gamma_{i,j}^{LW}$ is the surface tension for surface types i and j respectively [57]. This can be viewed as when both surfaces are separate, the system has a free energy with respect to the bulk in the amount of $\gamma_i^{LW} + \gamma_j^{LW}$, and then γ_{ij}^{LW} can thus be interpreted as the reduction of surface tension once the surface are in contact. It is further shown that $\gamma_{ij}^{LW} = \left(\sqrt{\gamma_i^{LW}} - \sqrt{\gamma_j^{LW}}\right)^2$ [58, 59], therefore we now have $\Delta G_{ij}^{LW} = -2\sqrt{\gamma_i^{LW}\gamma_j^{LW}}$.

2.2 Acid Base Interaction

While the Lifshitz-van der Waals model describes the dispersive apolar portion of the interfacial interactions, more recent studies in thermodynamics of interfacial tension between a solid and liquid have shown that polar interactions have significant impact on interfacial interactions. One example is the interaction between proton donors (Bronsted acids) and proton acceptors (Bronsted bases) of the Bronsted model. A second example is the hydrogen bond when it is used as a model to describe the hydrogen atom's interaction with an electronegative atom as shown in Figure 9[52, 60-62].

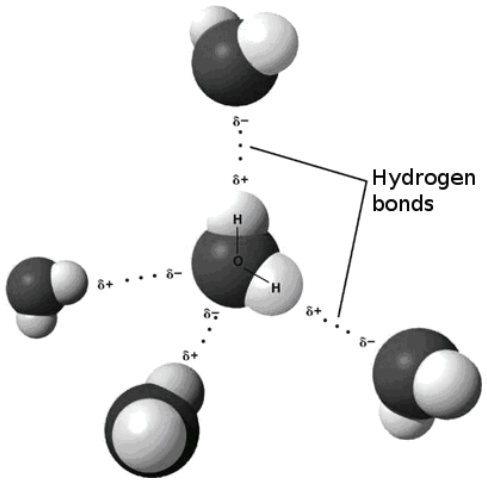

Figure 9.

Water molecules interact with each other as electric dipoles, by aligning their opposite charges in a three dimensional spherical spatial configuration. Figure used with permission in accordance to the GNU Free Document License, V1.2 [8, 62].

Van Oss showed that the interaction between an electron pair acceptor (Lewis acid) and electron pair donor (Lewis base) is asymmetrical. The change of

free energy based on the acid base (AB) model is $\Delta G_{ij}^{AB} = -2\sqrt{\gamma_i^+ \gamma_j^-} - 2\sqrt{\gamma_j^+ \gamma_i^-}$ where $\gamma_{i,j}^+$ is the Lewis acid component for surface types i and j respectively, while $\gamma_{i,j}^-$ is the Lewis base component of the surface tension for surface types i and j respectively. Note that when $i = j$, then $\Delta G_{ii}^{AB} = -4\sqrt{\gamma_i^+ \gamma_i^-}$.

2.3 Van Oss Theory and SFE

Combining the Lifshitz-van der Waals apolar dispersion interaction with the Lewis acid base polar interaction, the total free energy change of surface types i and j becomes $\Delta G_{ij} = \Delta G_{ij}^{LW} + \Delta G_{ij}^{AB}$. Thus we have the following mathematical expression in the model proposed by Van Oss [52, 53, 63],

$$\begin{cases} \gamma_i = \gamma_i^{LW} + 2\sqrt{\gamma_i^+ \gamma_i^-} \\ \gamma_{ij} = \left(\sqrt{\gamma_i^{LW}} - \sqrt{\gamma_j^{LW}}\right)^2 + 2\left(\sqrt{\gamma_i^+} - \sqrt{\gamma_j^+}\right)\left(\sqrt{\gamma_i^-} - \sqrt{\gamma_j^-}\right) \end{cases} \quad (1)$$

In summary, the total free energy change, or surface free energy (SFE) is derived from the intermolecular interaction concept. In this work, both the Lifshitz-van der Waals apolar dispersion component and the Lewis acid base polar component are considered. Note that, as stated before, surface tension is SFE per unit area, but will refer both as SFE. The contact angle method used in this work to characterize SFE will be discussed later in Chapter 6.

2.4 SFE and Water Affinity

The interaction between a macroscopic surface and a water film or droplet can thus be described by taking into account the intermolecular mechanisms of interaction.

If molecular interactions between the water molecules are stronger than the water's interactions with surface molecules, then the surface has less relative influence on the water and the surface is hydrophobic. Hence, liquid water interacts primarily with itself, with significant curvature if they are confined to droplets or thin films. This is due to the water molecules at the surface of the droplets creating a contact edge with the hydrophobic surface by pulling away from the surface. This effect leads to the definition of "contact angle" between the water droplets and the surface, where this angle is greater than 90° [64-66]. The water surface exhibits a significant curvature projecting away from the surface, which scales with the balance between the magnitude of the water-water interaction and the water-surface interaction, as shown in Figure 10.

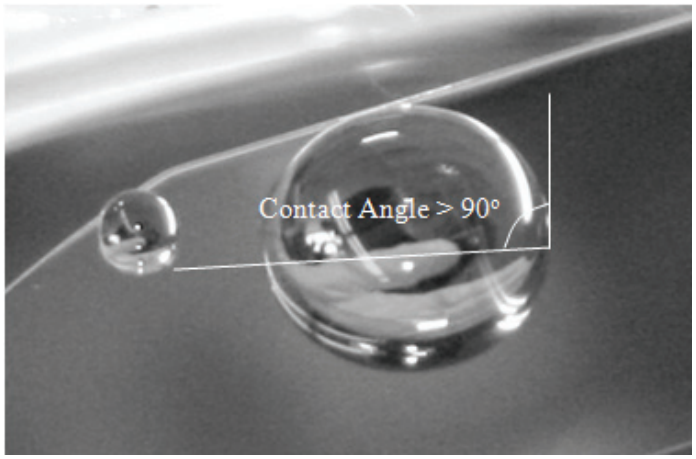

Figure 10.

A water droplet interacts with a hydrophobic surface, by curving its surface at the contact interface, yielding a contact angle between the surface, Si(100), and the water drop surface that is larger than 90°.

The interaction between hydrophilic surfaces with pure water is quite different. A hydrophilic surface's interactions with the water molecules exhibits a

larger magnitude than that of the water molecules interaction with themselves. The resulting surface-water interaction at the contact interface causes the water molecules to adhere close to surface, thus reducing the contact angle of a hydrophilic surface to less than 90° [64-66]. The more hydrophilic the surface is, the greater the magnitude of the interaction between the water molecules and the surface relative to the water molecule to water molecule interactions. Hence the contact angle decreases as the surface hydrophilic behavior increases. Figure 11 demonstrates a highly hydrophilic surface consisting of a rough surface of thermal oxide on the unpolished back side of a Si(100) wafer.

A material's surface water affinity and the mechanism of interaction with water can be related to the SFE possessed by the material. Defects such as dangling bonds and contaminants render any surface, such as the apolar, elemental and covalently bonded Si(100) surface, hydrophilic. One can simply link this behavior to the SFE averaging the intermolecular interaction between water molecules and the solid surfaces [65, 66]. Cleaning to remove contaminants will change the silicon's water affinity from hydrophilic to hydrophobic, but requires a precise, step by step recipe, such as the Herbots-Atluri clean noted in Chapter 1. Etching to smooth the surface and reduce defects, and passivation with apolar surface molecules of a cleaved Si crystal can lower SFE, leading to a hydrophobic behavior of the surface. Each step of the clean has the goal to lower the SFE of the silicon surface, either by directly removing the contaminants such as metals, which create a highly localized hydrophilic behavior, or by removing hydrocarbons which tend to mask the underlying silicon surface from etching or

reactive agents, and thus prevent any cleaning actions to this specific silicon surface region, or by stripping off the inevitable native oxide layer, again, shielding the silicon surface from further cleansing and smoothening.

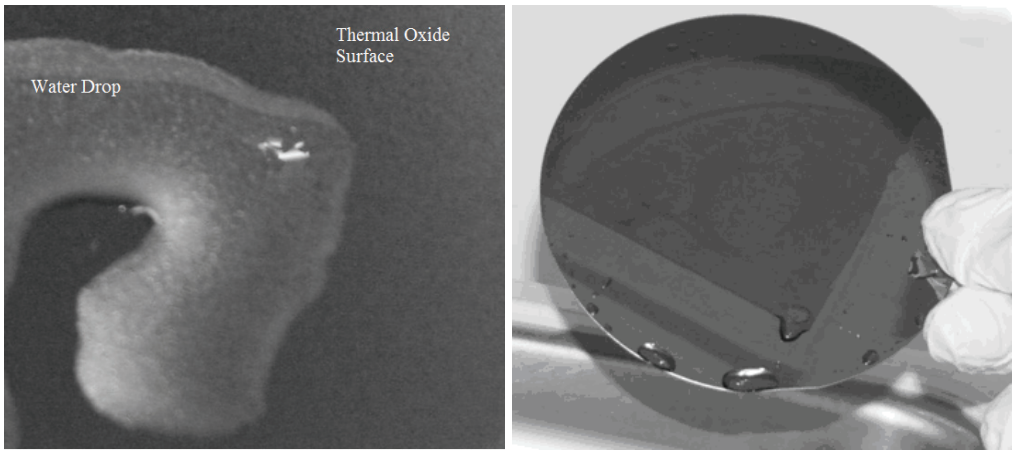

(a) (b)

Figure 11.

In (a), a water "drop" interacts on a strongly hydrophilic surface, a rough thermal oxide grown on the unpolished backside of a Si(100) wafer. The water-surface interaction is much greater than that of the water-water interaction, and thus the contact angle is much less than 90°. In (b), the darker pie shaped region of a Si(100) wafer has completely wetted, indicating its hydrophilic nature, while the outer portions of the same wafer cause any water to bead up, indicating a hydrophobic nature.

Once the Herbots-Atluri clean was fully applied to the silicon surface, the surface which was initially hydrophilic with metallic and hydrocarbon contaminants, and a rough, defective native oxide layer, is now topographically smoother by an order of magnitude, and free of contaminants [27]. Its dangling

bonds are passivated, and it has become hydrophobic in nature due to the lowering of the SFE.

Figure 12 shows that the same Si(100) surface can exhibit a stark difference in water affinity depending on whether the surface was terminated by a passivated molecular layer that renders it hydrophobic, or not. The contact angles of the water droplets detecting the degree of water affinity are shown in Figure 12(b). The picture taken in profile of the wafer showed face first in Figure 12(b) highlights the radical difference in water affinity between the upper hydrophilic and the lower hydrophobic regions of a polished Si(100) wafer.

As Figure 12(a) shows, a strongly defined boundary was created between the two regions via a passivating molecular film and is shown by the well defined, sharp boundary between the wet and the dry region created by a wet chemical treatment and masking.

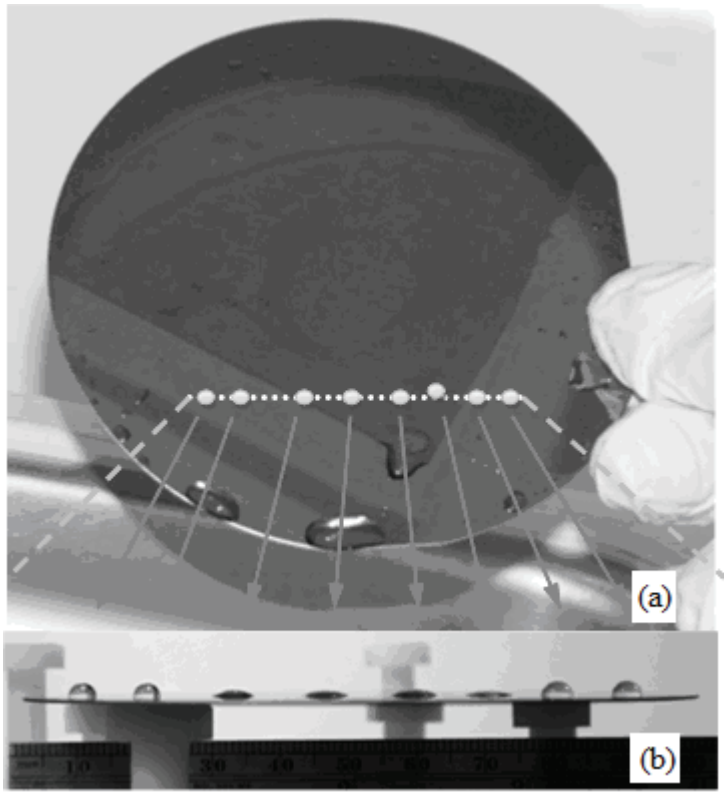

Figure 12.

A Si(100) polished wafer with an area of higher SFE (within the darker, wetted triangle shape) due to contaminants and dangling bonds that renders the surface more hydrophilic, while a passivation molecular layer (the lighter grey, dry area outside the triangle) renders the surface hydrophobic.

2.5 The Role of Water Affinity in the Applications of Interest

Water affinity and condensation behavior of surfaces are of interdisciplinary interest across physics, material science, engineering, and medical applications [4-25]. Understanding the water affinity and condensation behavior of the surface has practical implications in understanding the interactions of two independent surfaces, such as the bonding of Si(100) and SiO_2 surfaces at the atomic level. The Si(100) surface is passivated and therefore inert and of a

hydrophobic nature. Thermal oxide (SiO_2) surface can be reactive if deficient in oxygen and therefore hydrophilic in nature. By bringing such two surfaces together, a chemical bond between the two surfaces can be formed. Figure 13 is a conceptualization of the bonded pair, with a β-cristobalite structured interphase linking the Si(100) surface with the amorphous silicon oxide surface [28-30].

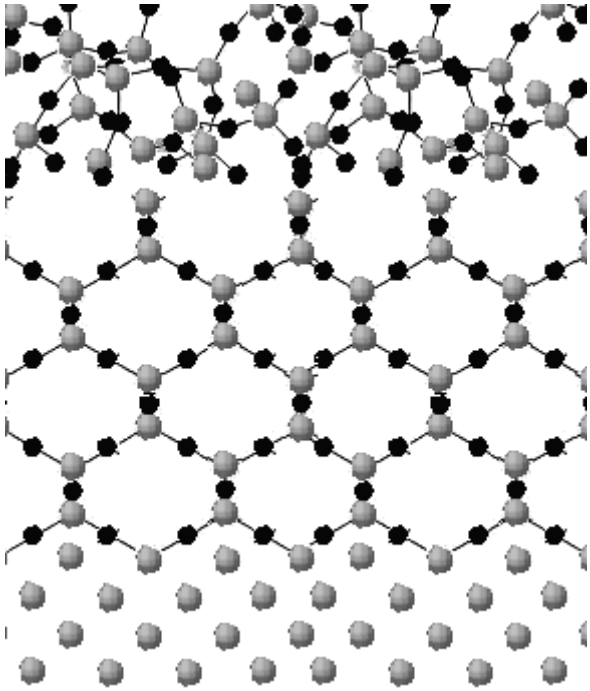

Figure 13.

Conceptual diagram of the cross section of crystalline Si(100), a β-cristobalite nanophase, and an amorphous silicon oxide layer (such a thermal oxide), bonded together by cross-bridging nanobonds. The smaller balls represent oxygen atoms, the larger balls identify silicon atoms.

Water affinity is measured quantitatively in this work by contact angle measurements and analysis, and by deriving from this analysis the SFE. The

control of the water affinity is derived via our understanding of intermolecular interactions between the Si-based surfaces and water molecules.

2.6 The Role of Surface Topography in the Water Condensation of a Surface

Condensation vs. evaporation can be viewed as thermal dynamic balancing of pressures between saturation vapor pressure p_e and ambient vapor pressure p. Thus, when $p = p_e$, condensation and evaporation reach equilibrium. When $p > p_e$, condensation occurs faster than evaporation, while evaporation dominates condensation when $p < p_e$. Therefore, the ratio of $\frac{p}{p_e}$ determines whether the system at the liquid-solid surface interface is under net evaporation or net condensation. The Kelvin equation (Equation (2) below) shows that the curvature of the water droplet (i.e. $\frac{1}{r}$, where r is the radius of the water droplet) affects $\frac{p}{p_e}$, and therefore impacts the condensation behavior,

$$\ln\left(\frac{p}{p_e}\right) = -\frac{2\gamma V_M}{rRT} \qquad (2)$$

where

p is the actual vapor pressure,

p_e is the equilibrium vapor pressure,

γ is the SFE of liquid,

V_M is the molar volume of liquid,

r is the radius of the droplet,

R is the gas constant, and

T is the temperature [67, 68].

On a solid surface, the topography affects the water condensation and evaporation behavior through modifying the water droplet curvature in contact with the surface. With the surface being rough due to capillary-like features and the water droplet curvature $\frac{1}{r}$ becoming small (implying large r), water nucleation and condensation become easier as shown in Figure 14(a). Conversely, water droplets are more difficult to nucleate and condense as the surface becomes smoother and the water droplet curvature becomes larger as shown in Figure 14 (b). Thus a change in surface topography results in changing the water condensation behavior on the surface. The capillary-like features may act as "nucleation sites". This effect is in addition to the aforementioned molecular interactions between the surface and the water droplets which affect the contact angle (and hence the curvature of the droplet) as shown in Figure 14(c).

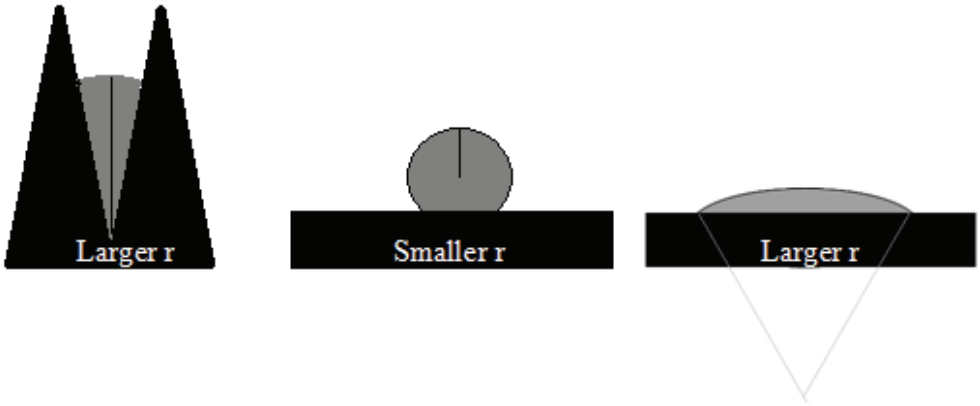

(a) (b) (c)

Figure 14.

Liquid droplet on (a) surface with capillary feature and (b) flat surface. Notice how the added nanofeatures of (a) effectively increase the radius of the water droplet when compared to (b). Thus, though the droplet volume is approximately the same for the droplet in (a) and (b), the radius of curvature is much less in (a) and thus the droplet in (a) will coalesce much easier (and at a more rapid rate) with other droplets than the droplet in (b). This topographical capillary effect is independent of the surface's water affinity, as (c) demonstrates a distinctive hydrophilic high SFE surface with a corresponding droplet of larger r.

CHAPTER 3

CONDENSATION EXPERIMENT, MATERIAL SELECTION, AND SAMPLE PREPARATION

3.1 Substrate Material Selection

Selection of sample materials used during this project was influenced by several factors. First, as noted in Chapter 1, the initiation of this research was inspired by the problem of fogging experienced by the retinal surgeons who first presented this complication to us. As the IOLs are composed of PDMS silicone, and exhibit a consistent, optical quality surface finish, it was only natural to use these PDMS silicone IOLs as one of the primary types of samples on which we used to determine the relation between fogging and water affinity or SFE. Thus, a steady supply of PDMS silicone IOLs was donated and used as the basis of the experiments in changing the water affinity and thus surface properties of these IOLs to prevent fogging. Note that acrylic IOLs were also included along side the PDMS silicone IOLs to make comparisons between simply the property of water affinity.

Second, again as noted in Chapter 1, the Si(100)-SiO_2 interphase formed during the bonding process of a silicon wafer to a silica wafer with an SiO_x nanophase was initially used as a launching point to explore how the surface properties could be modified by certain procedures (such as selected aspects of the Herbots-Atluri clean as shown in Figure 5). Thus, a second set of experiments was designed around understanding the effects of the water affinity or SFE of Si(100) surfaces and silica surfaces.

Third, as a natural extension to visionwear substrates in general, glass coated polycarbonate became of interest, as the issue of fogging during condensation is ubiquitous, adversely affecting high end visionwear in general (e. g. eye glasses, hockey and football helmet protective shields, etc). Glass coated polycarbonate is commonly used in the visionwear's industry; in particular for the manufacturing of high strength, impact resistant safety wear. Hence, glass coated polycarbonate substrates were used in order to determine their surface properties and therefore their water affinity, and how to prevent fogging during condensation. This approach also allows us to separate the physical property from the material by using the surface modification technique developed on PDMS silicone.

Finally, the last substrate, fused quartz silica wafer in the form of SiO_2 silica wafers was selected with several purposeful reasons in mind: 1) silica contains silicon and has a well defined compound stoichiometry of SiO_2; 2) silica and glass are closely related, where glass is often used as coatings on various visionwear products; 3) silica is not prone to damage during procedures such as IBA; and 4) quartz silica was reported in various scientific literatures of its contact angle analysis and SFE, and therefore direct comparison is possible for our experimental verification of our procedures.

3.2 Hydrophilic Molecular Films

3.2.1 Hydrophobic Surface Modification via Polymer Adsorption

A key idea led by our initial approach (as outlined in Chapter 1) is to modify the condensation behavior so it leads to wetting, instead of fogging.

It was quickly determined that an additional, biocompatible and benign substance would be needed in an effort to modify the surface of the IOLs in order to prevent fogging. Primary characteristics of the needed substance would be optical clarity, the ability to change the surface of the IOL from hydrophobic to hydrophilic, and most important, benign and non-toxic and well tolerated by the human body. Thus, several polymers were selected to determine their viability to fit the following criteria: 1) linear in the form of a hydrated gel 2) biocompatibility 3) non-toxic and benign effect on the human body 4) optical transparency, with minimal distortion 5) can be used to create a molecular hydrated film that adheres and transforms a hydrophobic surface to a hydrophilic surface, and 6) was readily available for experimentation. A final attribute was how the polymers' viscosity would play a role in modifying the targeted surface (linked to minimal distortion). There were several polymers attempted in hydrated gels approved by the federal food and drug administration. Figure 15 shows the range of linear polymer consistency which exists, from almost liquid, watery, to highly viscous polymers that are used to lend support in the human eye which are highly viscous such as molasses or honey [69].

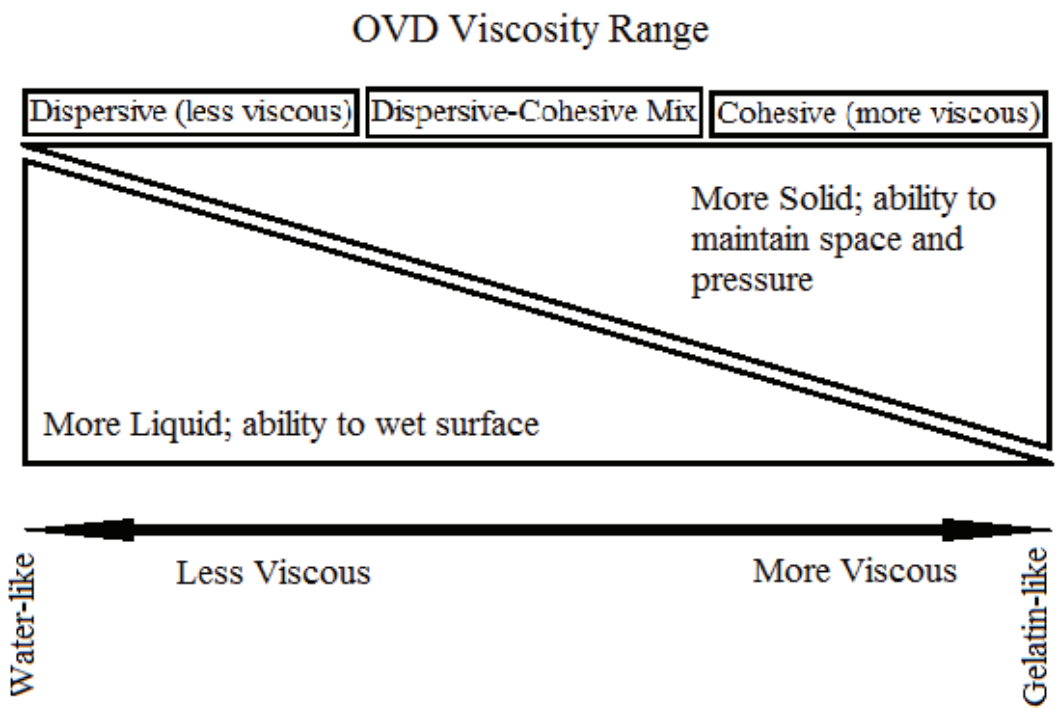

Figure 15.

A graphical representation of the range of viscosity possessed by a specific class of ophthalmic viscoelastic devices (OVDs). The viscosity range is from dispersive to cohesive, with a combination (of dispersive and cohesive) in the center.

3.2.2 Polymer Selection

Since the problem of fogging during condensation is well defined, and the scope of the environmental system constraints is also rigorous and well defined, the solution must match the stringent requirements of safely working within and on the human eye during retinal surgery. Hence, selection of the polymer is the first critical step in our analysis and determination of the solution. The polymer selected must be able to form a hydrated gel, since the polymer is to be in direct contact with the eye, and maintaining the proper hydration of the eye is critical throughout the retinal surgery to ensure success. Furthermore, the selected

polymer must create a thin, smooth molecular (polymer) layer which transforms the PDMS silicone (or silicon, polycarbonate) hydrophobic surface into a hydrophilic surface capable of inducing condensation with a uniform wetting layer instead of fogging. Figure 16 shows the characteristics of hydrophobic polymer, PDMS silicone. Figure 16(a) shows the monomer component; Figure 16(b) shows the PDMS silicone in its chain-like structure.

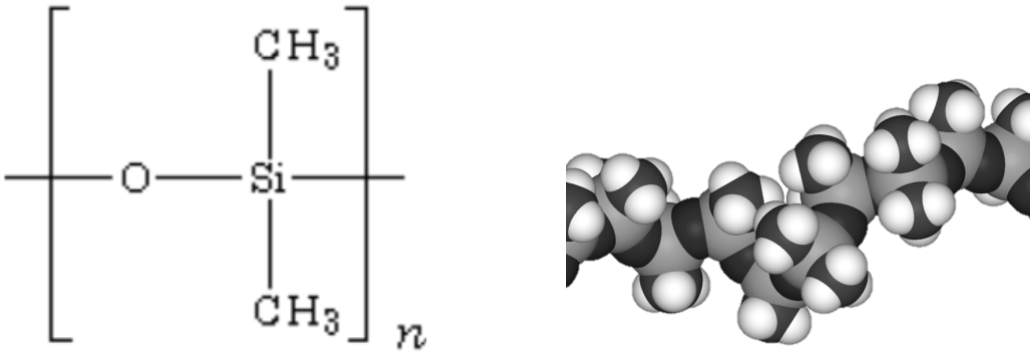

(a) (b)

Figure 16.

Multiple representations of PDMS silicone. (a) represents the PDMS silicone monomer, while (b) represents a PDMS silicone chain. The figure used with permission in accordance to the GNU Free Document License, V1.2 [8].

For the polymer to be hydratable, it must first be hydrophilic in nature. This allows water to interact with the polymer by having the polymer's radicals bond with the water molecules. Figure 17 shows the successive stages of hydration, ranging from under hydration, depicted in Figure 17(a), to full hydration, when all of the polymer's radicals have successfully bonded with the

water molecules, as shown in Figure 17(b), to over hydration, where there is an excess of water molecules compared to the available radicals to bond with, as shown in Figure 17(c) [70].

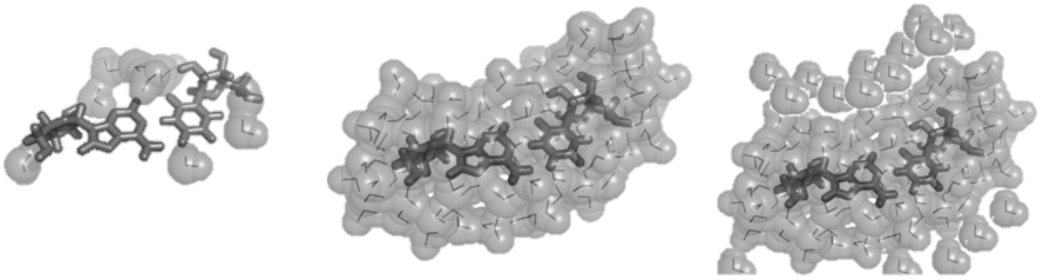

(a) (b) (c)

Figure 17.

The hydration process for a hydrophilic polymer is shown in the following sequence, (a) water molecules begin to bond with the radicals of the polymer, but have not bonded with all of the polymer's radicals, hence the polymer is under hydrated, (b) just enough water molecules have bonded with all of the polymer's radicals, and thus has fully hydrated the polymer, and (c) now there exists an overabundance of water compared to the number of radical sites on the polymer, and hence the polymer is now over hydrated. With over hydration one has free water flow. Figure used with permission in accordance of the Rights and Permissions section of the Copyright and License to Publish policy of the Proceedings of the National Academy of Sciences of the United States of America [70, 71].

Finally, the hydrated polymers selected form an emulsion. This emulsion allows the intermolecular force between the hydrated polymer and the PDMS silicone surface to create a solvated polymer film.

As a result of the intermolecular forces bonding the polymer film to the PDMS silicone surface, this polymer film now effectively creates a wetting layer. Thus, the hydrated polymer replaces fogging with a hydrophilic mesh. Figure 18 graphically demonstrates how this fully hydrated polymer mesh changes the surface from a hydrophobic surface which induces fogging during condensation, to a hydrophilic surface which induces condensation with a uniform wetting layer. This fully hydrated polymer mesh is very thin, below the thickness which interferes with light transmission, and therefore does not distort or change the optical properties of the original PDMS silicone surface.

Two polymers were selected, occupying opposite ends of the viscoelastic spectrum. The first is hyaluronic acid, with its monomer $C_{33}H_{54}N_2O_{23}$, 846.8 grams/mole. Being the most viscous, hyaluronic acid combined with a balanced electrolyte solution is the exact composition as that of the vitreous humor in the human eye, and can be simply extracted as a protein from sterile chicken stock, and is of animal origin. The other polymer is HPMC, with its monomer $C_{32}H_{60}O_{19}$, 748.8 g/mole. HPMC is much less viscous than hyaluronic acid, and is of vegetable origin. Hyaluronic acid has side branches of higher molecular weight, with a very high number of oxygen atoms in termination positions, which is highly electronegative and thus creates more viscous properties in the polymer chain. Cellulose, on the other hand, has fewer oxygen atom termination positions and is the least viscous.

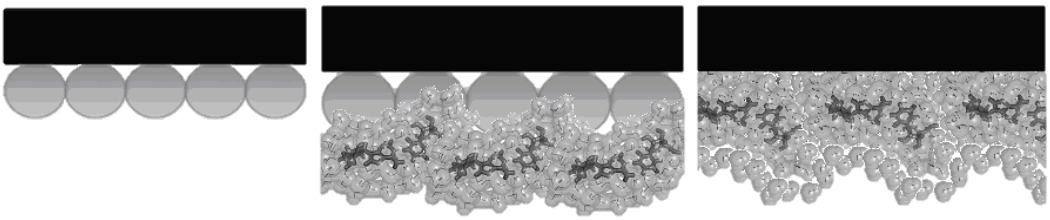

(a) (b) (c)

Figure 18.

Fully hydrated polymer mesh via uniform wetting replaces fogging. In (a), the PDMS silicone surface (black) is hydrophobic in nature, as depicted by the water beads. In (b) the fully hydrated polymer mesh is applied, using the intermolecular forces to bind the polymer film to the PDMS silicone surface. In (c) the fully hydrated polymer mesh changes the water affinity and PDMS silicone surface from hydrophobic to hydrophilic in nature, and enables an even, uniform wetting layer to form, resulting in the elimination of fogging while maintaining optical clarity.

3.3 Condensation Experimental Design and Surface Modification Model

3.3.1 Testing of Condensation Model with Acrylic and PDMS silicone IOLs

Direct observation provides a key understanding of the unique two step water interaction with PDMS silicone surfaces and why it enhances fogging during condensation. In preliminary experiments, the behavior of hydrophobic PDMS silicone IOLs and Si(100) was observed to be very different from hydrophilic acrylic lenses, hydrophilic Si and other hydrophilic materials because PDMS silicone is in fact a composite material made from two kinds of molecules, (1) insulating silicon dioxide and (2) organic chain polymers.

During the Herbots-Atluri clean, it is observed that when in contact with an aqueous solution, a stable, smooth, defect-free stoichiometric silicon dioxide with saturated bonds is strongly polar, and exhibits a response that can be described as strongly hydrophobic, unless hydrocarbons, or defects are also present which exhibit a reverse, hydrophilic behavior.

3.3.2 Contact Angle Visualization to Monitor Condensation during Tests and Compare between Lens Materials and Surface Modifications

The first tests measure how strong the initial hydrophobic behavior is, and detects easily modifications. In Figure 19(a), contact angle measurements compare hydrophobic PDMS silicone and in Figure 19(b) hydrophilic acrylic wetting response. We used as the definition of a hydrophobic surface as a drop of water having a contact angle > 90° as shown in Figure 19(c), while a hydrophilic surface is that drop of water possessing a contact angle < 90° as shown in Figure 19(d).

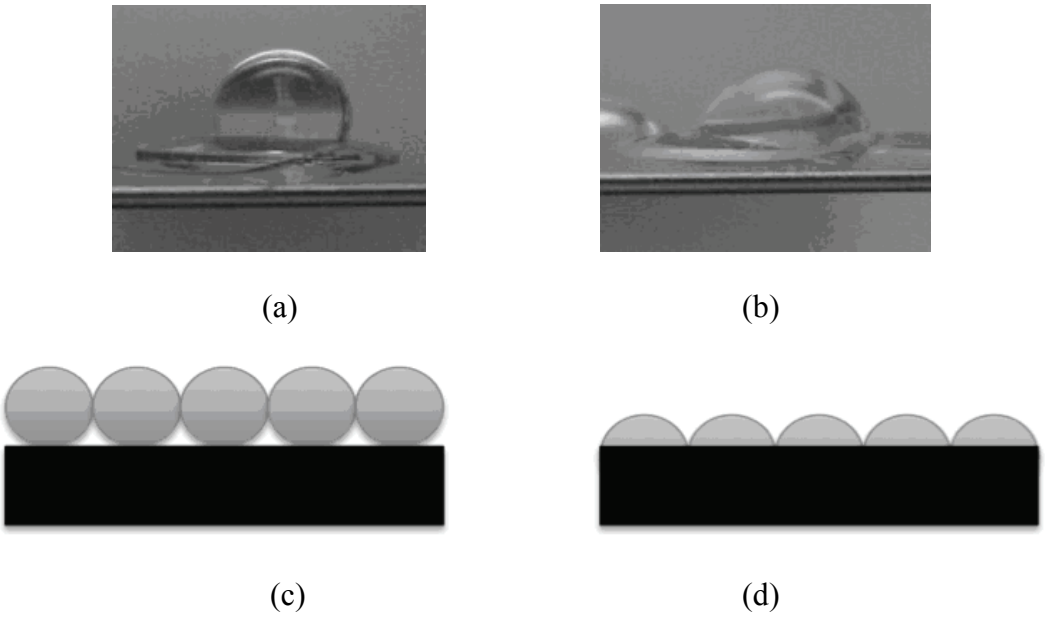

Figure 19.

The hydrophobic PDMS silicone (a), exhibits angles well above 90° (120°). The hydrophilic acrylic (b), which does not have such a severe condensation problem, consistently exhibits contact angles always below 90° (80°). When condensing drops come into contact, droplets on the PDMS silicone trap air between their boundaries, while the flatter droplets on acrylic contact each other at their base. These are thus more likely to form a continuous, uniform film through which visibility is maintained, (c) On PDMS silicone, condensed spherical droplets, (d) on acrylic, large contact angle droplets appear opaque due refraction between trapped forms a transparent, refractivity homogeneous water air and water droplets with high contact angle.

3.3.3 Condensation Experiment

After confirming the fogging event in the lab, the experimental map was laid out systematically. The ultimate goal was to create a hydrated network of hydrophilic polymer chains of which to bond to the PDMS silicone (or other) substrate without optical distortion. We required a hydrophilic molecular film. It is important to keep the boundary conditions clearly in mind, and are repeated here for convenience: 1) linear polymer in the form of a hydrated gel 2) biocompatibility 3) non-toxic and benign effect on the human body 4) optical transparency, with minimal distortion 5) can be used to create a molecular hydrated film that adheres and transforms a hydrophobic surface to a hydrophilic surface, and 6) is readily available for experimentation. The ultimate determination of success is to significantly delay or prevent the onset of fogging during condensation with minimum optical distortion using a hydrated polymeric mesh that is biocompatible with the human eye.

From the polymer analysis above, based on the requirements of a biocompatible, benign polymer, two polymers were selected: hyaluronic acid and HPMC. Hyaluronic acid hydrates into a high viscosity based gel, while HPMC hydrates into a low viscosity gel. The HPMC was further split into 4 different molecular weights (i.e. different polymer lengths): 10 kDa, 86 kDa, 90 kDa, and 120 kDa.

As shown in Figure 20, a water vapor chamber, which is a plastic artificial eye, with respiration holes allows the water vapor to enter and leave the chamber to maintain consistent pressure and temperature. The heating plate and

thermometer control the water temperature in the Petri dish. The surface under study is placed on top of the water vapor chamber. An overhead camera with optional microscope monitors and captures the condensation images. Time to fog data is collected by placing the surface of interest on top of the water vapor chamber. Placement is done at time t = 0. Then, using a stopwatch (started at t = 0 when the surface of interest, e.g. IOL, is placed atop the water vapor chamber), time is measured and then stopped either when fogging becomes visible on the IOL, or until 1200 seconds (20 minutes) has passed. Preliminary experiments demonstrated that if no fogging occurred after 20 minutes, fogging generally didn't occur for as long as time was measured (the longest being greater than 2 hours). The same general experimental apparatus was used to measure fogging times for other surfaces. Instead of using the water vapor chamber (plastic artificial eye), a water beaker was used with a place to mount the samples over the water vapor.

Qualitative analyses of condensation patterns as well as the time stamps of these images are analyzed to characterize the time versus condensation pattern. Different HPMC concentrations were systematically mixed, applied to the IOLs and then the time to fog was measured. Note that it was quickly observed that if no fogging occurred within 15 minutes to 20 minutes, then fogging did not occur subsequently; for the IOLs time to fogging was tested a maximum of 2 hours for IOLs that exhibited no fogging. Henceforth, the time of measurement was limited to 1200 seconds (20 minutes). While the hyaluronic acid at 1% wt. prevented fogging, it was so viscous that it introduced severe optical distortion on the IOL.

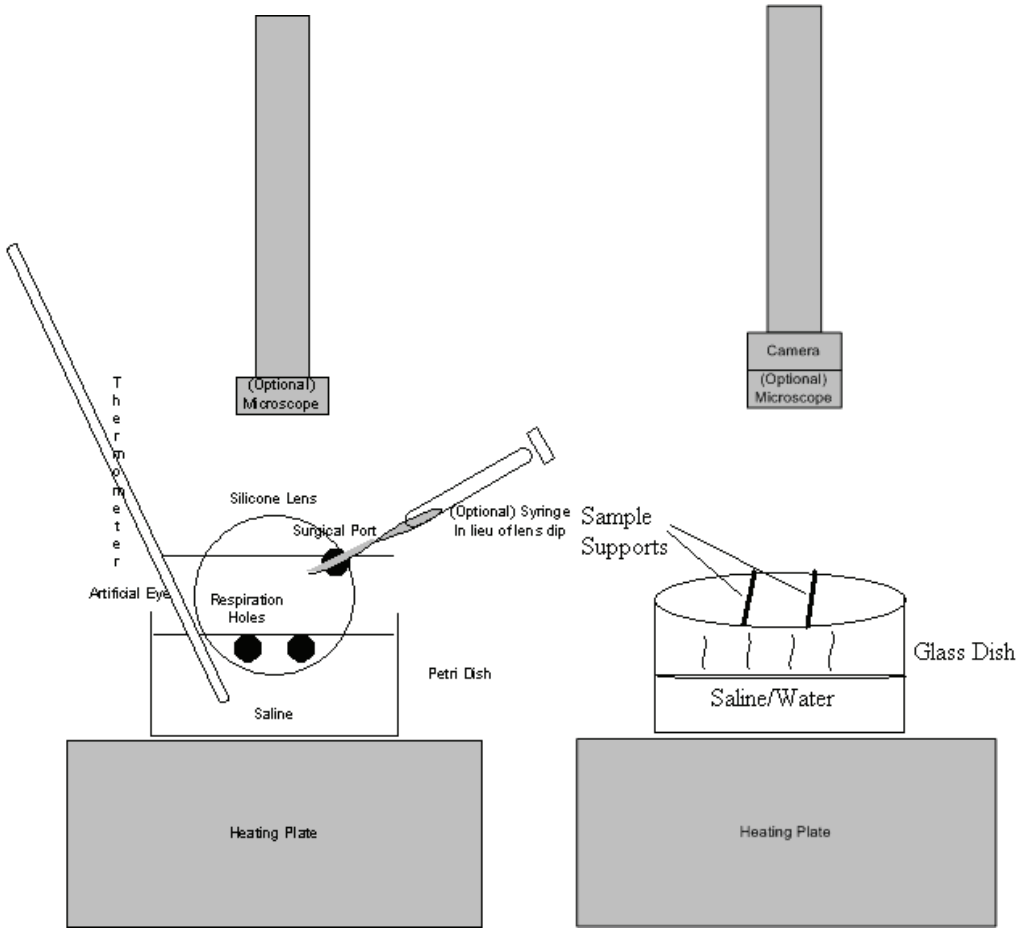

(a) (b)

Figure 20.

Experimental setup (a) for testing the IOLs for fogging during condensation. A plastic artificial eye had two large holes of at least 0.5 cm in diameter cut in the bottom to allow the heated saline to enter the artificial eye. A small hole was cut to act as the surgical port in which a syringe or other device could be maneuvered into the artificial eye. A final hole was cut into the top of the artificial eye of the size about 7 mm diameter; this is where the artificial lens (IOL) was placed to test for fogging. (b) A similar setup is used to test condensation on non-IOL samples.

A working range of emulsion and dried adsorbates prepared from the emulsion is summarized in Table 1. Note that, the working range is a rough estimate, since the testing step is 2 times or 0.5 times in most cases. For an example, if the upper limit of working range is 1% wt., it implies that 2% wt. failed the visual clarity test; if the lower limit of working range is 0.2% wt., it implies that 0.1% wt. failed the visual clarity test.

Table 1.

Vision clarity working range vs. polymer adsorbates. Substrate types included silica wafer and PDMS silicone; polymer types included HPMC cellulose and hyaluronic acid(NaHa); vision clarity working ranges included lower limit and upper limit of polymer adsorbates concentration % wt. in water with two applying methods, one is applying the emulsion directly, the other is dried adsorbates prepared with the emulsion. "-" means not tested, "×" means tested but did not work.

Substrate Type	Polymer Type	Dried Adsorbate Prepared with Emulsion Lower Limit (% wt.)	Dried Adsorbate Prepared with Emulsion Upper Limit (% wt.)	Emulsion Concentration Lower Limit (% wt.)	Emulsion Concentration Upper Limit (% wt.)
Silica Wafer	86 kDa HPMC	0.2%	1%	0.005%	1%
PDMS Silicone	86 kDa HPMC	0.2%	1%	0.005%	1%
PDMS Silicone	120 kDa HPMC	-	-	×	×
PDMS Silicone	10 kDa HPMC	-	-	1%	5%
PDMS Silicone	4 MDa NaHa	-	-	×	×

3.4 Materials and Supplies List

Numerous materials were required for this research project. Deionized (DI) water used was 2 MΩ cm resistivity unless otherwise noted. Fused silica wafers are from Medtronic, and were sonicated 10 minutes in DI water of 18 MΩ cm resistivity. The PDMS silicone lenses used were Bausch & Lomb HD-500 IOL. The polymer used was HPMC, $C_{32}H_{60}O_{19}$, CAS-9004-25-3, was 86 kDa molecular weight from Sigma-Aldrich and is hydrated using DI water. Glycerin was obtained from Sigma-Aldrich (G2289, CAS number 56-81-5), as was α-bromonaphthalene (17640, CAS number 90-11-9). The visors are Oakley brand and were selected randomly.

The silica wafers, the PDMS silicone lenses, and the Oakley visors were coated with the HPMC cellulose film at room temperature by soaking them in water hydrated HPMC for 2 hours at various concentrations (from 0.20% wt. to 1.00% w.t), and then air dried under a class 10K ventilation hood for a minimum of 24 hours.

The passivation samples consisted of 100 mm Boron (B) doped ultra flat Si(100) silicon wafers with a resistivity of 10 Ω cm to 14 Ω cm donated from Motorola. For annealed samples and as-received samples, the silicon wafers were 100 mm B-doped Si(100) with a resistivity of 10 Ω cm to 20 Ω cm and manufacture by Wacker Siltronic Corp. Chemicals used were the following: from KMG Electronic Chemicals, Inc; hydrochloric acid HCL (CAS number 7647-01-0), hydrogen peroxide H_2O_2 30% (CAS number 7722-84-1), Amonium Hydroxide 29% (CAS number 1336-21-6), and hydrofluoric acid HF 49% (CAS number

7664-39-3); and from JT Baker, Inc; methanol (CAS number 67-56-1). All chemicals were of electronic grade or better.

For wet chemical cleaning process and anneal, three sets of samples were prepared: the As-Received set, used as the Control Sample set, the Passivation-Sample set, and the Anneal-Sample set. The As-Received samples received no processing once removed from the wafer boat. The patented Herbots-Atluri wet chemical clean and passivation were performed in a class 10 chemical hood in a class 100 cleanroom, on both the Passivation-Sample and the Anneal-Sample; whose procedure is detailed elsewhere [27]. The Passivation-Sample received no further processing. The Anneal-Sample underwent a 24 hour 200 °C anneal at standard atmosphere and pressure immediately after receiving the Herbots-Atluri clean. The temperature was slowly ramped linearly from room temperature to 200 °C over a 30 minute time period. Cool down involved shutting the oven off and required 4 hours to cool to room temperature.

CHAPTER 4

RUTHERFORD BACKSCATTERING SPECTROMETRY, NUCLEAR RESONANCE SCATTERING, AND ELASTIC RECOIL DETECTION

4.1 Purpose

4.1.1 Determining the Areal Density of HPMC Cellulose

RBS was used to analyze polymer and substrate profiles including diffusion profiles, the aging process of organic photovoltaic cells, and polymers used for medical purposes [72-74]. Recently RBS was used to help characterize Poly(2-(methacryloyloyloxy)ethyl phosphorylcholine) brush-like structures [75].

Since the present research investigates how to render a surface hydrophilic by creating a hydrophilic aqueous emulsion using pure water such as DI water and hydrated linear polymers chains in the form of gels or dehydrated gels, a method had to be devised to characterize the composition of the surfaces modified in their water affinity via the application of a polymeric emulsion. First, as described in Chapter 3, a physical model to create and test such an emulsion had to be devised.

As discussed in Chapter 1 to 3, our initial model features for an emulsion that is to be applied to the surface in order to eliminate fogging, which also renders the surface hydrophilic by nucleating a uniform continuous wetting layer during condensation. The further development of this initial, simple model of complete wetting during condensation was the conception of a physical emulsion to apply on the surface, either by immersion or direct application. The goal is to create a hydrophilic film in the form of a fully hydrated polymeric mesh to

modify the water affinity of Si-based surfaces and polymer based surfaces. These surfaces include optical quality hydrophobic PDMS silicone, glass coating on polycarbonate visors, quartz silica wafer and other substrates used either in vision wear or fundamental surface studies. The surfaces investigated by IBA will thus include comparison surfaces to characterize and quantify topography, water affinity and SFE in a quantitative manner as described in the later two Chapter 6 and 7, which discuss topography and SFE as a function of water affinity of Si-based surfaces.

To test the model and the formation of a hydrophilic, fully hydrated microscopic mesh to inhibit droplet nucleation and favor the formation of a continuous wetting layer on hydrophobic surfaces, the experimental method developed in Chapter 3 based on the constraints from the key application discussed in Chapter 1 and the physical concepts of water affinity discussed in Chapter 2 involve in the present chapter creating in a water solution a hydrophilic mesh consisting of

(a) bio-compatible linear polymer chains,

(b) fully hydrated and long enough to tangle into a mesh of hydrated polymer strands,

(c) trapping, in addition to the water in the gel, free flowing water molecules on the surface and the mesh to render it hydrophilic by creating an initial, continuously wet layer while remaining thin enough to maintain full optical transparency and avoid any optical distortion.

This latter property of the emulsion is necessary in most vision applications, whether it is to enable visualization of the retina by the surgeon during microsurgery for retinal repair, or for simpler applications in vision wear.

This physical model of a polymeric molecular adsorbate with a specific microstructure developed to modify water affinity will be referred to as of a hydrophilic, fully hydrated polymer mesh.

4.1.2 Correlation of Cellulose Content with Initial Concentration of Emulsion

As discussed and shown in Chapter 3, the concept of a hydrophilic, fully hydrated microscopic mesh applied on a surface by using tangled hydrated polymer strands in an aqueous emulsion leads to an experimental method where the adsorbate mesh from a well calibrated emulsion is systematically investigated by exposing to condensation the adsorbate applied from the emulsion as a function of the degree of hydration of the gel (by % wt. in water) the polymer chain length, and emulsion dilutions, until an optimum hydrophilic, fully hydrated polymeric mesh is created and maintains wetting without fogging during condensation for extended durations. Extended duration means approximately 20 minutes, as the minimum required for retinal surgery, and longer. Such durations are thus at least three orders of magnitudes larger than the few seconds within which fogging typically occurs and subsequently remains.

Thus, in the present chapter, a key feature of the hydrophilic hydrated mesh model is to further establish, in the investigation of a wide range of hydration, the amount of cellulose found resulting from varying polymer content in the water gel by weight, between 0.1% wt. to 2% wt. in water. Also, a

characterization method of the adsorbate film after application and condensation is developed, and combines several forms of IBA to yield the desired measurement and correlation.

Since the adsorbate is a hydrated polymer mesh, the IBA method has to measure

(a) the HPMC cellulose polymer content (or areal density) adsorbed on the modified surface to accurately measure the compositional range investigated for the emulsion and gel

(b) the stoichiometry of the polymeric adsorbates to compare with and provide an independent calibration of the areal densities obtained.

A key feature to be investigated in the model for the microscopic hydrated polymeric mesh is that condensation adds water to it. But nevertheless, the added water molecules do not dramatically affect water affinity. Increasing water dilution over a significant range is a quantitative approach to measure that mechanism. The fact that the modified surfaces remain hydrophilic for several hours under condensation in an artificial eye as well as during test surgery constitute two independent confirmations of this property, which is the maintenance of hydrophilic behavior as water is condensing on the modified surface.

After experimenting with various viscoelastic gels, the simplest and most successful emulsion to modify water affinity was found to be, as described in Chapter 3, a HMPC cellulose gel. Additionally, after experimenting with various polymers, various polymer chain lengths, various gel concentrations, increasing

emulsions dilutions, and establishing that the physical model of a hydrophilic hydrated mesh, the experimental method converged on cellulose in the form of HPMC cellulose $C_{32}H_{60}O_{19}$ polymer chains in the range of 80 kDa - 120 kDa, emulsified in deionized water in rations between 0.2% wt. to 1% wt..

In the present chapter, IBA is thus used to correlate the composition and amount of HPMC cellulose based emulsion to the final composition of the Si-based surfaces after modification through application of HPMC cellulose of their water affinity. The method developed addresses the obvious difficulty of measuring the thickness of aqueous films, given their rate of evaporation and plasticity. The use of IBA requires high vacuum and thus water cannot be present on the surfaces to be analyzed. The first step is thus to dehydrate in a hood the modified surfaces of IOLs and other Si-based substrates used for measuring the areal density of thin polymeric contents.

The thickness of polymeric films is quite difficult to measure given the majority of the elements they are constituted of is carbon, hydrogen, and oxygen which are very light atoms compared to the substrate element silicon. As the scattering cross section is proportional to the square of the atomic number, and sensitivity is proportional to the scattering cross section, the sensitivity is thus limited for light elements with a heavy element background, “heavy” being defined as silicon. Since we use a He^{++} incident beam, H atoms are lighter than He^{++}, thus He^{++} cannot be detected by back scattering. In the case of HPMC cellulose ($C_{32}H_{60}O_{19}$), hydrogen constitutes more than 50% of the atomic content of one of these light organic molecules. Henceforth the present research had to

devise a method to characterize the polymers remaining on the surface after successfully modifying its water affinity via the application of the hydrophilic, fully hydrated polymeric mesh in the form of an aqueous emulsion.

The method of letting the emulsion dry and then characterize the cellulose residue eliminates uncertainty in dilution during water condensation experiments and ascertains the net amount of polymer material that needs to be present to control condensation without fogging by rendering the surface hydrophilic.

The following approach was developed using IBA to measure the amount of cellulose necessary to modify water affinity. An attractive property of IBA is atom counting. Since the polymer chains used in the inhibition of fogging are precisely diluted and emulsified in an aqueous solution, atom counting is a direct approach to measure the amount of cellulose in the form HMPC, its thickness and stoichiometry. It can then be translated into a precise amount of emulsion, by converting the contribution of the weight of the polymer into the gel into total gel weight, and then into the amount of emulsion via the dilution.

In this work, we investigated first if we could establish the net thickness of the HPMC cellulose strands film via the energy loss of 2 MeV He^{++} through the polymer adsorbates, as measured by the energy loss in the backscattering energy from the silicon atoms underneath the adsorbate layer of HPMC cellulose remaining after dehydrating the hydrophilic surface. Next, we compared the results obtained from this energy loss method by investigating the stoichiometry of the HPMC cellulose film via nuclear resonance scattering. The present work measured the areal density of the carbon atoms in the HMPC cellulose using the

4.265 MeV $^{12}C(\alpha, \alpha)^{12}C$ to enhance the carbon cross section and the 3.045 MeV $^{16}O(\alpha, \alpha)^{16}O$ to enhance the oxygen cross section, thus improves the spectra C and O signal sensitivity.

4.2 Background of RBS, Nuclear Resonance Scattering, and ERD

4.2.1 Description of RBS

RBS is one of the IBA methods, carried out by steering a mono-energetic, collimated beam of ions, (H^+, He^+, or He^{++} are the typical species used) at the target being characterized. The kinetics of the system is well known and has been explicitly described elsewhere [21, 22]. Essentially, the beam of ions collides with the atoms of the sample and scatters in multiple directions as a result. A detector collects and measures the kinetic energy of the ions scattered in the direction of the detector.

A key parameter is the kinematic factor,

$$k = \frac{E}{E_o} = \left[\frac{\left(m_2^2 - m_1^2 \sin^2 \theta_L \right)^{\frac{1}{2}} + m_1 \cos \theta_L}{m_1 + m_2} \right]^2 \qquad (3)$$

with

E is the detected energy after Rutherford backscattering,

E_0 is the ion incident energy,

θ_L is the scattering angle in the lab reference frame,

$m_{1,2}$ is the mass for the two scattering atoms respectively.

k is important because the target's mass can be determined by knowing only the incident ion's mass, initial energy, detected energy, and scattering angle [76].

4.2.2 Areal Density and Scattering Cross Section

Scattering cross section is the probability of occurrence of Rutherford backscattering [76], in the lab reference frame,

$$\frac{d\sigma}{d\Omega}=\left(\frac{Z_1Z_2}{4E}\right)^2\left(\frac{1}{\sin^4\left(\theta_L/2\right)}\right)\frac{\left\{\left[1-\left(\frac{m_1}{m_2}\sin\theta_L\right)^2\right]+\cos\theta_L\right\}^2}{\left[1-\left(\frac{m_1}{m_2}\sin\theta_L\right)^2\right]^{1/2}} \qquad (4)$$

with

σ is the Rutherford scattering cross section,

Ω is the detector solid angle,

θ_L is the scattering angle in the lab reference frame,

$Z_{1,2}$ is the atomic number for the two scattering atoms respectively,

$m_{1,2}$ is the mass for the two scattering atoms respectively,

E is the kinetic energy of the 1st atom (where 2nd atom has 0 kinetic energy).

Atomic density N atom/cm^3 and of thickness t cm, the sample presents an areal density is Nt atom/cm^2 for an ion beam impinging normal to the sample. Furthermore, knowing the number of ions Q impinging on the target, the number of particles striking the detector is $n=Q\sigma\left(\theta_L\right)Nt\Omega$. The detector discriminates energies of the detected ions, and bins them in the histogram form, with each bin representing a channel or discrete energy range (the bin width) and the number of

counts at the respective energy (the bin height) referred to as "yield" from this point on.

Considering two elements A and B in the same spectrum,

$$\frac{N_A t}{N_B t} = \frac{n_A \sigma_B}{n_B \sigma_A} \tag{5}$$

where subscripts A and B represent the two elements respectively [76].

4.2.3 Energy Loss and Straggling

A significant percentage of the impinging ions which are scattered and detected penetrate below the surface of the target before undergoing a scattering event. These penetrating ions lose energy as they travel deeper into the target and as they travel back towards the surface after a scattering event. Energy loss during transit occurs as the ion passes near enough to the target atom that discrete amounts of energy are transferred to the target electrons. The entire trip into and out of the target involves many such interactions as to approximate the energy loss in a continuous fashion. This rate of energy loss is called the stopping cross section $\varepsilon_E = \frac{1}{N}\frac{dE}{dx}$ with N is the density of the target material and $\frac{dE}{dx}$ is the change of energy per change of thickness into the sample, and also known as the stopping power. Both stopping cross section and stopping power have dependency of the ion type as well as ion energy, ε_E is used to note the stopping cross section ε at E.

Energy loss of ions can be used to determine the film thickness [77]. The energy loss due to the in-path of incident ion and the out-path of the scattered ion

needs to be considered. If an element exists in the substrate only and not in the film, one can determine the energy loss due to the energy loss in the film,

$$\Delta E = kE_0 - E \tag{6}$$

with

ΔE is the energy loss,

k is the kinematic factor,

E_0 is the incident ion energy, and

E is the ion energy at the detector.

There are two contributions to the ΔE, one contribution is due to the in-path where the incident ions lose energy in the film before reaching the substrate, $\Delta E_{in-path} = N\int_0^{t_{in-path}} \varepsilon dx \approx Nt_{in-path}\varepsilon_{E_0}$ where $t_{in-path}$ represents the ion travel distance of the in-path; when the ion reaches the substrate, its energy thus becomes $E_s = E_0 - \Delta E_{in-path}$, after the ion being scattered, thus becomes kE_s The other contribution is due to the out-path where the backscatter ion from the substrate lose energy before getting out of the film. Similarly $\Delta E_{out-path} \approx Nt_{out-path}\varepsilon(kE_s)$ where $t_{out-path}$ represents the ion travel distance of the out-path. When total energy loss ΔE is much smaller than kE_0, we can determine the areal density of the film,

$$\Delta E \approx kNt_{in-path}\varepsilon_{E_0} + Nt_{out-path}\varepsilon_{kE_0} \tag{7}$$

Bragg's rule provides a way to compute the stopping cross section of a compound,

$$\varepsilon_{E,A_mB_n} \approx \frac{m\varepsilon_{E,A} + n\varepsilon_{E,B}}{m+n} \quad (8)$$

with

$\varepsilon_{E,A}$ is the stopping cross section for element A at energy E, similarly, when A is replaced by B or A_mB_n, it means for the said element or compound respectively.

As a result of the energy loss, the RBS spectra have a depth resolution of

$$\delta E = \sqrt{\delta E_s^{\,2} + \delta E_d^{\,2}} \quad (9)$$

with

δE_s is the energy straggling resolution due to the energy stopping power, δE_d is the detector resolution [76].

4.2.4 RBS with Nuclear Resonance Scattering

Since all of this work's IBA involves silicon as being either the substrate, or a main component of the substrate, the oxygen signal to noise ratio and carbon signal to noise ratio decreases significantly by being on top of the Si signal background with RBS. The silicon bulk signal acts as background noise when trying to resolve the oxygen signal and carbon signal [24]. Thus, NRA is used to enhance the oxygen and carbon signals. The ^{12}C cross section at the 4.265 ± 0.055 MeV nuclear resonance with the following nuclear interaction: 4.265 MeV $^{12}C(\alpha, \alpha)^{12}C$ is enhanced 128 times compared to that of the Rutherford cross section for carbon. Similarly, the ^{16}O cross section at the 3.045 ± 0.005 MeV nuclear resonance with the following nuclear interaction: 3.045 MeV $^{16}O(\alpha, \alpha)^{16}O$ with He^{++} is enhanced 27 times compared to that of the Rutherford cross section for

oxygen for nuclear elastic scattering at this resonance energy [78, 79]. Thus, NRA allows for a tremendous amplification of the carbon signal and oxygen signal relative to the background signal (including the Si substrate signal).

4.2.5 RBS with Channeling

Finally, in specific cases where there is a crystalline structure that generates periodic order with respect to the sample lattice structure, such as single crystal Si(100), another IBA method can be used to augment the respective non-crystalline elements on the surface, such as oxygen, carbon, and unregistered Si surface signals relative to the background noise, that is channeling. Channeling reduces the background substrate signal of Si by a factor of 10 by aligning the incident ion beam with one of the crystalline axes [80]. The procedure to successfully channel on a crystalline Si substrate is detailed elsewhere [21, 22, 24]. When channeling data is collected, areal density calculations require that a rotating random spectrum be collected due to the need for the silicon surface signal height [24]. The rotating random spectrum was generated by first tilting the sample off axis of any principle or secondary crystalline axes. Then, to ensure a truly random spectrum without the influence of channeling, the sample was then rotated slowly via the goniometer on which the sample was mounted through a total arc of roughly 20 degrees.

Determining the areal densities of the elements of Si, O, C, and H are of central importance to the data results and analysis of this research. Si, O, and C areal densities are calculated by using the standard surface approximation with normalization implemented by using the Si substrate signal obtained from the

rotating random spectrum. The general equation to determine the areal density of carbon, oxygen, and Si surface peak is [76]

$$(Nt)_{C,O,Si} = \frac{A_{C,O,Si}\sigma_{Si}\delta E}{H_{Si}\sigma_{C,O,Si}\left[\varepsilon_{C,O,Si}\right]_{Si}\cos\theta_1} \quad (10)$$

with

$A_{C,O,Si}$ is the carbon resonance peak, oxygen resonance peak, and Si surface peak area integrations respectively, channeling preferred, but not mandatory,

$\sigma_{C,O,Si}$ is the scattering cross sections of carbon resonance, oxygen resonance, and Si surface peak respectively,

H_{Si} is the rotating random Si signal height,

$\left[\varepsilon_{C,O,Si}\right]_{Si}$ is the silicon stopping cross section at carbon resonance energy, oxygen resonance energy, and the energy when ion reaches the Si surface atoms, respectively

θ_1 is the incident angle to the sample normal,

δE is the energy width per channel.

Oxygen and Si surface peak areal density on Si(100) from films of 2 nm to 20 nm thickness can be measured using the IBA techniques of channeling, rotating random, and nuclear resonance scattering [27, 32, 81].

4.2.6 ERD

In order to use IBA to quantitatively analyze hydrogen, ERD was required due to the kinematic restrictions imposed on the system [82]. Since H is the

lightest of elements, and incident ion heavier that the hydrogen atom would not make back scattering possible. Instead, a detector is placed in a forward scattering location within the IBA chamber relative to the sample, and shielded with a mylar foil to prevent all but the H atoms from being detected, counted and binned per its scattered energy [76, 83]. Then, as the incident ion beam forward scatters the H atoms, the detector then bins the H energy. Note that the H must pass through the sample and the mylar before being counted, and thus the result of the H detection is a depth profile. The biggest constraint in using ERD is the requirement of measuring a sample with a known amount of hydrogen in order to calibrate the counts of subsequent samples [76, 84].

Thus, the sample with unknown H is evaluated by comparing its H coverage with the known sample, using the following to determine the H fraction of the sample [85]

$$x = \frac{R\left(\varepsilon_{matrix}\right)}{\varepsilon_{std} + \varepsilon_{H}\left(1-R\right)} \tag{11}$$

With

R is the ratio of H in the sample over the standard,

ε_{matrix} is the weighted sum of stopping powers of the sample matrix,

ε_{std} is the weighted sum of stopping powers of the standard matrix, and

ε_{H} is the stopping power of hydrogen.

ERD was used to successfully measure and study the induced H ejection in polymers, in effect looking at the damage of the polymers with respect to MeV incident He^{+} ions [86]. ERD has also been used by this group to examine

hydrogen passivation on Si(100) wafers [87]. ERD was also used in conjunction with a heavier ion beam, in which case elements heavier than H can be analyzed in a forward scattered configuration [88, 89].

4.3 Areal Density of HPMC Cellulose

4.3.1 Energy Loss Method in Determining the Areal Density of HPMC Cellulose

The presence of a heavier atom like Si in the substrate is critical to conduct an energy loss analysis to measure the areal density of a polymer film whose atoms are too light to be detected by conventional RBS directly such as carbon and oxygen. HPMC cellulose ($C_{32}H_{60}O_{19}$) film causes an energy loss of the Si signal from the Si-based substrate compare to when there is no film. With given geometry shown in Figure 21, we can determine areal density from Equation (6) and (7),

$$N_{C_{32}H_{60}O_{19}}t = \frac{\Delta E}{k_{Si}\frac{1}{\left|\cos\theta_1\right|}\varepsilon_{E_0,C_{32}H_{60}O_{19}} + \frac{1}{\left|\cos\theta_2\right|}\varepsilon_{kE_0,C_{32}H_{60}O_{19}}} \qquad (12)$$

with

$N_{C_{32}H_{60}O_{19}}t$ is the areal density of $C_{32}H_{60}O_{19}$,

θ_1 is the incident angle with respect to sample normal,

θ_2 is the detector angle with respect to sample normal,

k_{Si} is the kinematic factor of incident ion scattered by the Si atom,

$\varepsilon_{C_{32}H_{60}O_{19}} \approx \frac{32\varepsilon_C + 60\varepsilon_H + 19\varepsilon_O}{32+60+19}$ with ε_C, ε_H, and ε_O obtained from [77].

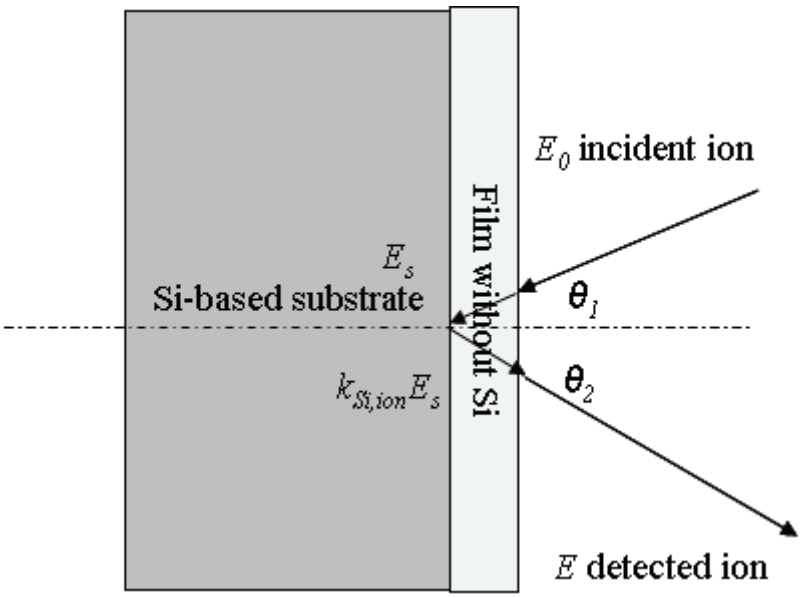

Figure 21.

Energy loss method is used to determine areal density of a film applied to a Si-based substrate. E_0 is the incident ion energy, E_s is the ion energy at the substrate before being scattered, $k_{Si,ion}$ is the kinematic factor of ion being scattered by the Si atom in the substrate, E is the ion energy at the detector, θ_1 is the incident angle with respect to sample normal, and θ_2 is the detector angle with respect to sample normal.

4.3.2 Experiment Design

The areal density was obtained to analyze the HPMC cellulose film using He^{++} RBS. The non-conducting substrate experienced sample charging due to the ion beam incidence which was observed for both the silica wafer and the PDMS silicone lens samples. The charging effect was minimized by grounding the sample using an aluminum foil wrapping with a 4 mm to 10 mm diameter hole cut to expose the sample directly to the ion beam. This enabled consistent,

reproducible data collection. The experiment was conducted in a vacuum of 10^{-7} Torr to 10^{-6} Torr using an ion pump and turbo pumps. Thus, carbon contamination during the data collecting process, a major concern that can confound the data, is minimized and does not become a concern [90].

An incident angle of 0° (normal to the surface) was used for films prepared with of 0.33% - 1.00% wt. HPMC in water, while a 65° incident angle was chosen for thinner films prepared with < 0.33% wt. HPMC in water. The incident angles were chosen so that the silicon edge of the RBS spectra would be exposed for thicker films, while also being able to enhance the energy loss resolution for the thinner films. The detector is set at a scattering angle of 170° and incident He^{++} energy is 2 MeV with the beam current approximately 20 nA. The ion beam cross section is approximately 1.5 mm × 1.5 mm. Detector resolution δE_d is approximately 20 keV in the current lab setup.

The incident He^{++} beam current is measures by the chopper, which samples the beam current at a constant rate; approximately 5% of the beam is intercepted by sampling. In the current lab setup, the IBeAM facility calibrates the chopper to a constant rate of 10^{-4} μC/count where count is the pulse count reading from the timer. A typical spectrum is taken for the duration of 10,000 to 100,000 counts depending on the desired counting statistics (smoothness of the spectra).

4.3.3 Data Analysis

4.3.3.1 Si Signal Leading Edge Determination and Background Noise Subtraction

As shown in Equation (9), due to energy straggling and the detector resolution, the Si signal detected at the highest energy from the bulk surface will have a spread. To determine the Si signal at highest energy, Si signal is determined via interpolations of the background noise, Si signal detected at the highest energy (referred to as "Si leading edge" from this point on), and Si bulk signal as shown in Figure 22. The linear regression line of the Si signal detected at the highest energy intersects with both the background noise and Si bulk signal. The mid-point energy of the two intersections is obtained as shown in Figure 22, i.e. Si leading edge energy.

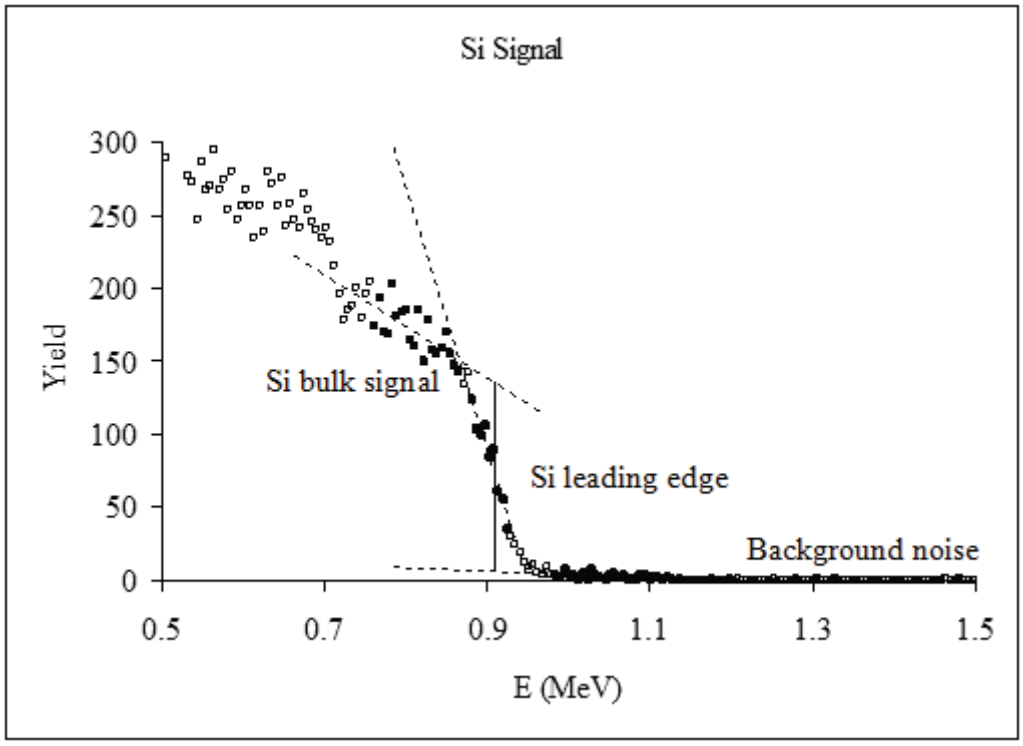

Figure 22.

RBS Si signal determination at 2 MeV He^{++} on HPMC cellulose film on Si-based substrates. Si leading edge is the Si signal detected at the highest energy. Yield is based on a silica wafer substrate in this example, with the same concept applicable to other Si-based substrates as well.

4.3.3.2 Energy loss of the Si Leading Edge due to the Film

Energy loss of the Si signal was used in the present investigation to measure the thickness of the HMPC cellulose film. In other words, the energy loss of He^{++} within the film shifts the Si signal from the substrate underneath, even if the polymer film itself cannot be detected by RBS, as shown in Figure 23 where only the Si signal can be detected, and the subsequent energy loss measured. The atoms from the film itself are undetected.

The Si leading edge shift with and without the HPMC cellulose film is observed in the RBS spectra. Figure 23 shows the energy loss of various RBS spectra taken as incident beam flux density increases. The HPMC areal density can be determined using Equation (12).

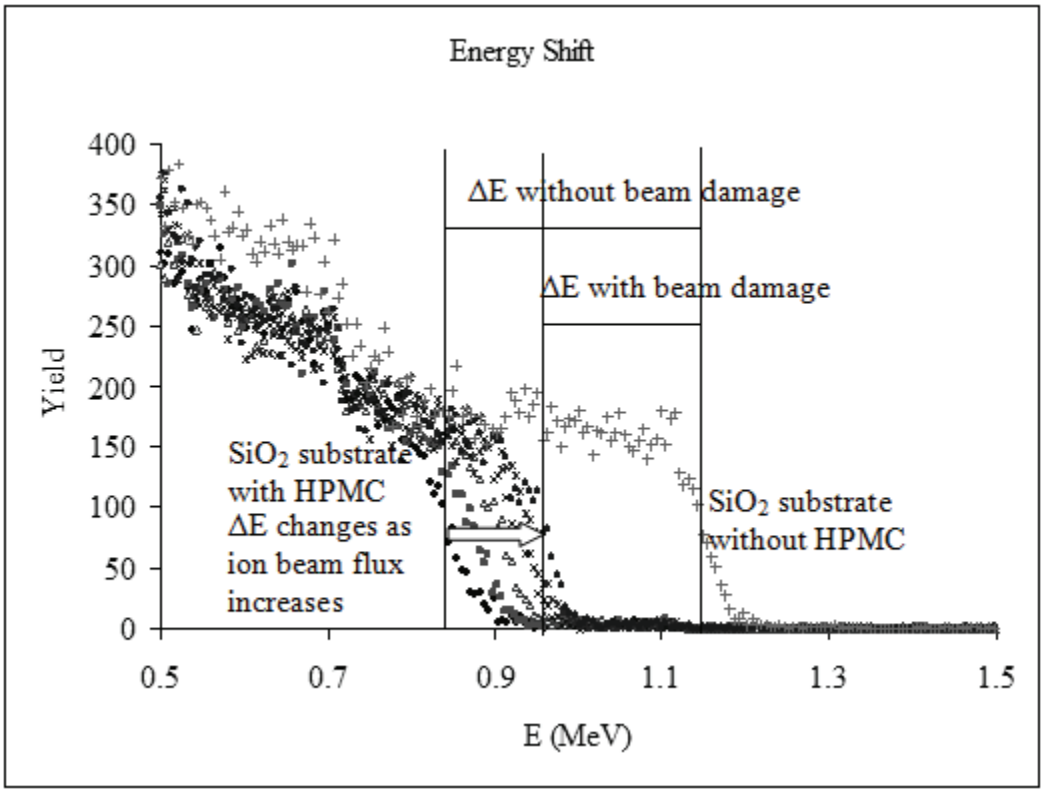

Figure 23.

RBS Si signal energy loss with and without HPMC cellulose film, the shift changes as incident He^{++} at 2 MeV increases every 1.1 $\mu C/mm^2$ of current density flux. Silica wafer substrate is used in this example, with the same concept applicable to the PDMS silicone substrate.

4.3.3.3 Damage Curve Regression and Analysis

Ion beam damage in polymer films is a well known and problematic issue [75, 91, 92]. The concept and implementation of the damage curve was necessary

since even a small flux of He^{++} causes a reduction in polymer film areal density measurement as seen in Figure 23. The energy loss of the silicon signal edge towards higher energies as the analyzing flux increases scales linearly with the loss of areal density of the film as atoms are ejected by collisions and the film thins, as expected from electronic energy loss theory.

The damaged region from the incident ion beam is visually evident on to the sample surface, where the normally transparent cellulose visibly darkens. The size of this region depends also upon the incident angle. Therefore, it was necessary to construct damage curves as a function of the cumulative incident ion beam flux, and then extrapolate the damage curve to the intercept for a zero ion flux, to find the backscattering yield prior to ion beam damage in the polymer film. The areal density prior to damage is found using exponential regression modeling as the damage curve for HPMC cellulose is found to be best fitted using an exponential decrease of the backscattering signal as a function of the cumulative ion flux.

Identification of an exponential model for the regression to account for the ion beam damage during IBA is a unique feature of the analysis used in this work. Ion beam damage typically scales linearly with the cumulative flux, as found for example for oxygen signals in silica and high density polymers [21, 27, 93]. However, the experimental evidence from the damage curves measured in the present investigation shows a much stronger correlation with an exponential model for atom ejection and areal density decrease as a function of ion flux. This

may be due to the high hydrogen content and light average atomic weight of cellulose.

Also, the open network model for the microstructure of the hydrophilic mesh model would facilitate a much more effective and rapid desorption and ejection of light atoms during ion beam damage than in high density polymers. Hence, an exponential model for the regression on the damage curve is a unique finding of this work. To ascertain this finding independently, the results of the present exponential fit will be used to extract the measured C and O stoichiometry of the cellulose ($C_{32}H_{60}O_{19}$) and compared to its expected ratio of 1.68. It will also provide an error range.

Generation of the damage curves allows for the use of IBA as an analysis tool on films that are particularly sensitive and significantly damaged during the IBA measurement process, as Figure 24 demonstrates.

Uncertainty of the areal density measurement is obtained through error propagation of the regression modeling parameters. Areal density of the HPMC cellulose adsorbates is shown in Table 2.

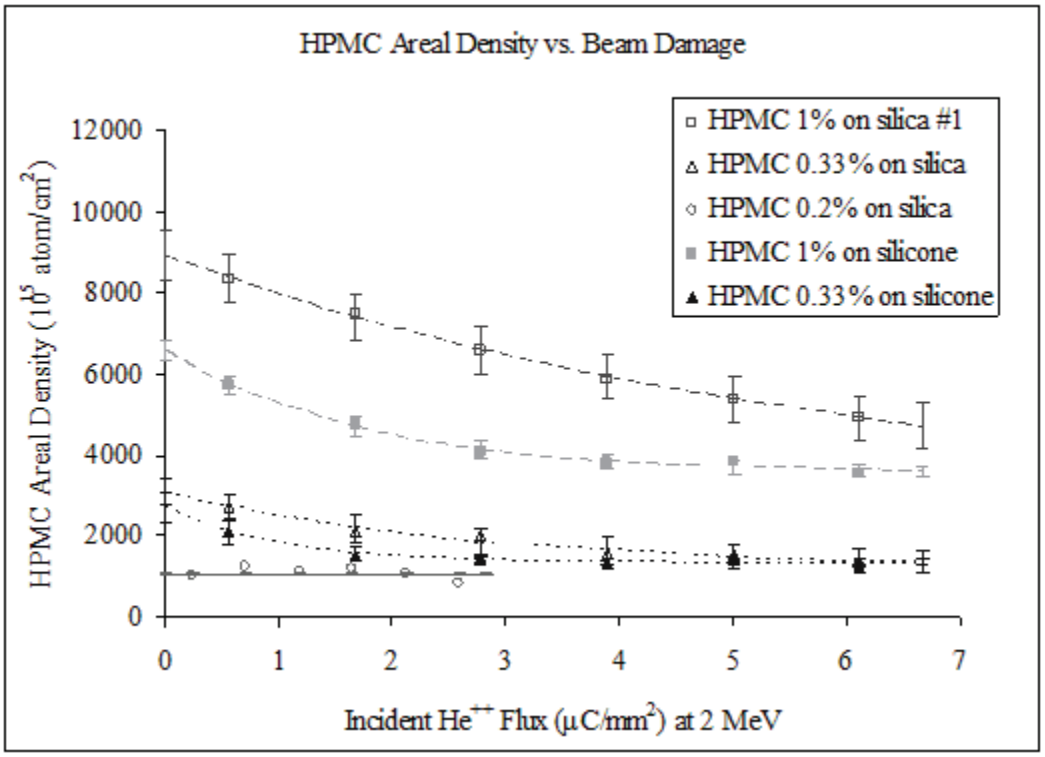

Figure 24.

Damage curves generated from hydrated HPMC cellulose film of concentrations ranging from 0.2% wt. to 1.0% wt. applied on silica wafer and PDMS silicone substrates. Note that the 0.2% wt. sample has a lower flux density range because of a different incident angle described in the above "Experiment Design" section.

Table 2.

HPMC cellulose gel concentration during the preparation of the dried film vs. areal density of the dried film determined using RBS on silica wafer and PDMS silicone substrates.

Substrate Type	Gel Concentration (% wt.)	Film Areal Density (10^{15} atom/cm^2)
Silica Wafer	1% Sample #1	8920 ± 620
Silica Wafer	1% Sample #2	9680 ± 210
Silica Wafer	1% Sample #3	8350 ± 700
Silica Wafer	0.33%	3100 ± 310
Silica Wafer	0.25%	1087 ± 25
Silica Wafer	0.2%	1086 ± 55
PDMS silicone	1%	6570 ± 250
PDMS silicone	0.33%	2730 ± 380

4.4 HPMC Stoichiometry via Nuclear Resonance Scattering

4.4.1 Density Ratio via Enhanced Resonance Scattering Cross Section

HPMC cellulose consists of lighter C and O atoms which are typically difficult to detect on heavier substrates with a high degree of resolution [94]. By using 4.265 MeV $^{12}C(\alpha, \alpha)^{12}C$ and 3.045 MeV $^{16}O(\alpha, \alpha)^{16}O$, one can determine the carbon versus oxygen composition at high resolution near the surface [94, 95]. Since C and O resonate at different energy, they cannot be in a same spectrum for

direct comparison. Therefore, Si is used as a calibration element assuming N_{Si} does not change for the same sample.

The carbon and oxygen ratio can then be estimated using Equation (5) with n as the element signal height obtained from the spectra,

$$\frac{N_C}{N_O} = \frac{\frac{\sigma_{Si}(E_C)}{\sigma_C(E_C)} \cdot \frac{H_C(E_C)}{H_{Si}(E_C)}}{\frac{\sigma_{Si}(E_O)}{\sigma_O(E_O)} \cdot \frac{H_O(E_O)}{H_{Si}(E_O)}} \tag{13}$$

with

$N_{C,O,Si}$ is the atomic density of elements identified by the subscript,

$H_{C,O,Si}$ is the signal height in the spectra, subscript represents the element,

$\sigma_{C,O,Si}$ is the scattering cross sections of the respective element,

$E_{C,O}$ is the energy at which the spectrum is taken, i.e. 4.265 MeV and 3.045 MeV respectively.

4.4.2 Experimental Design

The HPMC cellulose film on Si-based substrates is separately measured for the height of the carbon and oxygen signals at incident beam energies of 4.265 ± 0.055 MeV and 3.045 ± 0.005 MeV, respectively. To maintain consistency, the Si signal is used to normalize all spectra. The incident beam is normal to the sample, with the detector angle at 170°, with a He^{++} beam current of about 20 nA.

Sample charging can be an issue when using an insulating substrate and film [96-99]. A built-in advantage of using nuclear resonance analysis is that charging is quickly detected by the energy shift of the incident ions and decay in

resonance. This built-in energy calibration during charging facilitated maintaining the resonance and a stable measurement on extremely difficult to measure materials. Sample charging due to the ion beam incidence was observed for both the silica wafer and the PDMS silicone lens samples. To help mitigate this charging effect, the sample was grounded by wrapped with aluminum foil; with a 4 mm to 10 mm diameter hole for the ion charges to be easily removed from the surface and allowed for consistent, reproducible data collection. However, the charging effect still was significant enough to require an offset in terminal voltage to compensate for the required resonance energy; and hence this offset had to be introduced even after adding a conducting aluminum wrapping around the samples. Resonance yield was thus not maximized by reading the fixed terminal voltage based on the energy and the energy spread of carbon resonance of 4.265 ± 0.055 MeV and oxygen resonance of 3.045 ± 0.005 MeV. Instead the scattering yield was maximized above the center values of the respective resonances of 4.265 MeV and 3.045 MeV by increasing the offset voltage to compensate for the charging effects unique to each sample and attain the self-calibrating effective resonance energy for reproducible collection of the IBA spectra. The experiment was conducted in vacuum of 10^{-7} Torr to 10^{-6} Torr.

4.4.3 Data Analysis

4.4.3.1 Background Subtraction

3.045 MeV $^{16}O(\alpha, \alpha)^{16}O$ spectrum is shown in Figure 25. Several simulations are done to analyze the case. Once we do a RUMP fitting, the areal density of the film is determined to be 4600 (10^{15} atom/cm^2) in this specific case.

We then can simulate the case without oxygen resonance. Two distinct oxygen edges are shown; the high energy edge is from the HPMC cellulose film surface, while the lower energy edge is from the silica wafer substrate. By comparing line 2 and line 3, we can determine that the substrate oxygen edge falls out of the resonance peak. Therefore, we can analyze the oxygen resonance peak without the interference from the oxygen in the substrate. However, this also implies that we cannot subtract the left-hand-side background, as the left hand side includes the oxygen signal from the bulk which does not exist underneath the resonance peak. Ideally, we would like to subtract the background to achieve what's shown in line 6 with HPMC cellulose only and no substrate. Line 4 and line 5 show the simulation of bare silica wafer substrate without HPMC film as a reference.

Figure 26 zoomed in on the oxygen resonance region similar to Figure 25. Oxygen signal height is obtained by subtracting the linear regression line of the Si bulk signal from oxygen peak (height between P1 and P2), i.e. the oxygen signal height from the net oxygen peak after background subtraction. This concept is based on the observation that the oxygen from the silica substrate falls to the left-hand-side of the resonance peak region. We also verified from the simulation that the oxygen signal height obtained from the background subtraction is the same as the oxygen peak height without the silica substrate (height between Q1 and Q2).

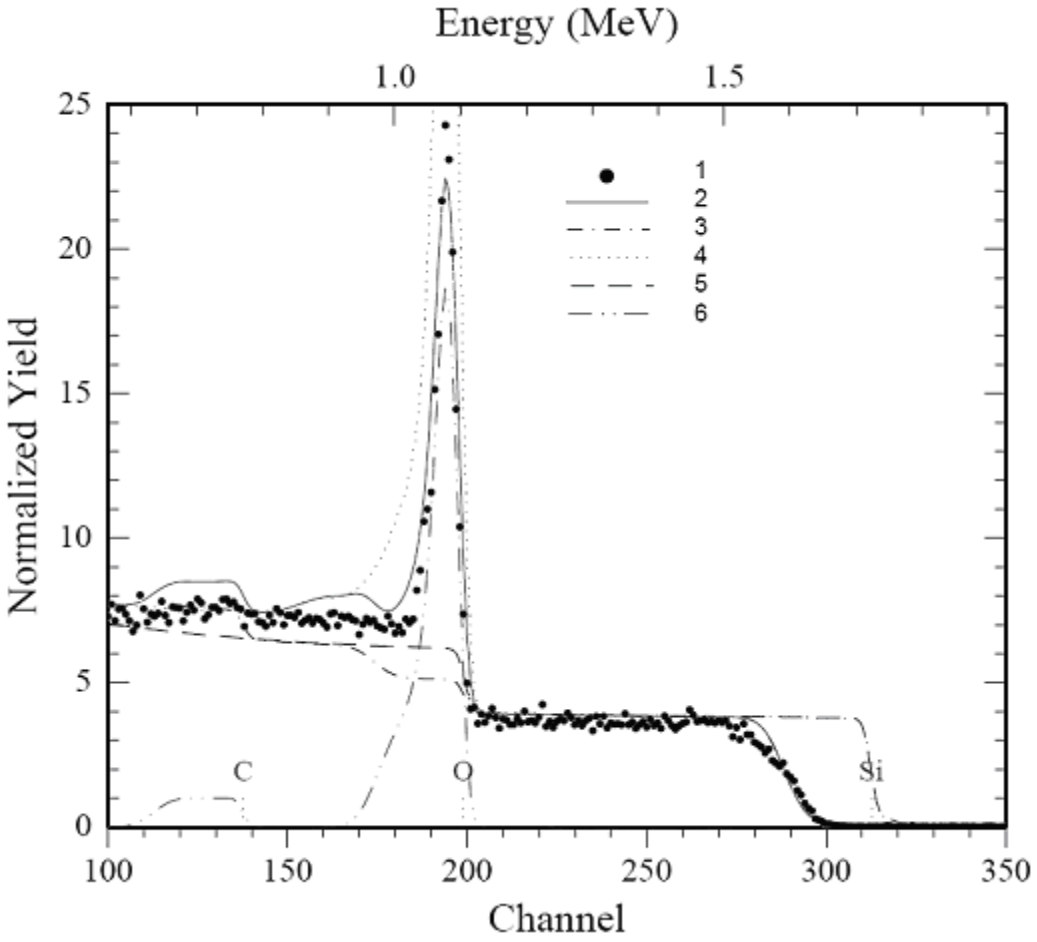

Figure 25.

HPMC cellulose film on silica wafer substrate, showing 3.045 MeV $^{16}O(\alpha, \alpha)^{16}O$. Symbol 1 (round dot) is the actual spectrum. Line 2 (solid line) is a RUMP simulation showing an excellent fitting to the original spectrum where we can obtain the areal density of the $C_{32}H_{60}O_{19}$ film to be 4600 (10^{15} atom/cm^2). Line 3 is the RUMP simulation similar to line 2, but without the O resonance; where we can identity two edges for oxygen. Line 4 is the RUMP simulation of the silica wafer substrate only, without HPMC cellulose film. Line 5 is the RUMP simulation similar to line 4, but without O resonance. Line 6 is the RUMP simulation of the HPMC film only without silica substrate.

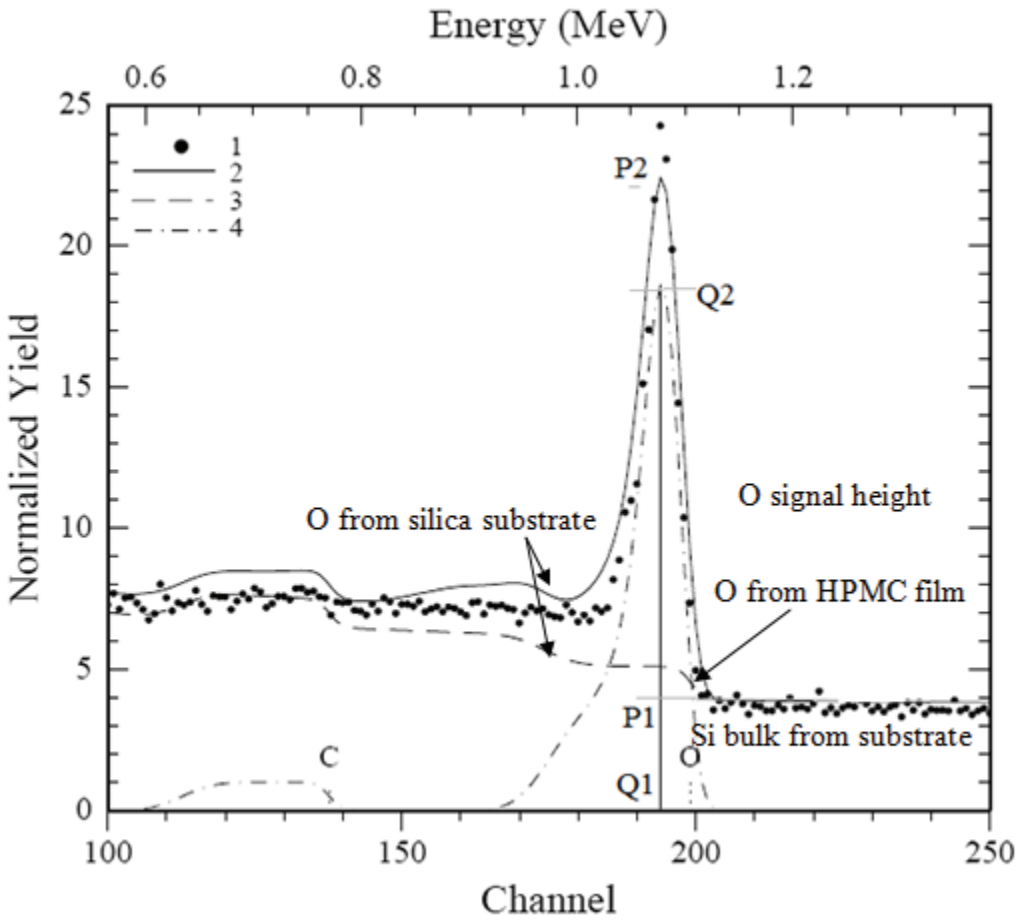

Figure 26.

HPMC cellulose film on silica wafer substrate, showing oxygen signal height determination at 3.045 MeV $^{16}O(\alpha, \alpha)^{16}O$. Symbol 1 (round dot) is the actual spectrum. Line 2 (solid line) is a RUMP simulation showing an excellent fitting to the original spectrum where we can obtain the areal density of the $C_{32}H_{60}O_{19}$ film to be 4600 (10^{15} atom/cm^2). Line 3 is the RUMP simulation similar to line 2, but without the O resonance; where we can identity two edges for oxygen. Line 4 is the RUMP simulation of the HPMC film without the silica substrate.

The Si signal height is determined from the linear regression lines of the Si substrate signal, background noise, and the Si leading edge as shown in Figure

27. The regression line of the Si leading edge intersects with both the Si bulk signal to the left and the background noise to the right. The Si signal height is obtained by measuring the (perpendicular) distance between the left-hand-side intersection and the right-hand-side intersection, as shown in Figure 27.

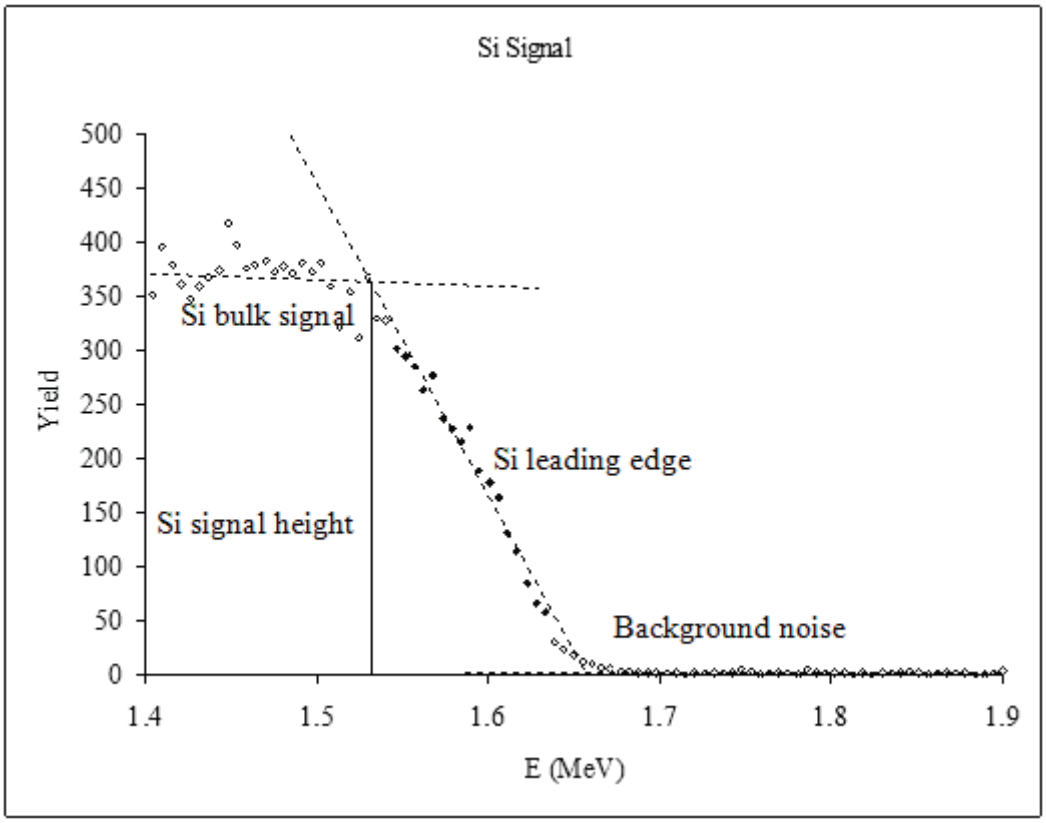

Figure 27.

HPMC cellulose on Si-based substrates (silica wafer substrate is used in this example, same concept is applicable to PDMS silicone substrate), and the subsequent silicon signal height determination at 3.045 MeV $^{16}O(\alpha, \alpha)^{16}O$. In this example, the height of the silicon signal is approximately 370 counts.

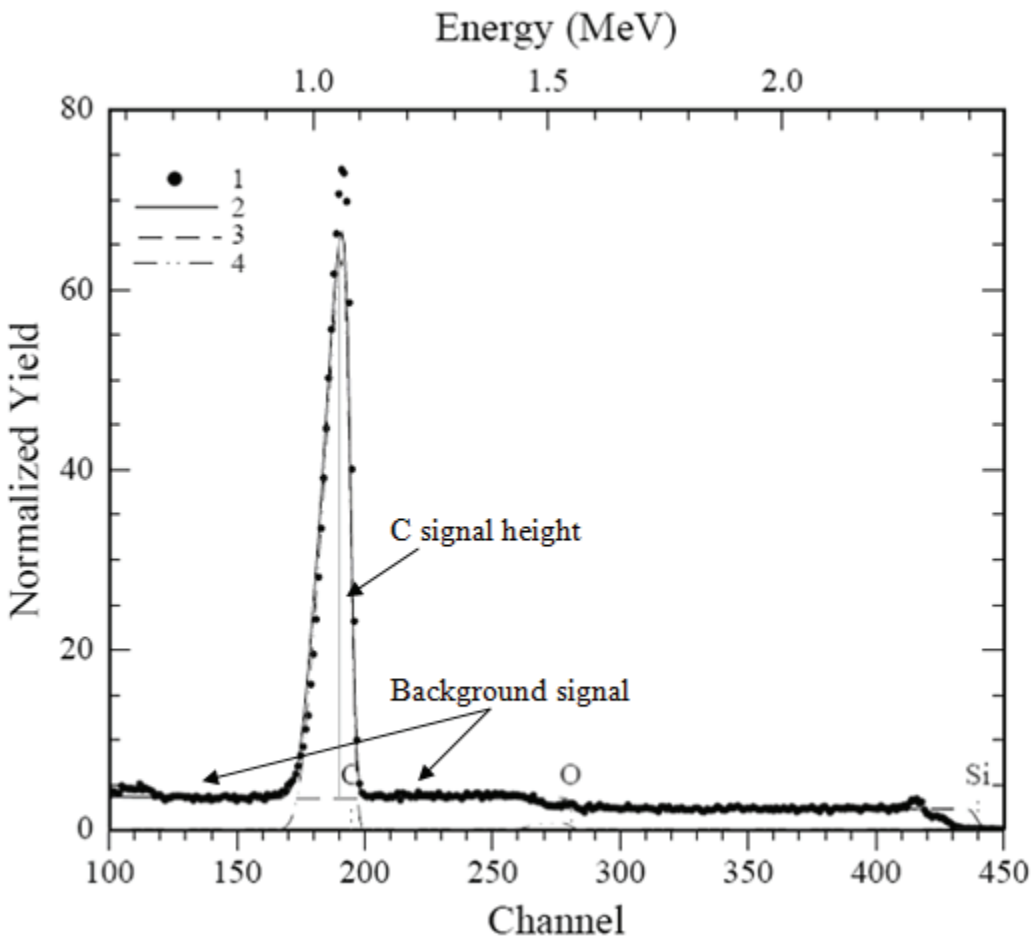

Figure 28.

HPMC cellulose film on silica wafer substrate, showing 4.265 MeV $^{12}C(\alpha, \alpha)^{12}C$. Symbol 1 (round dot) is the actual spectrum. Line 2 (solid line) is a RUMP simulation showing an excellent fitting to the original spectrum where we can obtain the areal density of the $C_{32}H_{60}O_{19}$ film to be 3500 (10^{15} atom/cm^2). Line 3 is the RUMP simulation of the silica wafer substrate only, without HPMC cellulose film. Line 4 is the RUMP simulation of the HPMC film only without silica substrate.

4.265 MeV $^{12}C(\alpha, \alpha)^{12}C$ spectrum is shown in Figure 28. Several simulations are done to analyze the case. Once we do a RUMP fitting, the areal

density of the $C_{32}H_{60}O_{19}$ film is determined to be 3500 (10^{15} atom/cm^2) in this specific case. Since carbon does not exist in the substrate, we can analyze the carbon resonance peak by subtracting the total background. We also verified from the simulation that the carbon signal height obtained from the background subtraction is the same as what is shown by line 4 with HPMC cellulose only and not the substrate. Line 3 shows the simulation of silica wafer substrate without HPMC film as a reference.

4.4.3.2 Stoichiometry Determination with Damage Curve Analysis

Ion beam damage in HPMC cellulose films is accounted for by using interpolation on the sequential damage curves shown in Figure 29 and Figure 30. The exponential extrapolation of the scattering yield for both oxygen and carbon resonance to zero beam flux density can then be used to determine the initial yield prior to damage from the analysis and the subsequent areal density measurement through regression modeling.

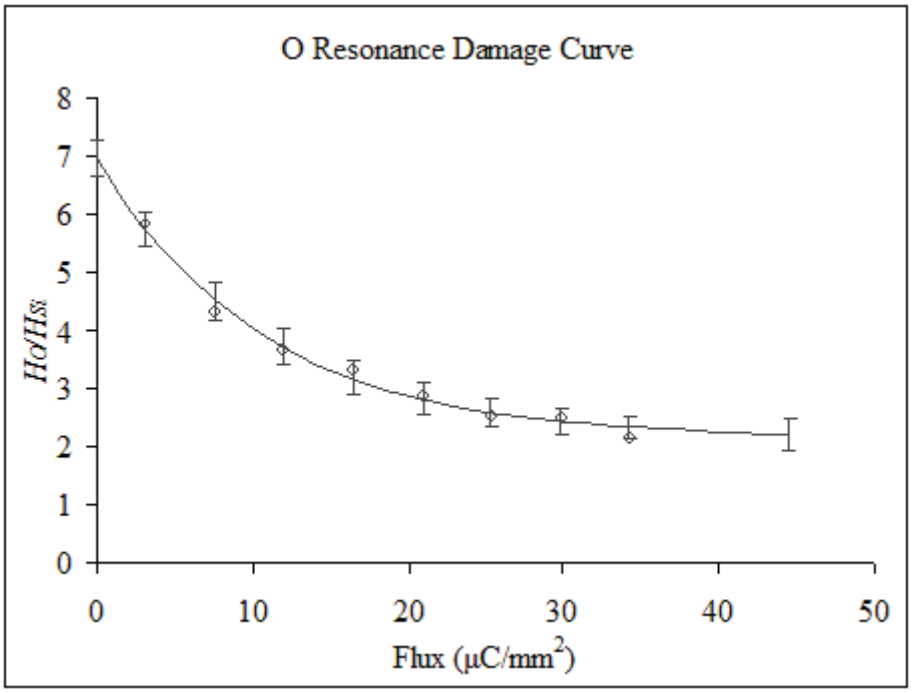

Figure 29.

Damage curve of HPMC cellulose at 3.045 MeV He^{++}. Extrapolation of the normalized oxygen signal height. The y-intercept is the extrapolated oxygen signal height without ion beam damage.

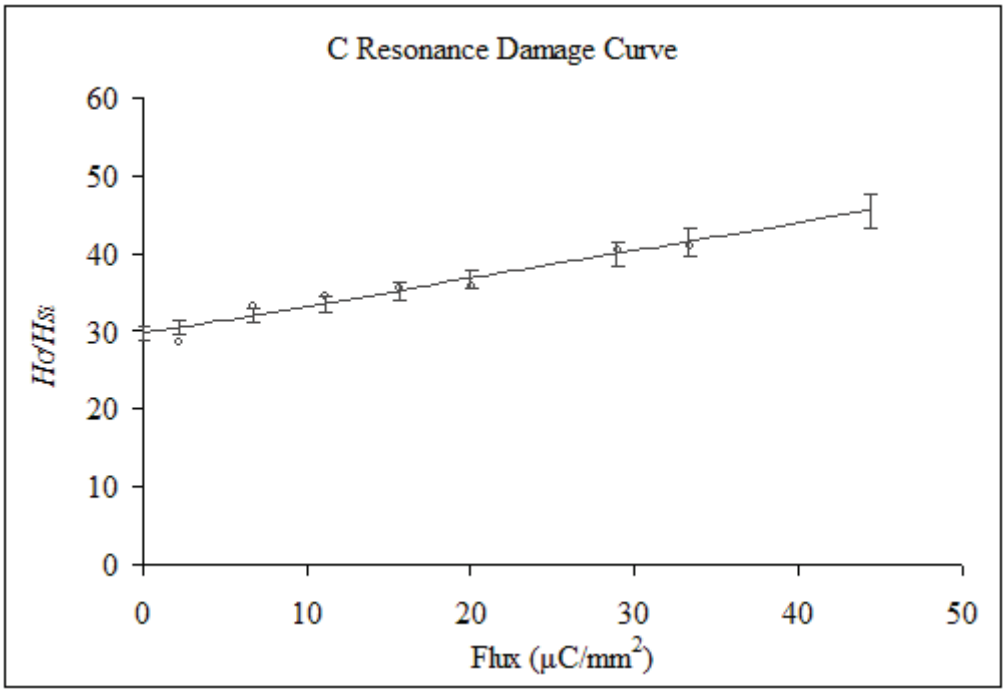

Figure 30.

Damage curve of HPMC cellulose at 4.265 MeV He^{++}. Extrapolation of the normalized carbon signal height. The y-intercept at zero flux is the extrapolated carbon signal height without ion beam damage.

Replace the extrapolated values $\left.\frac{H_C}{H_{Si}}\right|_{4.265MeV}$ and $\left.\frac{H_O}{H_{Si}}\right|_{3.045MeV}$ in Equation (13) and (4), together with the nuclear resonance cross section enhancement factors, we thus determined the $\frac{N_C}{N_O} = 1.60 \pm 0.08$. The uncertainty is obtained through error propagation of the regression parameters. By computing the surface stoichiometric ratio this way, the accuracy of the exponential regression model proposed here is demonstrated by the excellent agreement with the expected bulk stoichiometric ratio for $C_{32}H_{60}O_{19}$ cellulose, or $\frac{32}{19} \approx 1.68$.

In summary, the analysis of damage curves enables an accurate counting of C and O atoms in HPMC cellulose adsorbates, which can lead to an accurate measurement of the areal density and thin film thickness if the accurate yields obtained by exponential interpolation are calibrated with a substrate signal.

A reliable signal in Si-based substrates is obtained from the heavier Si atoms, if again the stoichiometry of the substrate can be accurately extracted from the data. Since the stoichiometry of the PDMS silicone and silica substrates remains constant while the dilution of the hydrophilic emulsion, and thus the net amount of HMPC cellulose varies, the constant stoichiometry of PDMS silicone and the silicon height is a good choice to calibrate the signal heights of O and C.

4.5 PDMS Silicone Substrate Stoichiometry via Nuclear Resonance Scattering

4.5.1 Density Ratio via Enhanced Resonance Scattering Cross Section

Similar to the section above about calculating HPMC cellulose stoichiometric ratio, we now determine C, O, and Si for the PDMS silicone substrate. We approach this by determining the ratio separately, and then combining them under the assumption that N_{Si} remains the same.

$$\frac{N_{C,O}}{N_{Si}} = \frac{\sigma_{Si}}{\sigma_{C,O}} \cdot \frac{H_{C,O}}{H_{Si}} \tag{14}$$

with

$N_{C,O,Si}$ is the atomic density of elements identified by the subscript,

$H_{C,O,Si}$ is the signal height in the spectra, subscript represents the element,

$\sigma_{C,O,Si}$ is the scattering cross sections of the respective element at a given energy.

4.5.2 Experimental Design

PDMS silicone consists of carbon based molecules attached to a repetitive silicon-oxygen backbone. As found in the case of HPMC cellulose, the lighter C and O atoms in PDMS silicone again are typically difficult to detect on heavier substrates (the silicon) with a high degree of resolution. Hence, the same method developed for the HPMC cellulose can be applied to the PDMS silicone substrates.

By using again 4.265 MeV $^{12}C(\alpha, \alpha)^{12}C$ and 3.045 MeV $^{16}O(\alpha, \alpha)^{16}O$ nuclear resonance scattering, one can determine the stoichiometry at high resolution near the PDMS silicone surface. The incident beam is 8° to the sample normal; the detector angle is again 170°, along with a similar beam current of approximately 20 nA.

4.5.3 Data Analysis

4.5.3.1 Background Subtraction

Figure 31 shows PDMS silicone $SiOC_2H_6$ at 3.045 MeV $^{16}O(\alpha, \alpha)^{16}O$. Symbol “round dot” is the actual spectrum taken. The RUMP simulation is an excellent fit to the original spectrum, and we can confirm the material has a stoichiometry close to $SiOC_2H_6$. The net oxygen peak is determined by four points as shown in Figure 31.

Figure 32 shows PDMS silicone $SiOC_2H_6$ at 4.265 MeV $^{12}C(\alpha, \alpha)^{12}C$. The RUMP simulation showing an excellent fitting to the original spectrum where we can confirm the material has a stoichiometry close to $SiOC_2H_6$. The net carbon peak is determined by four points as shown in Figure 32 which is similar to the oxygen case described above.

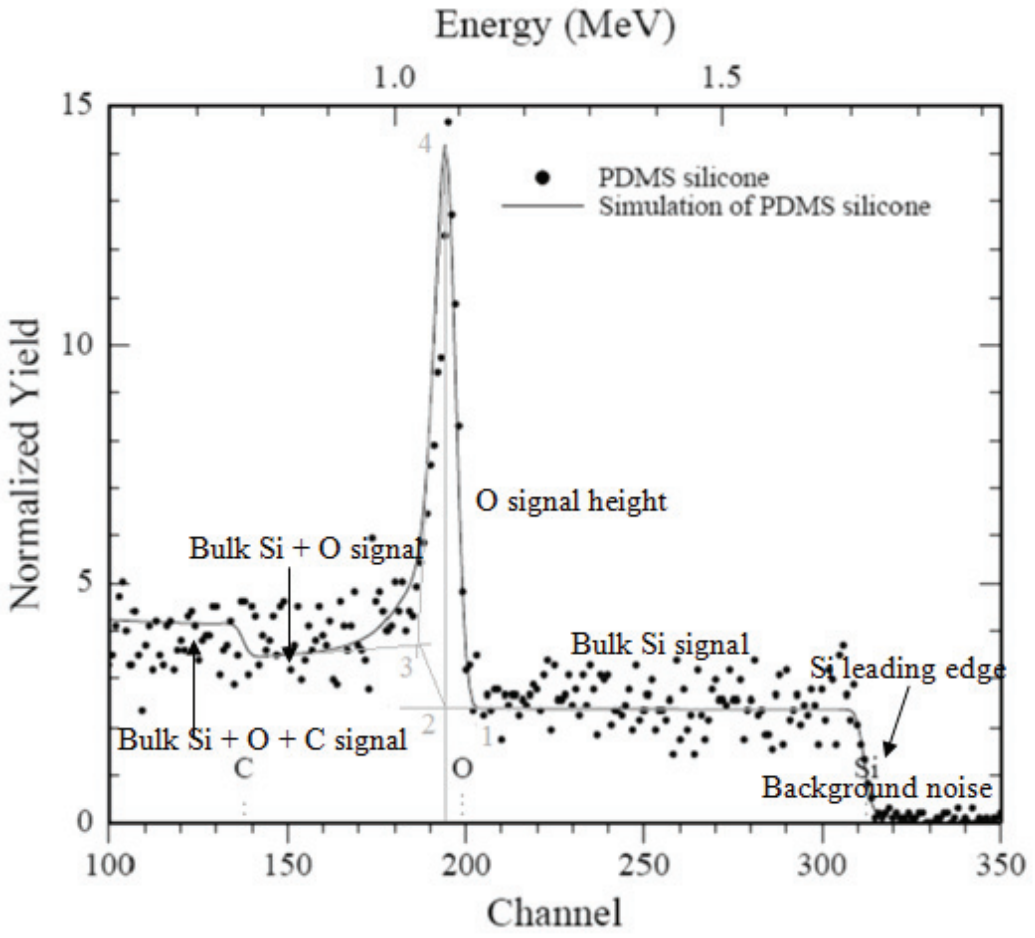

Figure 31.

PDMS silicone $SiOC_2H_6$ at 3.045 MeV $^{16}O(\alpha, \alpha)^{16}O$. Symbol "round dot" is the actual spectrum taken by RBS. The "solid line" is a RUMP simulation showing an excellent fitting to the original spectrum where we can confirm the material has a stoichiometry close to $SiOC_2H_6$. Point 1 is the intersection between the extension of the right-hand-side of the oxygen peak and the right-hand-side of the bulk signal, point 2 is the intersection between the vertical line from the oxygen resonance peak and the bulk signal from the right-hand-side, point 3 is the intersection between the extension of the left-hand-side of the oxygen peak and the left-hand-side of the bulk signal, and point 4 is the oxygen resonance peak.

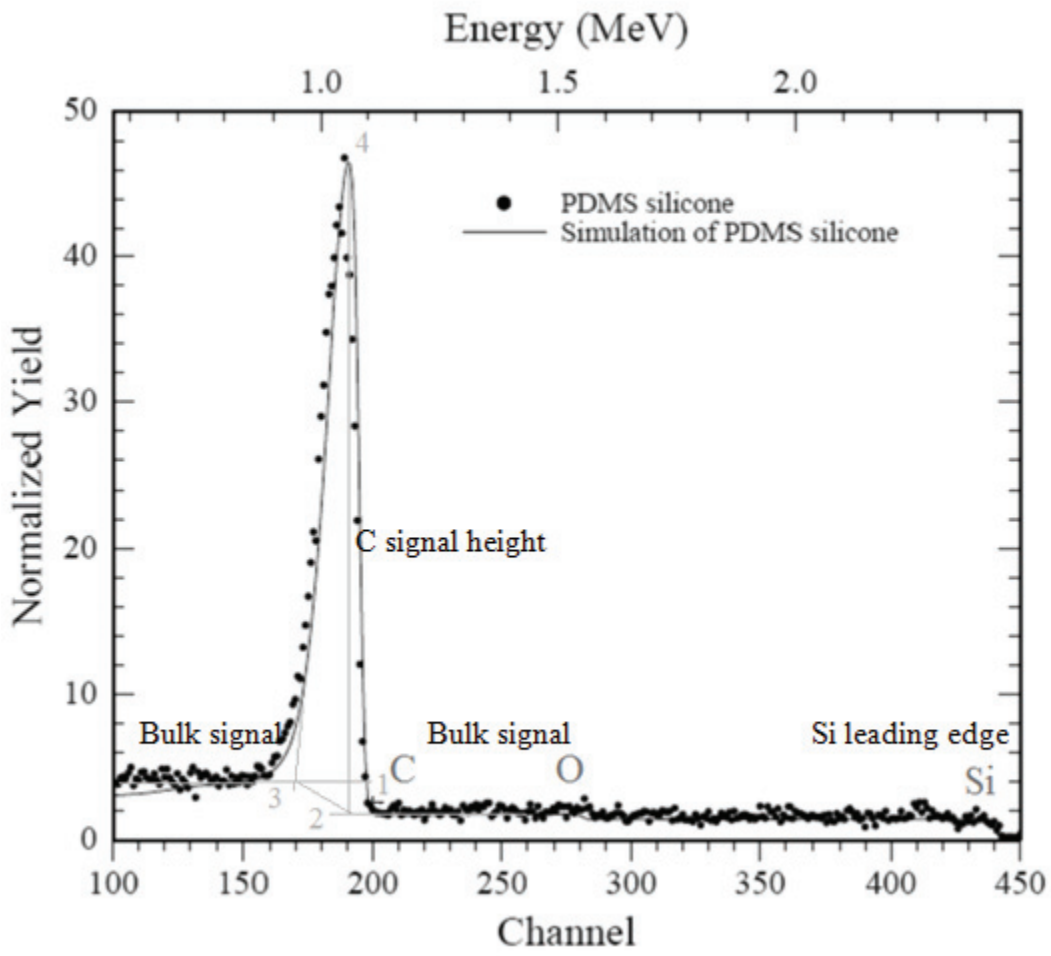

Figure 32.

PDMS silicone $SiOC_2H_6$ at 4.265 MeV $^{12}C(\alpha, \alpha)^{12}C$. Symbol "round dot" is the actual spectrum. The "solid line" is a RUMP simulation showing an excellent fitting to the original spectrum where we can confirm the material has a stoichiometry close to $SiOC_2H_6$.

4.5.3.2 Stoichiometry Determination with Damage Curve Analysis

Ion beam damage in PDMS silicone polymers can also be measured by generating damage curves, as shown in Figure 33 and Figure 34. The measured yields as a function of cumulative analyzing flux density can then be used to

extrapolate to the net yield prior to damage to obtain the net areal density by using again exponential regression. An accurate height of the surface silicon signal is necessary to normalize the oxygen nuclear resonance scattering signal height to enable direct comparison between spectra, since the silicon signal height versus the flux of He^{++} always remains constant, unlike the HPMC cellulose coverage which is the object of this measurement.

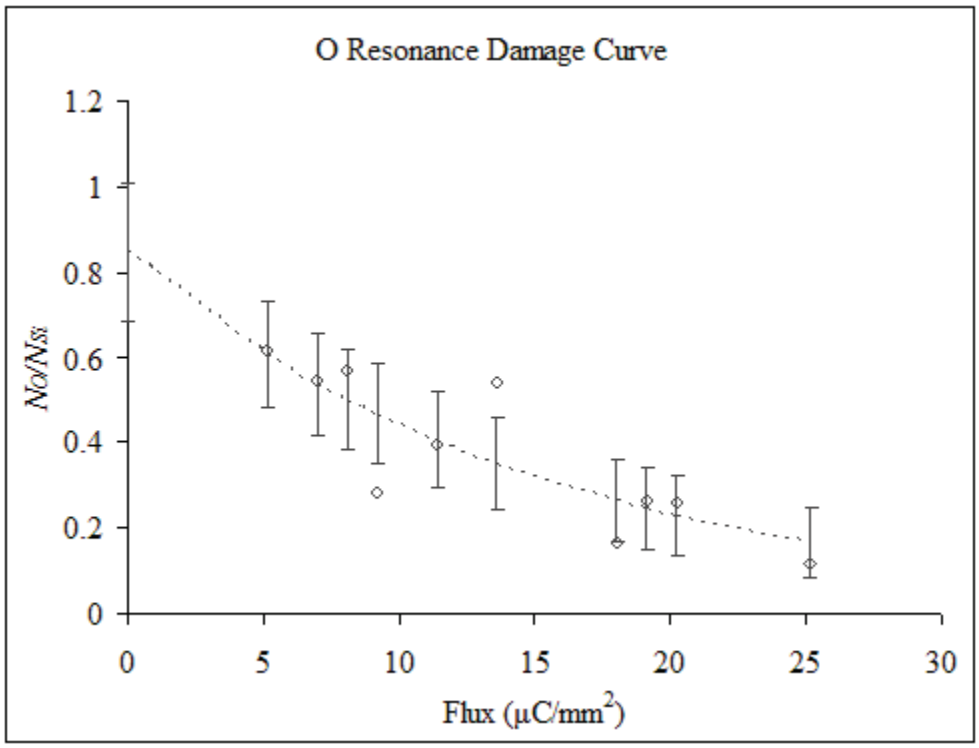

Figure 33.

IBMM of PDMS silicone Extrapolation of the normalized oxygen signal height without ion beam damage occurs at the y-intercept.

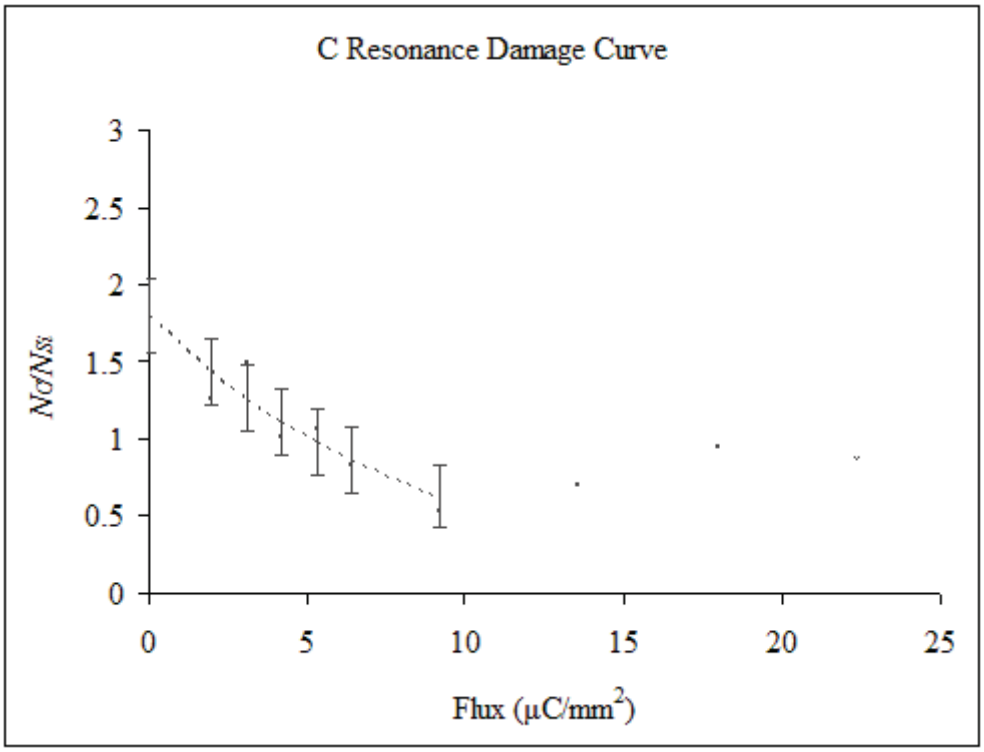

Figure 34.

IBMM of PDMS silicone; extrapolation of the normalized carbon signal height without ion beam damage occurs at the y-intercept.

The rate of oxygen loss in PDMS silicone within the resonated surface is found again to be best fitted as an exponentially decreasing function. However, carbon regression was only taken into consideration when the He^{++} flux is less than 10 $\mu C/mm^2$. The change of surface carbon was determined using the nuclear resonance scattering carbon signal height normalized by the surface silicon signal height as well. The normalization not only allows for the comparison amongst the carbon spectra, but also provides a relative scale to compare the carbon and oxygen amounts. The carbon damage curve trend changes significantly from an exponential behavior afterwards as can be seen in Figure 34, most likely due to a

phase transformation. But, the exponential regression fits well for the first 6 initial flux points nearest the origin and can be used for finding the y-intercept.

The two resulting measured ratios yield the following results, $\frac{N_C}{N_{Si}} \approx 1.80 \pm 0.25$ and $\frac{N_O}{N_{Si}} \approx 0.85 \pm 0.16$. Uncertainty of the measurement is obtained through error propagation of the regression parameters. Stoichiometric ratios deviates from the expected PDMS silicone ($SiOC_2H_6$) stoichiometry, however, the IOL material is not standard PDMS silicone, it is a patented material based of PDMS silicone with composition unknown to us.

4.6 Stoichiometry and Areal Density via ERD

ERD is one of the few techniques that can measure areal densities and bulk densities of hydrogen [100, 101]. ERD can do both depth profiling of hydrogen and determine its areal density of hydrogen and that of other light elements by using direct heavy-ion elastic recoil detection [102, 103]. Therefore, by conducting ERD, not only we complete the stoichiometric ratios with hydrogen, but also verify independently the areal density.

4.6.1 Experimental Design Used for ERD in HPMC Cellulose and PDMS Silicone

ERD of hydrogen atoms is conducted to provide independent areal density measurements to compare with the above areal density measurements obtained from the energy loss method, via the hydrogen depth profiling. The measurement was optimized and the most useful incident analyzing beam was found to be consistent He^{++} at and energy of 2.8 MeV. These were then filtered out using a

10.6 μm mylar filter at the Si(Li) detector so that only recoiled hydrogen atoms from the film by high energy collisions with He^{++} are detected. The incident beam angle with the sample normal is 75°, while the forward scattering detector angle is 150°. Beam current is typically about 20 nA.

Surface charging due to the ion beam was again observed for both the PDMS silicone lens, and silica wafer substrate with HPMC cellulose adsorbates. Again, grounding the surface by wrapping the sample with an aluminum foil pierced with a 4 mm to 10 mm diameter hole, minimized the charging effect and allowed for consistent, reproducible data collection. The experiment was conducted in a vacuum of 10^{-7} Torr to 10^{-6} Torr.

4.6.2 Data Analysis

Using RUMP simulations, with a given ratio of other known components, i.e., C and O in HPMC cellulose and C, O, Si in PDMS silicone, we can adjust the relative proportion of the unknown hydrogen, until the simulation matches the ERD spectrum. From the simulations, we can obtain simultaneously, hydrogen proportion entered during the simulation and the depth profiling for hydrogen. To obtain the depth profiling of a film, the total areal density of the signal has to be integrated over the energy and convoluted with the variation of the scattering cross section as a function of energy. This has to be done with a finite element integration rather than algebra as was done for signal height analysis. Therefore, the RUMP software is used to determine

(a) relative proportion of hydrogen compare to other known proportions of elements, and

(b) as an independent test of this method, the areal density Nt of atoms in PDMS silicone and HPMC cellulose by comparing the relative hydrogen composition to the expected oxygen, carbon, and silicon in the polymers [104].

4.6.2.1 Hydrogen Yield Calibration in ERD

Since in ERD there is no signal detected besides the hydrogen yield, a calibration sample has to be used to obtain an absolute measurement and hydrogen content. Figure 35 shows the spectra calibration utilizing a calibration sample with polymer film with known composition and thickness or areal density. The samples used for calibration were produced in our group [21]. The polymer film has a composition of $C_{35}H_{22}N_2O_5$ and a known areal density of 550 (10^{15} atom/cm^2), yielding a hydrogen depth profiling including total counts scaling with the areal density. The calibration spectra should be rerun whenever the experiment condition changes, for an example, the change of the incident He^{++} energy occurs. The calibration process is optimizing the parameters in RUMP simulation to match the spectra.

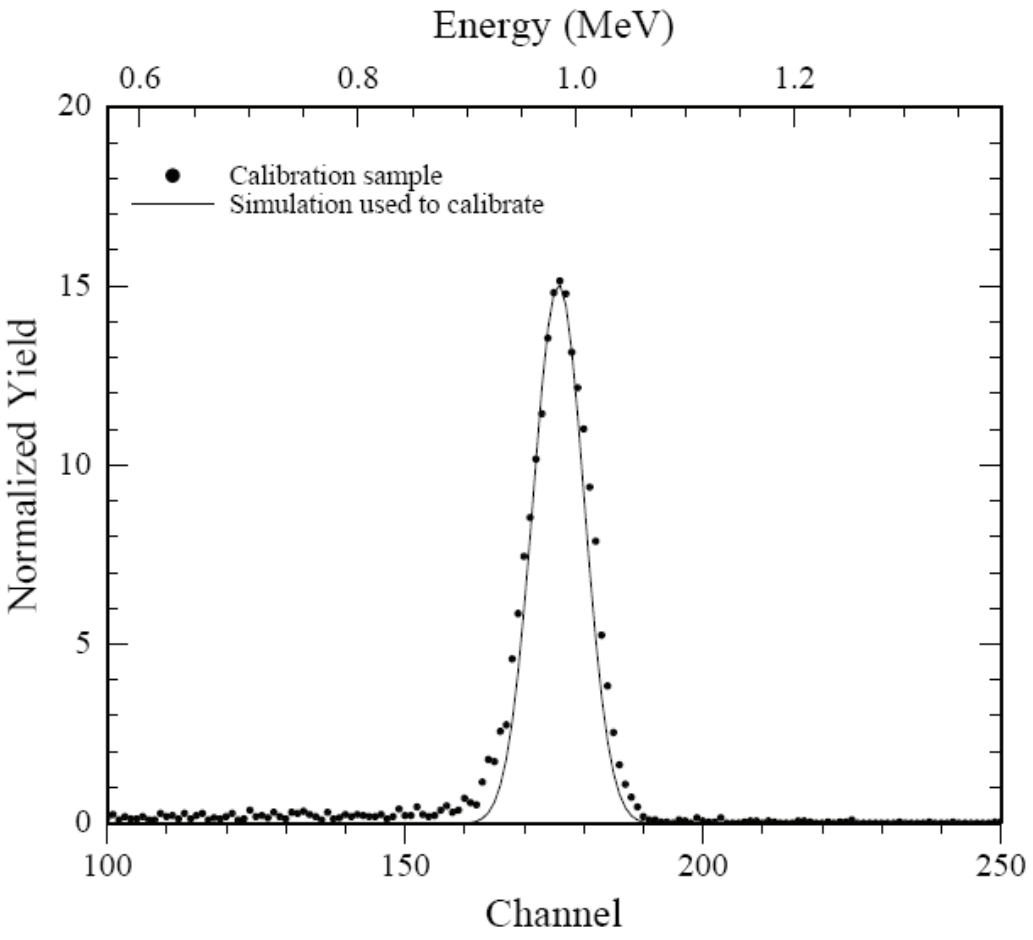

Figure 35.

Calibration with $C_{35}H_{22}N_2O_5$ and its areal density of 550 (10^{15} atom/cm^2) using RUMP computations.

4.6.2.2 Areal Density and Stoichiometry Determination of HPMC Cellulose

The spectrum of an HPMC cellulose polymer film measured by 2.8 MeV He^{++} and ERD combined with the RUMP simulation fitting curve is shown in Figure 36. The areal density of the hydrogen signal is found to be 11,600 (10^{15} atom/cm^2), with increments of 100 (10^{15} atom/cm^2) for the iteration step.

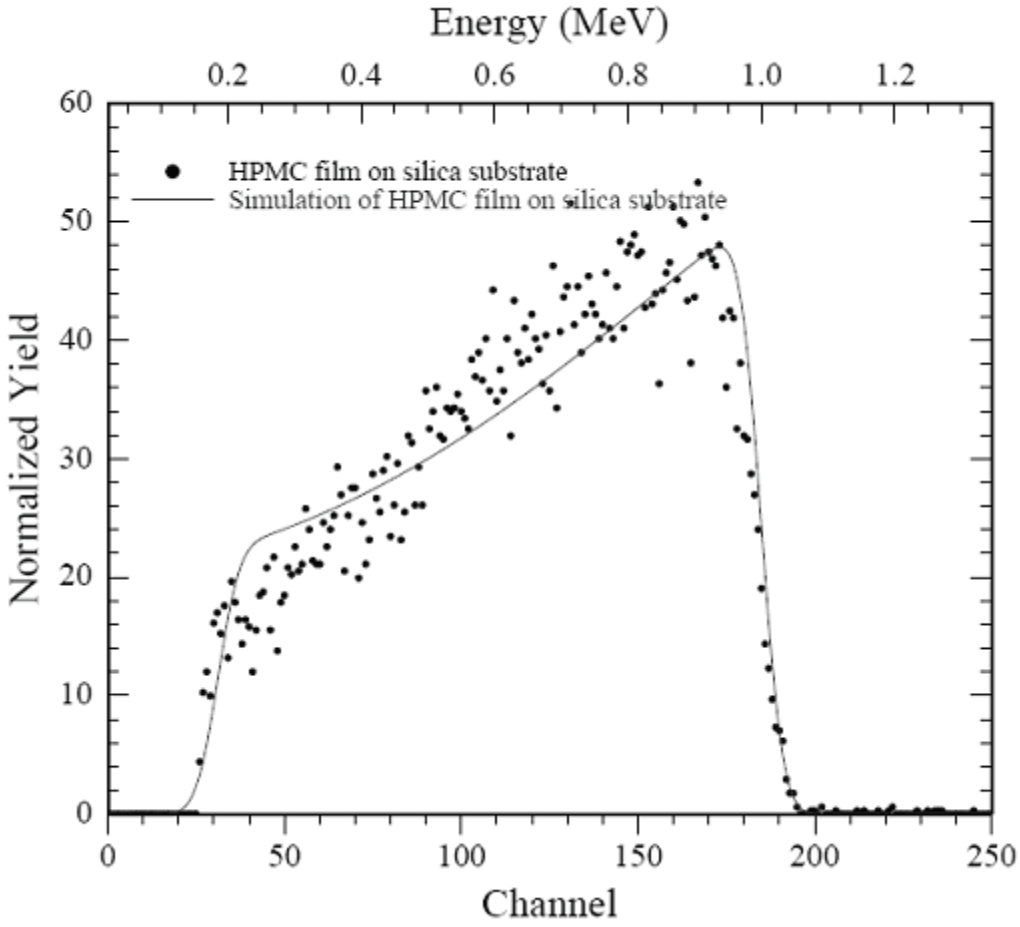

Figure 36.

ERD of HPMC cellulose film on silica substrate, with RUMP simulation. The simulation gives an areal density of 1.16×10^{19} hydrogen atom/cm^2 in the dried from original concentration 1% wt. HPMC cellulose film.

The areal density measured by ERD was then compared to the areal density measured by RBS on the same sample. Both methods are found be in agreement. The areal density that was extracted using the Si signal energy loss method, gave values ranging 12000 (10^{15} atom/cm^2) to 13000 (10^{15} atom/cm^2) from the computations for areal density shown in Figure 37 using RUMP.

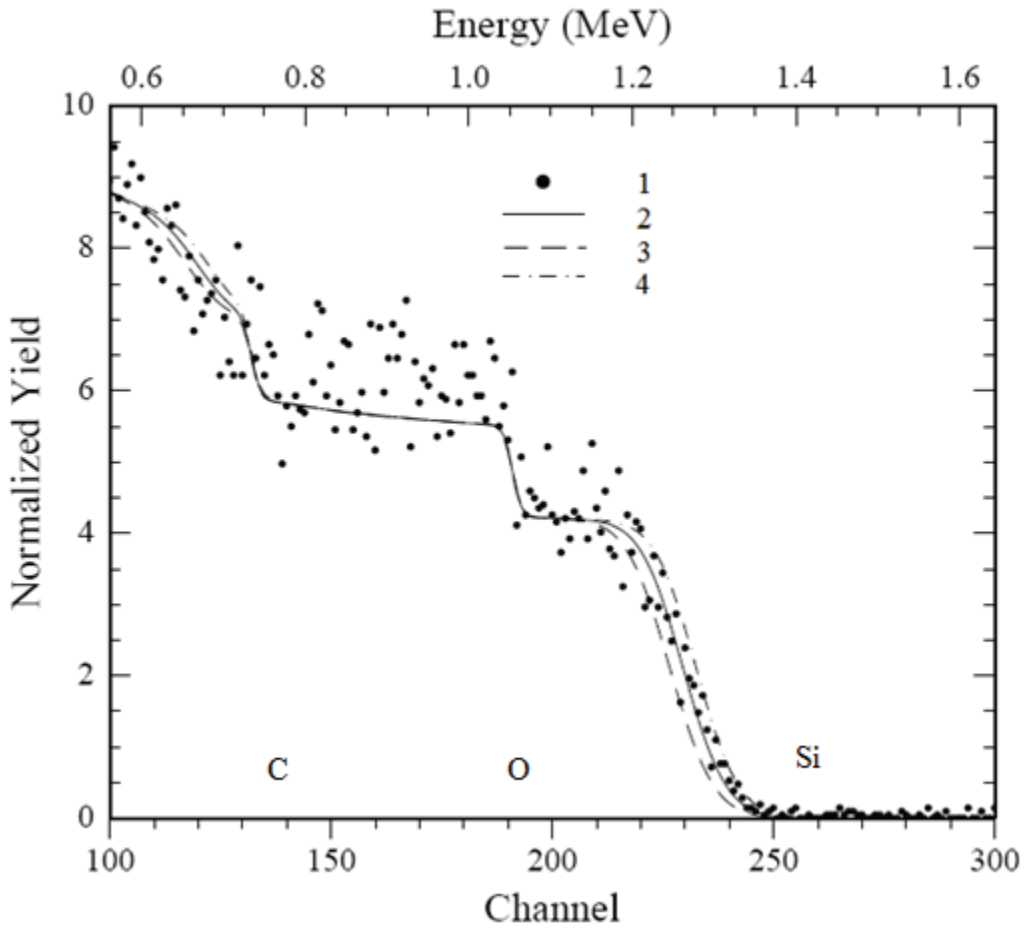

Figure 37.

This figure shows how RBS spectrum curve fitting with RUMP simulations are used to bracket a range from the areal density and obtained an average areal density with an error bar. Three simulations were run on the spectrum of the same HPMC cellulose film as in Figure 36. Symbol 1 (round dot) is the original spectrum, line 2 (solid line) is a simulation curve with 1.25×10^{19} atom/cm^2. The areal density obtained by line 3 is 1.30×10^{19} atom/cm^2. The areal density obtained from line 4 is 1.20×10^{19} atom/cm^2.

The hydrogen to oxygen and carbon ratio was also determined to be $N_C : N_O : N_H = 1.60 : 1.00 : 2.90$, using for the simulations with N_H incremented in

steps of 0.05, which can be compared to the HPMC cellulose ($C_{32}H_{60}O_{19}$) stoichiometric ratio of $32:19:60 \approx 1.68:1.00:3.16$. Thus, the combined method of using O and C resonances energies for RBS to detect C and O using the spectrum self calibration measurements with the underlying Si signal, and the 2.8 MeV He^{++} ERD of hydrogen calibration sample yields a hydrogen stoichiometry with a relative error of 8%.

Since the stoichiometry for hydrogen is derived from areal density measurements rather than surface peak signal height, this range of error matches the expected uncertainty from energy straggling.

4.6.2.3 Areal Density and Stoichiometry Determination of PDMS silicone

The PDMS silicone polymer substrate was also analyzed by 2.8 MeV He^{++} for ERD of hydrogen by fitting the ERD spectrum with a RUMP simulation and is shown in Figure 38. The hydrogen to oxygen and carbon ratio was also determined to be $N_{Si}:N_O:N_C:N_H = 1.00:0.85:1.80:3.50$ with N_H in steps of 0.05, as compared to the HPMC stoichiometric ratio of $N_{Si}:N_O:N_C:N_H = 1:1:2:6$.

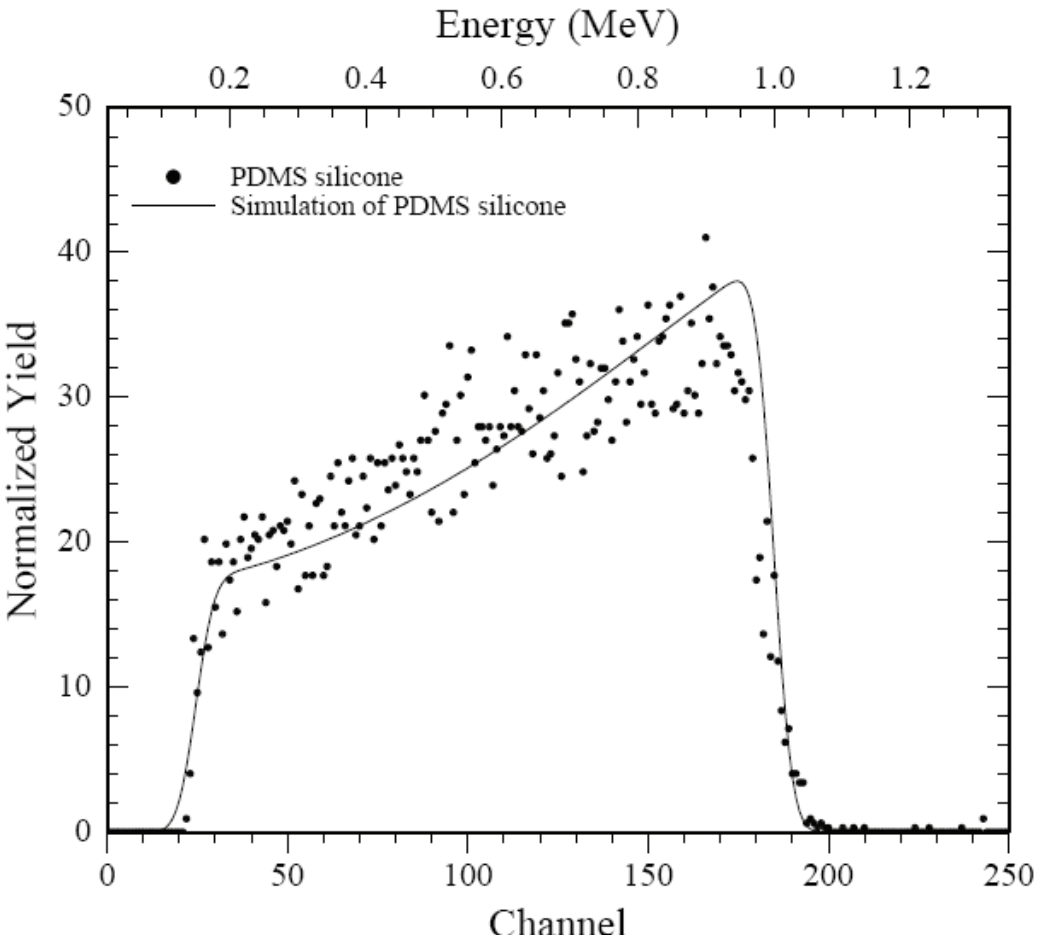

Figure 38.

2.8 MeV He^{++} ERD spectrum at 75° to the sample normal of the PDMS silicone substrate, with the hydrogen signal fitted with RUMP simulation to extract the areal density via calibration with a standard.

4.7 Areal Densities of Si, O, C, and H on Si(100)

4.7.1 Experimental Design

In this work, the C, O, and surface unregistered Si areal densities will be determined via channeling and rotating random in the <100> direction with respect to the Si(100) wafer. 4.265 MeV $^{12}C(\alpha, \alpha)^{12}C$ and 3.045 MeV $^{16}O(\alpha, \alpha)^{16}O$ are used to enhance the carbon and oxygen scattering cross sections. Si

surface peak is taken at 2 MeV via channeling and rotating random. Figure 39 shows an example of the 4.265 MeV $^{12}C(\alpha, \alpha)^{12}C$ with both channeling in the <100> and rotating random spectra overlaid on top of each other. Effectively, channeling reduces the background noise, while nuclear resonance enhanced the scattering cross section.

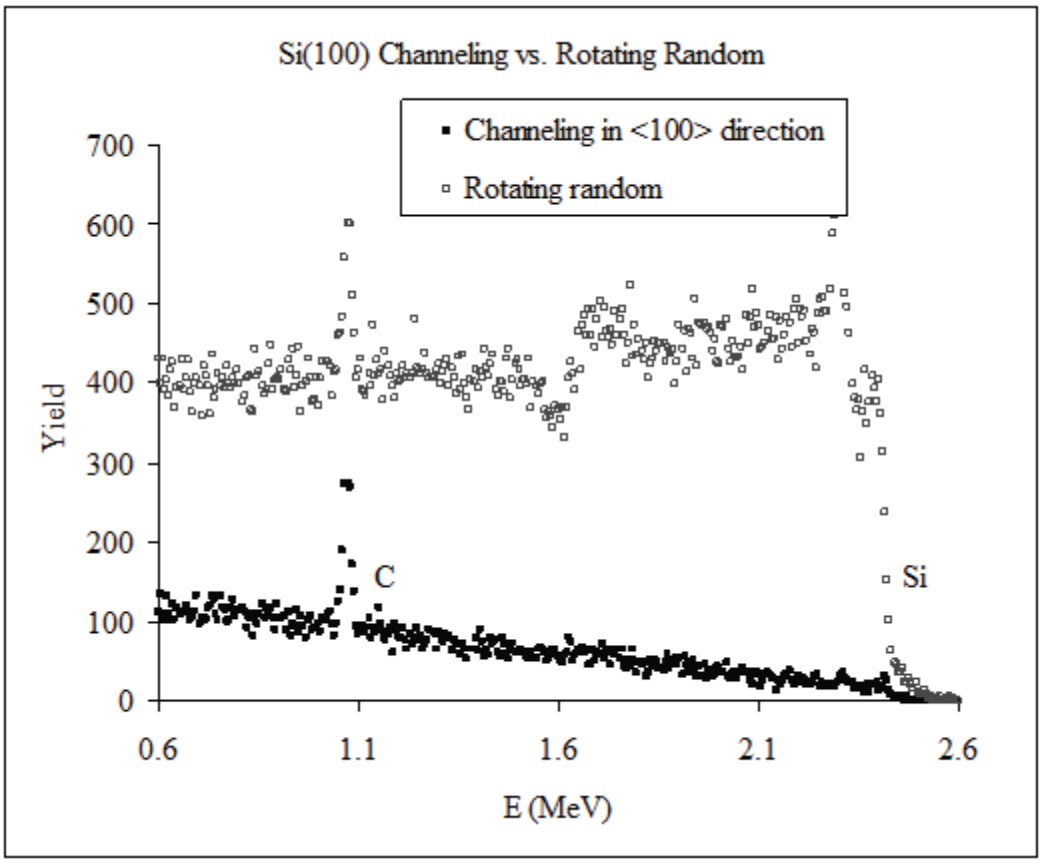

Figure 39.

Si(100) channeling versus rotating random in <100> direction and 4.265 MeV $^{12}C(\alpha, \alpha)^{12}C$. With both channeling in the <100> and rotating random spectra overlaid on top of each other. Effectively, channeling reduces the background noise, while nuclear resonance enhanced the scattering cross section.

4.7.2 Data Analysis via Channeling and Nuclear Resonance Scattering

The Si signal height is obtained via rotating random spectrum from the Si leading edge, similar example was discussed in Figure 27 earlier.

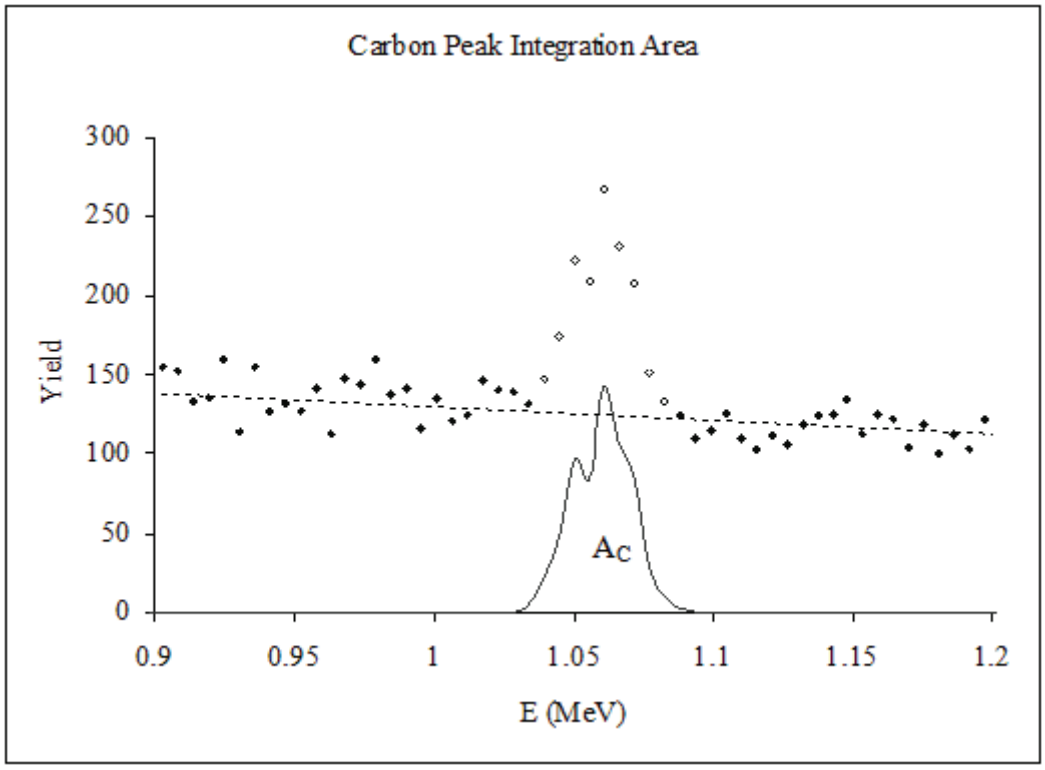

Figure 40.

Carbon resonance peak area extraction via channeling is demonstrate using Si(100) wafer channeling in the <100> direction at 4.265 MeV $^{12}C(\alpha, \alpha)^{12}C$. Surface peak integration area is obtained by area under the peak, subtracting the background noise. The area is outlined by the solid line. Note that channeling is preferred, but not mandatory.

The carbon and oxygen signal integration area are obtained via linear regression of background and signal trapezoidal subtraction of the background as

shown in Figure 40. To determine the areal density of the Si surface peak, a triangle subtraction method is shown in Figure 41.

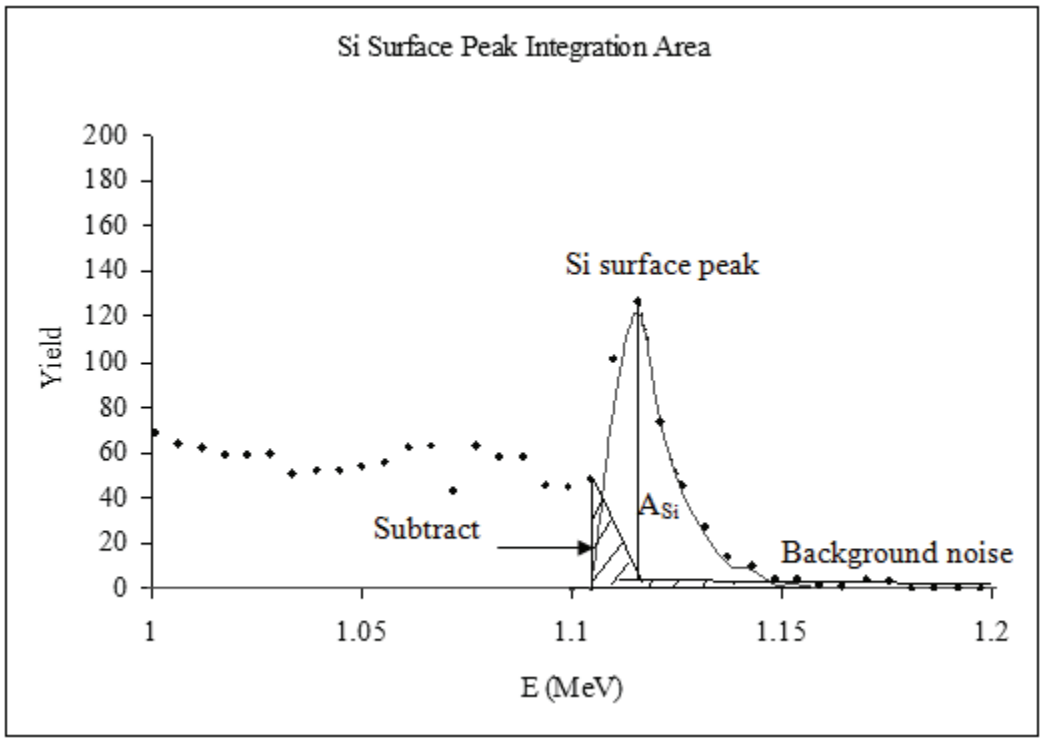

Figure 41.

Si surface peak area extraction via channeling is demonstrate using Si(100) wafer channeling in the <100> direction. Surface peak integration area is obtained by area under the peak, subtracting the background noise to the right, and subtracting the shaded triangle to the left. The area is outlined by the solid line.

The Si surface peak, oxygen, and carbon areal densities are shown in Table 3.

Table 3.

Areal densities of silicon, oxygen, carbon were obtained via channeling along the <100> axis at 2 MeV, 3.045 MeV, and 4.265 MeV (respectively), and calibrated using the rotating random silicon signal height.

Type of Si(100)	Si Surface Peak Areal Density (10^{15} atom/cm^2)	O Areal Density (10^{15} atom/cm^2)	C Areal Density (10^{15} atom/cm^2)	Prior He^{++} exposure ($\mu C/mm^2$)
As-Received-1 with IBMM	-	7.196	7.300	47.79
As-Received-2 with IBMM	16.366	4.659	2.190	39.97
Passivation-Sample-1 with IBMM	17.686	3.025	4.010	35.57
Anneal-Sample-1 with IBMM	15.426	4.300	2.434	57.74

4.7.3 Data Analysis via ERD

ERD to collect data to determine the hydrogen areal density was conducted at 2.8 MeV. RUMP was then used by combining the Si surface peak, oxygen, and carbon areal densities to identify the hydrogen areal density. The resultant RUMP simulation superimposed on the ERD spectra is shown in Figure 42.

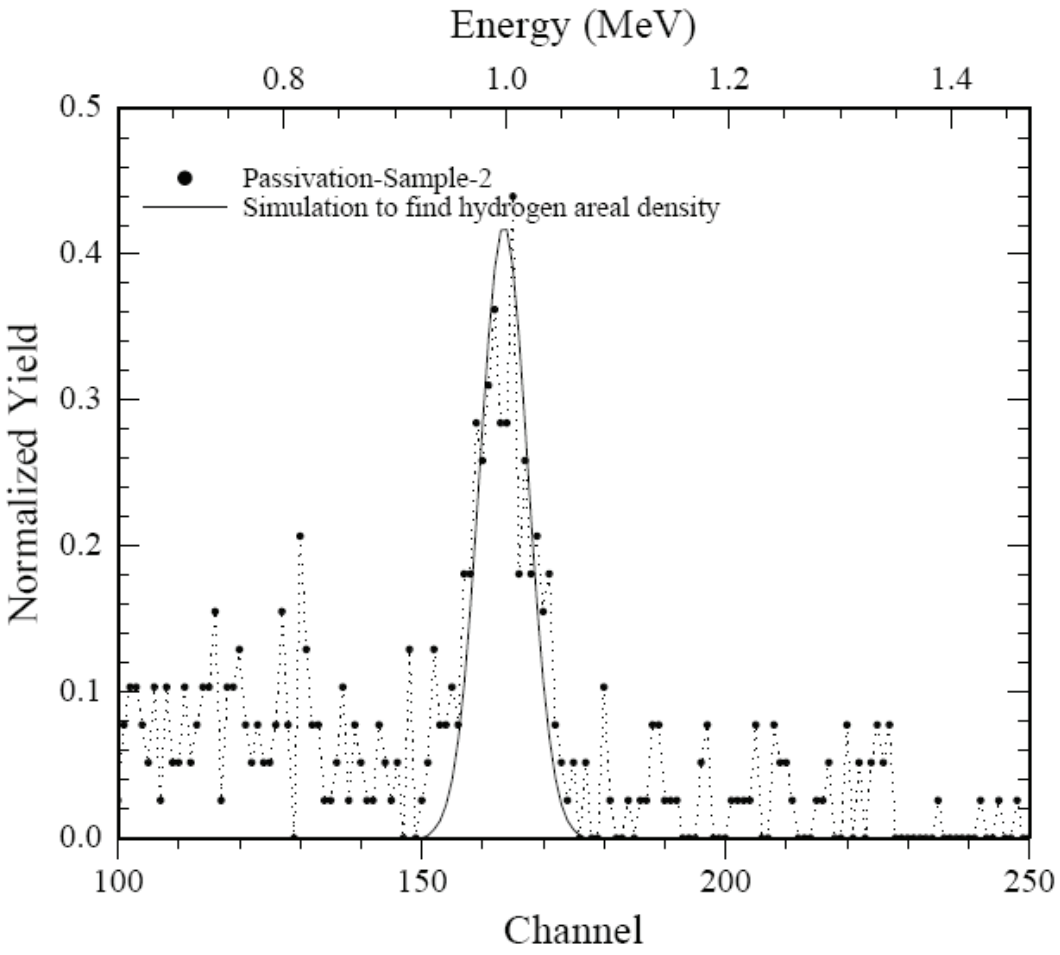

Figure 42.

He^{++} ERD of hydrogen at 2.8 MeV. Sample shown is Passivation-Sample-2, and surface hydrogen areal density of 4.4 (10^{15} atom/cm^2) is thus determined via RUMP fitting.

The hydrogen areal density results are shown in Table 4.

Table 4.

Hydrogen areal density was obtained using ERD at 2.8 MeV He^{++} analyzed utilizing RUMP.

Type of Si(100)	H Areal Density (10^{15} atom/cm^2)
As-Received-3	5.0
Passivation-Sample-2	4.4
Anneal-Sample-2	4.0

CHAPTER 5

PARTICLE INDUCED X-RAY EMISSION

5.1 Purpose

This third category of substrates is the high impact resistant polycarbonate used for most external visionwear applications such as glasses and visors. High performance visionwear typically have a thin, poorly characterized silica or glass coating on the polycarbonate. PIXE has perhaps one of the most versatile surface analyses, encompassing the broadest range of applications making use of IBA. From monitoring the behavior of thermally aged rubber [105], to the analysis of composites for restorative dentistry [106], and the investigation of undersea heavy metal and toxic element pollution in a Japanese bay [107], PIXE has of course been also been used to study the more mundane, such as quantitative elemental analysis of silicates and glass [108], and finally our own work on high impact resistance polycarbonates [109].

Differential PIXE was used on more than one occasion to build a relationship between the PIXE beam energy and the relative X-ray intensities particular metals [110, 111]. The variance of proton energy modifies the ratio uniquely depending if the sample is homogeneous or possesses a layered or depth profile structure [110, 111]. In a similar way, differential PIXE is used to depth profile the samples similar to the following references [112, 113]. In the present work, differential PIXE was further explored to work together with the ion beam energy loss concept to determine the areal density of the HPMC cellulose film on Si-based substrates, with the motivation being to induce condensation with

wetting rather than fogging on such surfaces via polymer adsorption on sport visionwear applications.

5.2 Background

When a high energy (MeV) ion beam bombards a sample, it causes inner shell ionization of the atoms by creating vacancies in their inner shell. Electrons from outer states then drop down to a more stable inner state, and thus an X-ray is emitted as a result of the ion induction. Since all electron energy levels from a certain element are fixed, X-ray emission can thus be used to identify the element by comparing the X-ray energy to the discrete energy level differences of an element [76, 114]. The amount of X-rays induced,

$$N_x = N_i \frac{N_0 \rho t}{A} \sigma_{\theta,E} d\Omega \eta_x \qquad (15)$$

with

N_i is the number of incident ions,

N_0 is the Avogadro's number,

ρ is the target density in g/cm^3,

t is the target thickness in cm,

A is the atomic weight of the element,

$\sigma_{\theta,E}$ is the cross section in cm^2 at given angle θ and ion energy E_i,

η_x is the detector efficiency at X-ray energy E_x, and

$d\Omega$ is the solid angle of the detector.

Alternatively, we now have $(\rho t)_Z = \frac{N_x}{N_i} F_{x,Z}$ for element Z, where $F_{x,Z}$ is a calibration constant for a given combination of atomic elements, X-ray transition, primary ion beam particle, detector characteristics, and PIXE geometry [76]. This means that for element Z in the sample, the areal density of the element has a direct relationship to $\frac{N_x}{N_i}$, which also implies that when $\frac{N_x}{N_i}$ is the same for a given element Z, the areal density of that element is also the same. We can now establish a relation between the ion beam energy and its relation to $\frac{N_x}{N_i}$ [109].

5.3 Theory and Method

In this work, differential PIXE is explored to examine whether the use of the ion beam's energy loss that the ion beam experiences as it travels through the HPMC cellulose adsorbate while inducing X-ray emission can be used to calculate the areal density of the HPMC cellulose.

First, the differential PIXE concept is used to correlate the incident ion beam energy E_0 vs. $\frac{N_x}{N_i}$ on the Si-based substrate without the HPMC cellulose film.

Next, after the HPMC cellulose film being applied, at high enough incident energy, the ion can penetrate through the cellulose adsorbate and enter into the Si-based substrate. As shown in Figure 43, due to the stopping factor of the film, ions experience an energy loss during the in-path of the HPMC cellulose film,

$$\Delta E_{in-path} = E_0 - E_s \approx \left[\frac{1}{|\cos\theta|} \varepsilon_E \right] N_{C_{32}H_{60}O_{19}} t \qquad (16)$$

where

E_0 is the incident ion energy before striking the HPMC cellulose,

E_s is the energy of ions at the substrate interface,

$N_{C_{32}H_{60}O_{19}} t$ is the areal density of the HPMC cellulose,

θ is the incoming angle of the ions to the sample normal,

ε_E is the energy loss cross section of HPMC cellulose at E.

Third, $\frac{N_x^{'}}{N_i}$ can be determined from the PIXE spectrum. When $N_x^{'} \approx N_x$, we can use the $\frac{N_x^{'}}{N_i}$ value to find E_s by the reverse lookup of relationship established using the Si-based substrate without HPMC cellulose film. Then use Equation (16) to estimate the HPMC cellulose areal density $N_{C_{32}H_{60}O_{19}} t \approx \frac{(E_0 - E_s)}{\frac{\varepsilon_{E,C_{32}H_{60}O_{19}}}{|\cos\theta|}}$.

Finally, the emission from within the substrate (on which the cellulose is adsorbed) can be a unique Si K X-ray (which includes both K_α and K_β X-rays) are used emission that can be compared to the uncoated region. The above X-ray notation follows the typical notation such as that found in [107, 115]. Even if the stoichiometry of the substrate and the thickness are unknown, the HPMC cellulose adsorbate has no Si, and hence the substrate and adsorbate can be distinguished.

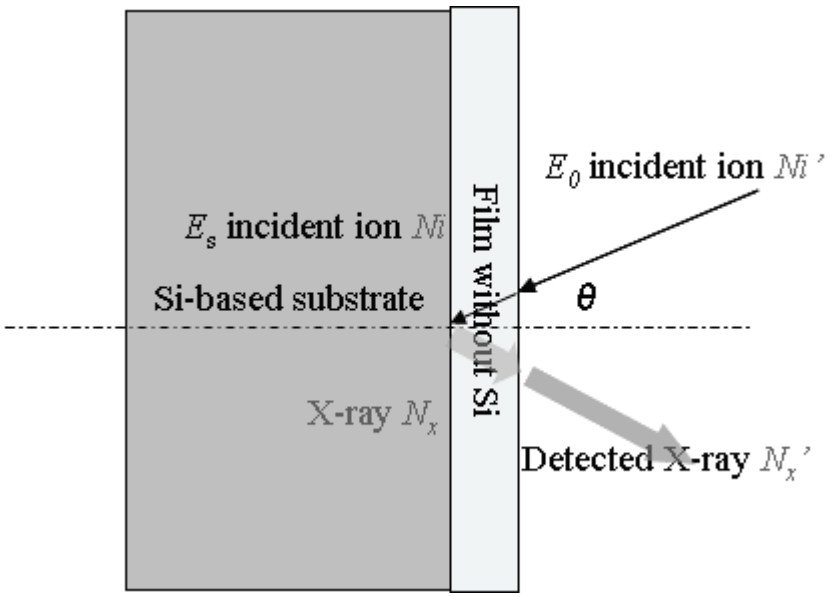

Figure 43.

Pictorial representation and geometry of Si-based substrate with applied HPMC cellulose film layer. E_0 is the energy of incident ion (N_i') just before striking the HPMC cellulose adsorbate, E_s is the energy of ions at the substrate interface (N_i), θ is the incoming angle of the ions to the sample normal, He^{++} induced X-ray (N_x) emitted out of the substrate interface, and then entered the detector (N_x').

5.4 Experimental Design

5.4.1 Initial Characterization of the Glass Coated Polycarbonate Visor

Initial characterization of the glass coated polycarbonate visor allows us to confirm whether or not it fits for differential PIXE analysis. The Oakley provided visors were analyzed using proton PIXE to confirm the Si signal. The proton incident energy was at 1.8 MeV, with an ion beam angle of incidence of 40° with respect to the surface normal and a detector angle that was 40° with respect to the sample normal in a vacuum of about 10^{-1} Torr without filter, and a beam current <

0.3 nA. The proton PIXE spectra in Figure 44 demonstrated that there is significant Si on both the convex and concave sides of the Oakley provided polycarbonate substrate.

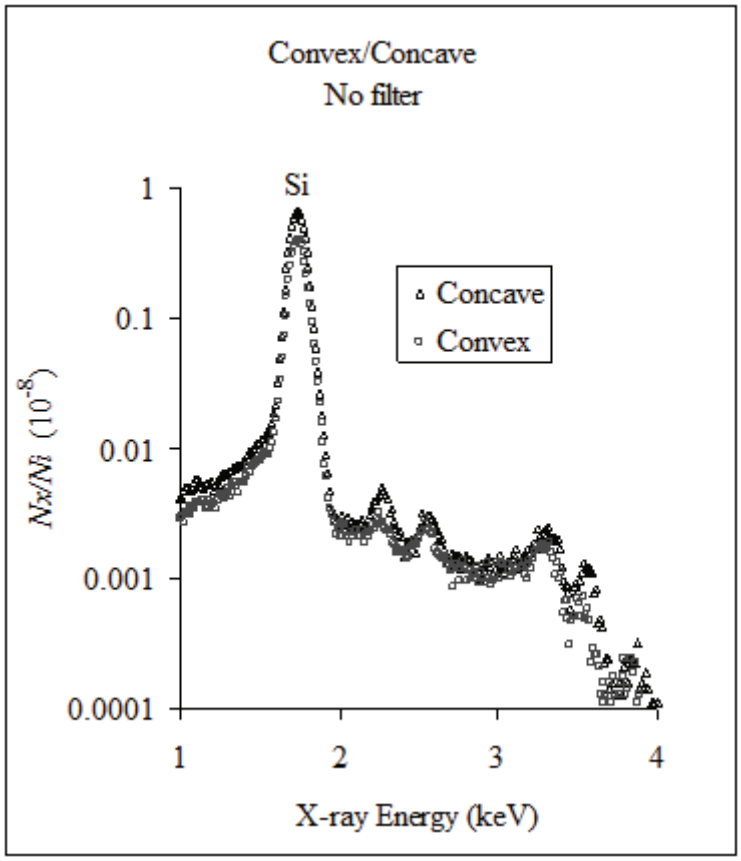

Figure 44.

Proton PIXE spectra with an incident energy of 1.88 MeV, an incident angle is 40°, and detector angle is 40° to the sample normal demonstrating that a significant silicon K X-ray signal can be detected in both area of the samples by using protons at this energy and geometry.

Comparison with RUMP simulation of RBS spectra taken on the same substrate and shown in Figure 45 and Figure 46, confirms the presence of Si, O,

and C with a stoichiometry of $SiO_2C_{2.5}$ and an areal density of 1.3×10^{19} atom/cm^2 for the silicon oxide coating on the polycarbonate.

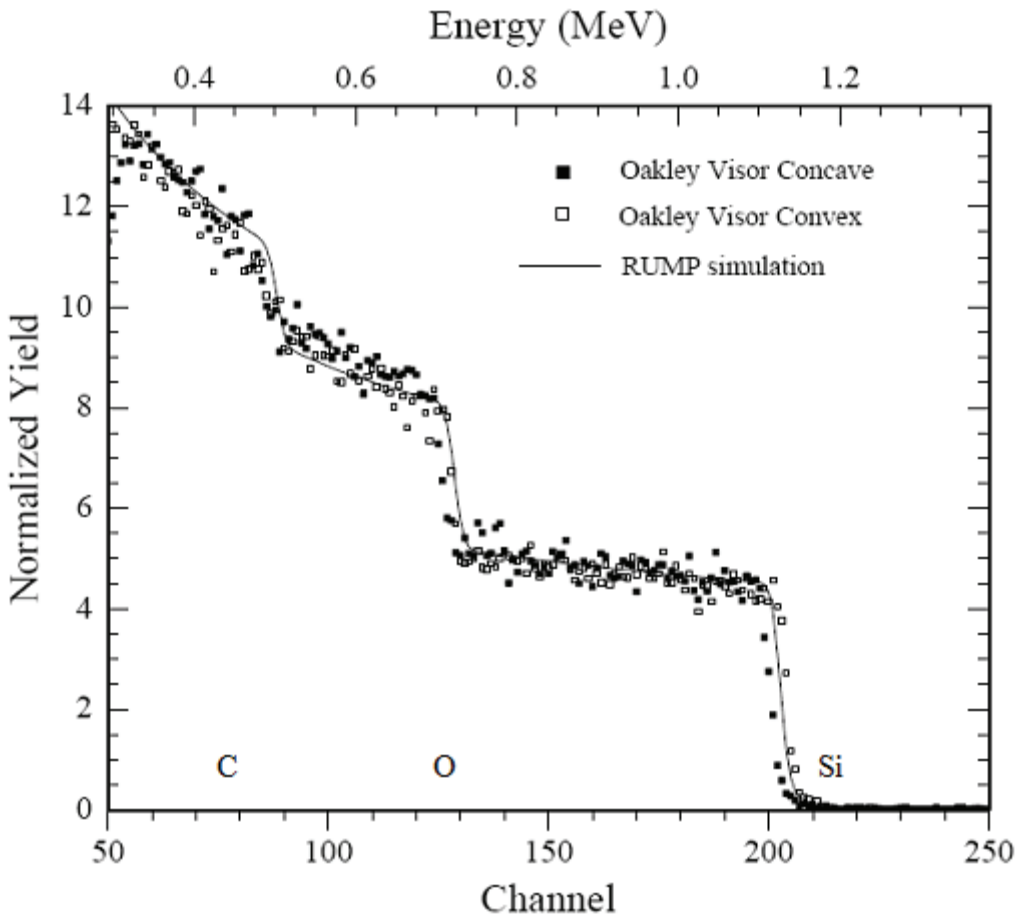

Figure 45.

He^{++} RBS spectra, taken with an incident energy is 2.0 MeV to verify the elements detected by PIXE and determine the stoichiometry via RUMP, which is $SiO_2C_{2.5}$. Note that the convex and concave sides of visor exhibit similar composition.

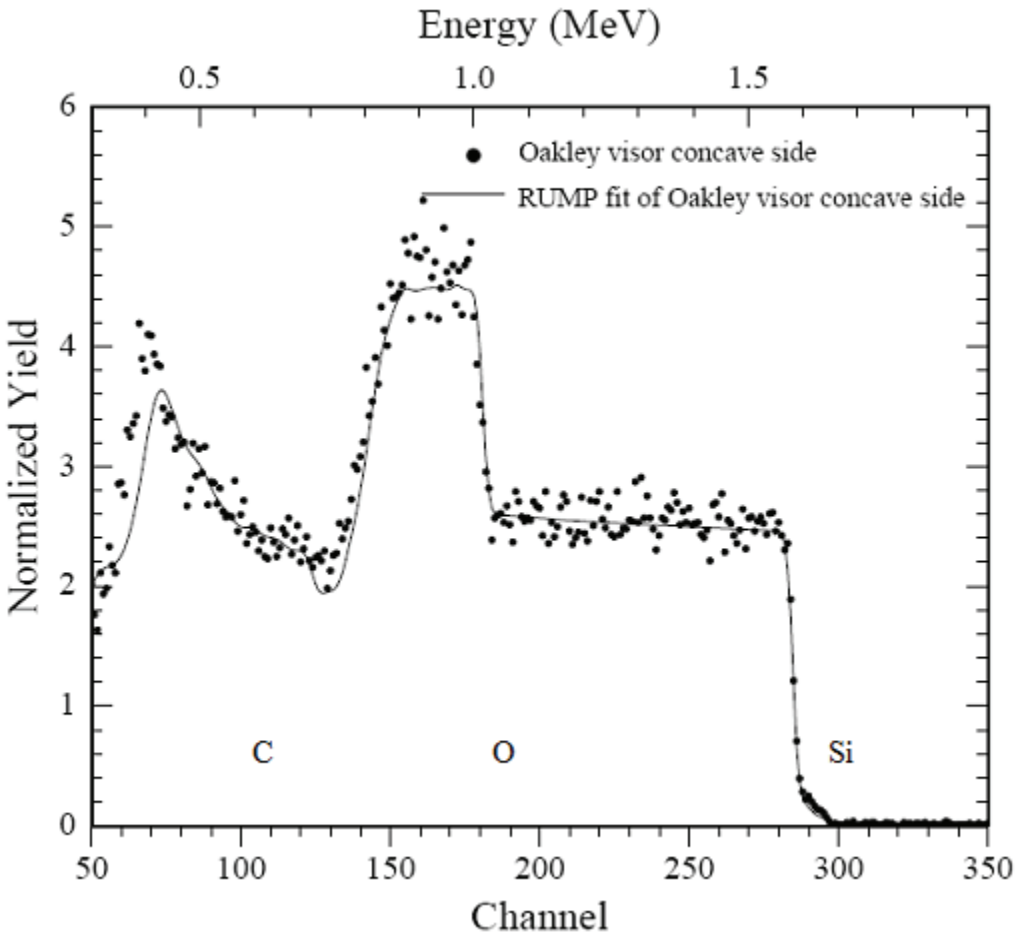

Figure 46.

He^{++} RBS spectrum, with an incident energy is 2.8 MeV, an ion beam incidence angle 8° to the normal and the detector 170° to the sample normal. The simulation fit via RUMP to the stoichiometric formula SiO_2C_3. This measurement was taken on the concave side of the polycarbonate substrates and yielded an areal density of 1.3×10^{19} atom/cm^2 for the film. Compare to Figure 45, visor composition is not uniform at all spots, especially carbon composition.

5.4.2 Ion Selection for Differential PIXE

He^{++} rather than H^+ was selected to enhance the energy loss within the HPMC cellulose adsorbate and thus the sensitivity of the measurement. He^{++} was

found to exhibit sufficient energy loss to allow for a measurable difference in Si K X-ray intensity of emission, while H^+ was found to be too penetrative to exhibit enough of an energy loss to lead to a significant decrease in intensity. The stopping factor of HPMC cellulose for He^{++} is approximately four times that of H^+.

Furthermore, $\frac{N_x^{'}}{N_i}$ also relied on the areal density (or thickness) of Si in the substrate to be differentiable at different incident ion energy. If the areal density or thickness) of the substrate is too thin, then $\frac{N_x^{'}}{N_i}$ is limited, and thus becomes none differentiable. From our initial analysis of the glass coated polycarbonate visors, the glass coating areal density is about 1.3×10^{19} atom/cm^2 which is about several μm. It is marginally enough for the He^{++}, but too thin for the H^+.

5.4.3 Accuracy and Systematic Error

The number of incident He^{++} lost to backscattering within the HPMC cellulose adsorbate is negligible ($\frac{N_i^{'} - N_i}{N_i^{'}} < 10^{-5}$), so we conclude $N_i^{'} \approx N_i$.

However, Si K X-ray attenuation is due to the HPMC cellulose film, as the emitted X-rays from the Si atom has to travel through the HPMC cellulose during its out-path. Approximately between 0.5% for a total areal density of 10^{18} atom/cm^2 to about 5.0% for a total areal density of 10^{19} atom/cm^2 of the HPMC cellulose adsorbate respectively, when the detector axis is positioned along at the sample normal. Thus, one should expect with the systematic error, yields of the actual areal density are lower than this measurement.

5.4.4 Geometry

The He^{++} beam impinges at an incident angle of 8° with respect to the sample normal and the detector angle is 37° from the sample normal for silica samples (see Figure 47(a)). Ion beam incidence normal to the surface minimizes beam travel in the samples and is suitable for thick film on thick substrate.

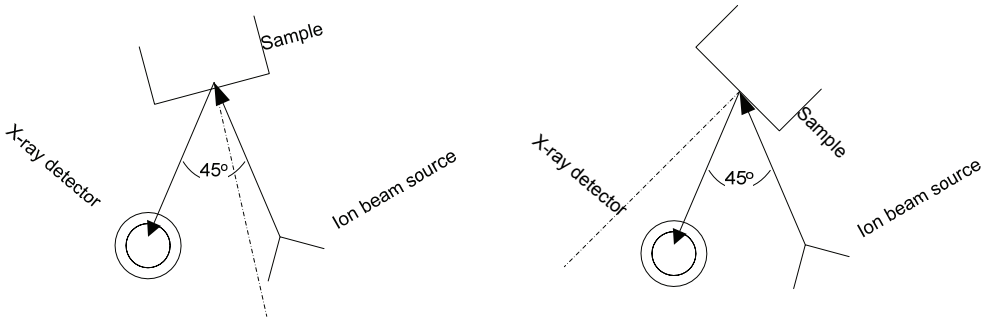

(a) (b)

Figure 47.

Angle between the X-ray detractor and the ion beam is fixed at 45°. The sample holder is rotatable. Setting (a) ion beam to the sample normal is 8°, while detector to the sample normal is 37°; (b) ion beam to the sample normal is 75°, while detector to the sample normal is 30°.

In the case of glass coated polycarbonates used for visionwear, the glass layer is much thinner than the silicon oxide and PDMS silicone substrates used for the IOL study and thus a more grazing incidence geometry had to be used and optimized. A detector angle of 30° and an incident angle of 75° to sample normal were found to yield sufficient Si K X-ray intensity from the thin silicon oxide coating on the polycarbonate samples (see Figure 47(b)). Large incident angle to

the sample normal maximizes the beam travel distance and is suitable for thin films on thin substrates.

5.4.5 Other Experimental Details

The He^{++} IBA is conducted in a vacuum of 10^{-7} Torr to 10^{-6} Torr without a mylar filter. Optimizing the beam current is critical to minimize detector dead time as well as pileup [116]. Detection of X-ray was most consistent when the beam current < 0.2 nA, therefore data collection was taken at 0.1 nA. Each spectrum was collected by using a charge of 0.5 μC. Sample charging due to the incident particles was again observed for both the silica wafer and visor samples, as found previously in RBS and nuclear resonance scattering. The same grounding method was thus used, by wrapping in an aluminum foil the sample was wrapped with a 4 mm to 10 mm diameter hole in the aluminum to allow for the beam to reach the surface. This surface grounding method minimized the charging effect and ensured the reproducibility of the spectra; it enabled consistent, repetitive data collection without energy shifts or erratic electrical discharge.

5.5 PIXE Data Analysis

Software GUPIX was used to calculate the area count of the silicon K X-ray (which included both K_α and K_β X-ray counts) [117]. Calibration of the spectra utilized the Soda-Lime Sheet Glass from the National Institute of Standards and Technology standard reference material 1831. This Soda-Lime Sheet Glass standard was selected as a calibration reference because of the similarity of components in the standard and our samples (i.e. the silicon in the

standard and the silicon in the Si-based samples). Thus, the calibration is accurate and direct for the range of emitted X-ray energy levels common to both the standard and the Si-based samples. Sample calibration fit is in Figure 48.

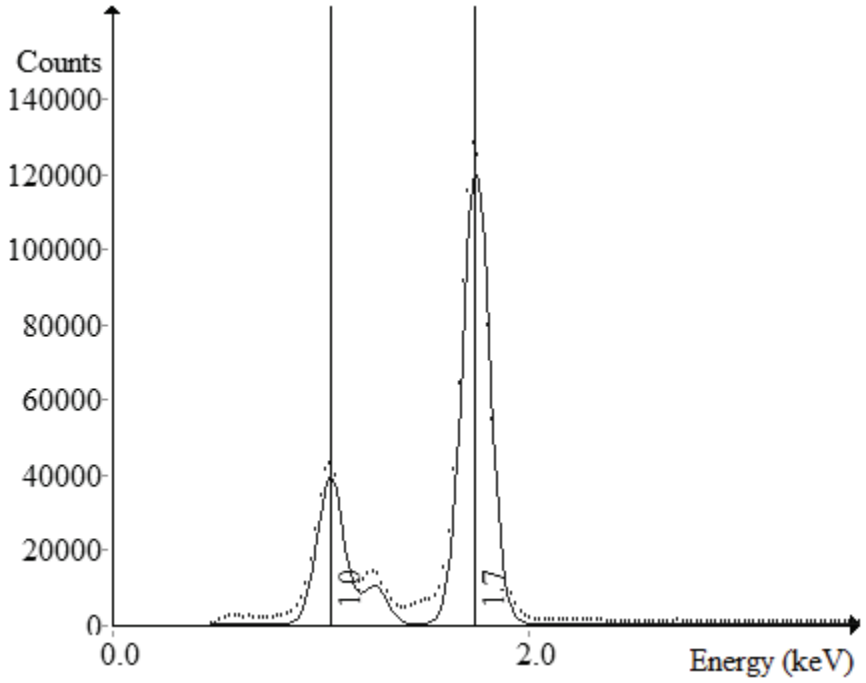

Figure 48.

Calibration of the spectra using the Soda-Lime Sheet Glass from the National Institute of Standards and Technology standard reference material 1831. Use Gaussian fit in this case.

After calibration, the PIXE spectrum can be fitted using the same parameters and the X-ray count is obtained from the integration of the peak. Residue is also verified to be random (see Figure 49).

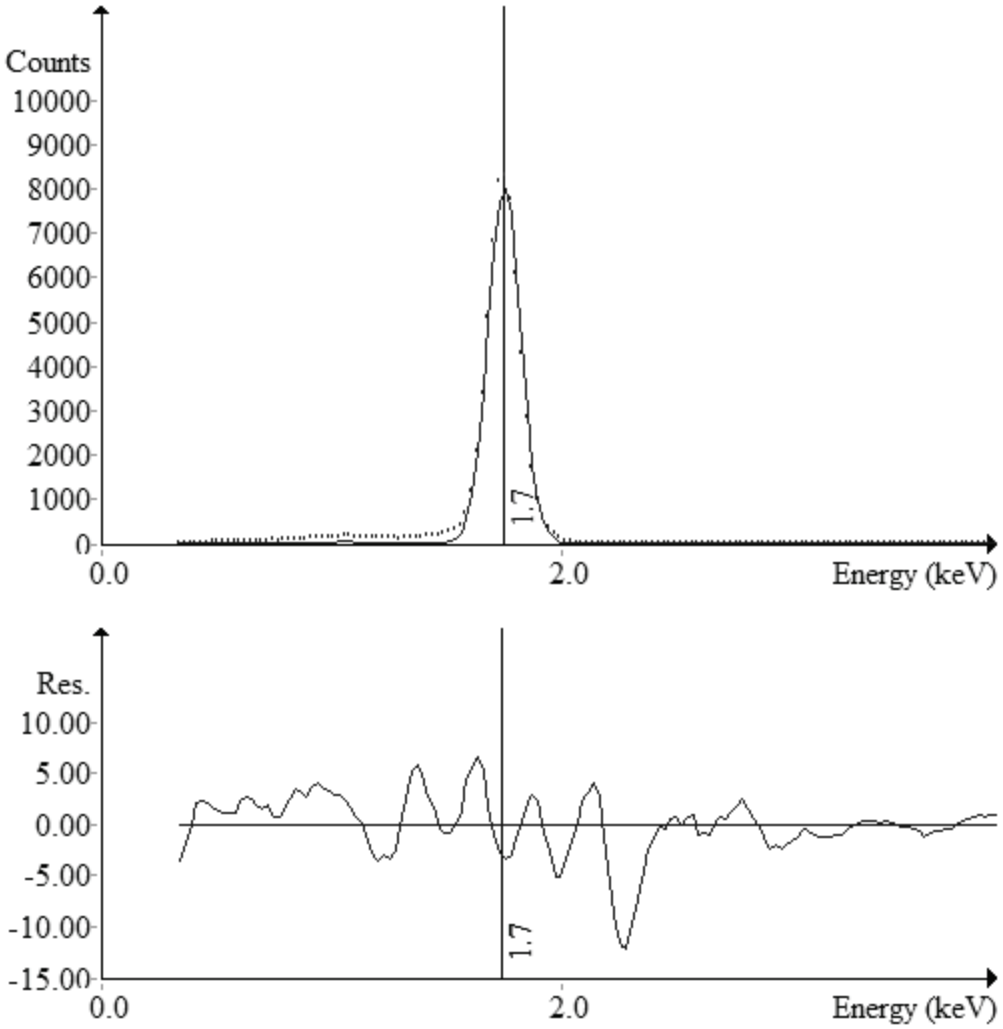

Figure 49.

PIXE spectrum is analyzed by GUPIX, Gaussian fit extracts the signal and the Si K X-ray count is obtained from the discrete integration of the area under the peak. The residual plot demonstrates good quality of the Gaussian fit with random oscillating residue.

The relationship between the incident He^{++} energy E and the ratio of detected silicon K X-ray count over the incident particle count $\frac{N_X}{N_i}$ is shown in

Figure 50, representing a silica substrate without HPMC cellulose film, and is used as the baseline for the relative yield graph.

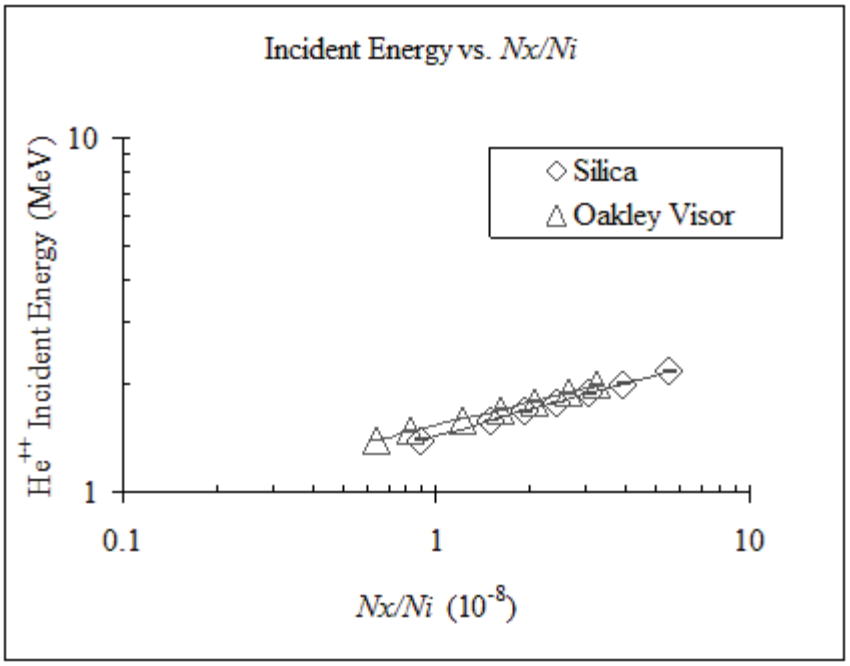

Figure 50.

Incident energy of the He^{++} plotted against the $\frac{N_x}{N_i}$ ratio. Note that the above data is based on silica and Oakley visor substrates without HPMC cellulose film by varying the incident energy.

The log-log regression modeling uncertainty is analyzed to serve as the basis to obtain the error of the areal density calculation utilizing the differential PIXE method. Areal density via the RBS method is obtained from RUMP simulation of the spectra. The uncertainty is analyzed from the roughness and determined by analyzing the Si leading edge of which indicated the roughness of the film is observed.

Uncertainty of the areal density measurement is obtained through error propagation of the regression modeling parameters. The areal density of the HPMC cellulose adsorbates is shown in Table 5.

Table 5.

HPMC cellulose gel concentration during the preparation of the dried film vs. areal density of the dried film determined using PIXE on silica wafer and glass coated polycarbonate visors provided by Oakley substrates.

Substrate Type	Gel Concentration (% wt.)	Film Areal Density (10^{15} atom/cm^2)
Silica Wafer	1.00% wt.	7500 ± 500
Silica Wafer	0.50% wt.	4270 ± 560
Silica Wafer	0.40% wt.	3040 ± 580
Silica Wafer	0.33% wt.	2100 ± 600
Glass Coating on Visor Concave Side	1.00% wt.	16560 ± 170
Glass Coating on Visor Concave Side	0.50% wt.	9430 ± 150
Glass Coating on Visor Concave Side	0.33% wt.	1430 ± 170
Glass Coating on Visor Concave Side	0.20% wt.	1640 ± 160

CHAPTER 6

CONTACT ANGLE ANALYSIS TO OBTAIN SURFACE FREE ENERGY

6.1 Approach

We have successfully shown that,

(a) over hydrated hydrophilic molecular adsorbates can modify water condensation as described in Chapter 3,

(b) areal density and composition of these molecular adsorbates on Si-based substrates can be characterized by IBA as shown in the previous Chapter 4 and 5, and

(c) we can qualitatively describe the wetting behavior on Si-based surfaces before and after adsorption of a hydrophilic molecular adsorbate.

As discussed in Chapter 2, in Figure 10, Figure 11, and Figure 14, the measurement of contact angles can detect changes in hydrophilic and hydrophobic behavior, as the above figures which compare contact angles of water between various hydrophobic and hydrophilic regions demonstrate. Changes in water affinity of a surface can only be detected and measured by observation and characterization of such contact angles. Hence, we needed to develop a consistent method to accurately measure contact angles on samples as varied as, 1" silica wafer pieces, 4" and 6" silicon wafers, 4 mm to 7 mm convex IOLs, and glass coated polycarbonate visor samples with both convex and concave surfaces.

This required the design of a proper apparatus and matching analysis software to consistently extract contact angles from various surface geometries

and the selection of appropriate parameters to succeed in quantitatively and reproducibly characterize contact angles. The next step is then to correlate these contact angles to surface composition and possibly the fundamental property of SFE if needed. One fact must be considered; both surface composition and topography modify water condensation pattern, as shown in Chapter 2, Figure 11 and Figure 14. Thus, the contact angle and water affinity observed in the present chapter are not complete without being correlated with

(a) the composition and areal densities obtained from IBA in Chapter 4 and 5, and

(b) the results from the next Chapter 7, which discusses characterization of the topography by Atomic Force Microscopy (AFM).

6.2 Combining the Young-Dupré Equation for SFE as a Function of Contact Angles with Van Oss theory

The SFE of a liquid and solid interface can be derived as function of the contact angle of the liquid on the surface and used to quantify water affinity via the Young Dupré equation combined with Van Oss theory. The Young Dupré equation states that the SFE of the solid and the liquid simply add up by factoring the contact angle in the contribution of the liquid SFE to the total interfacial energy.

$$\gamma_{SL} = \gamma_S + \gamma_L \cos\theta \qquad (17)$$

with

γ_L is the liquid's SFE,

γ_S is the solid's SFE,

γ_{SL} is the SFE at solid-liquid interface, and

θ is the contact angle made at the solid-liquid interface [118].

The contact angle modulates the contribution of the liquid SFE to the total energy as an inverse function of the contact angle via the cosine factor of that angle.

Recall the Van Oss theory in Chapter 2 in terms of Equation (1), each of the SFE components is expressed as the sum of:

(a) the LW component of SFE accounting for the apolar dispersion component, and

(b) the polar component of SFE from both positive electron donor (Lewis acid) and negative electron acceptor (Lewis base). This contribution is typically modeled by an asymmetry contribution, the square root of the product of the Lewis acid component and the Lewis base component.

Thus each of the three terms in the Young-Dupré equation can be replaced, so the modified Young-Dupré equation can be rewritten as

$$(1+\cos\theta)\gamma_L = 2\left(\sqrt{\gamma_S^{LW}\gamma_L^{LW}} + \sqrt{\gamma_S^{+}\gamma_L^{-}} + \sqrt{\gamma_S^{-}\gamma_L^{+}}\right) \qquad (18)$$

Large SFE components combine into a large total liquid and solid interface energy which results in the contact angle being small, and defines the surface as being hydrophilic, due to the strong intermolecular forces and charge interactions between the surface and water. If the value of the contact angle increases, the SFE contribution decreases as expected for a surface being hydrophobic. The intermolecular forces are weak and there are few charge interactions.

6.2.1 Determination of SFE Using Three Different Contact Angles from Three Different Liquids

The three identified components of the SFE of the liquid and solid interfaces from the Van Oss theory can be calculated by measuring the contact angles of three distinct types of liquids to the one solid surface to be characterized [66]. One can then calculate the total SFE through the following set of three equations with three unknowns,

$$\begin{pmatrix} \sqrt{\gamma_S^{LW}} \\ \sqrt{\gamma_S^{+}} \\ \sqrt{\gamma_S^{-}} \end{pmatrix} = \frac{1}{2} \cdot \begin{pmatrix} \sqrt{\gamma_{L1}^{LW}} & \sqrt{\gamma_{L1}^{-}} & \sqrt{\gamma_{L1}^{+}} \\ \sqrt{\gamma_{L2}^{LW}} & \sqrt{\gamma_{L2}^{-}} & \sqrt{\gamma_{L2}^{+}} \\ \sqrt{\gamma_{L3}^{LW}} & \sqrt{\gamma_{L3}^{-}} & \sqrt{\gamma_{L3}^{+}} \end{pmatrix}^{-1} \cdot \begin{pmatrix} (1+\cos\theta_{L1})\gamma_{L1} \\ (1+\cos\theta_{L2})\gamma_{L2} \\ (1+\cos\theta_{L3})\gamma_{L3} \end{pmatrix} \quad (19)$$

with

subscript S representing solid,

subscripts of $L1, L2, L3$ represent the three types of liquid respectively,

θ is the contact angle made at the liquid and solid interface,

γ is the SFE,

γ^{+} is the Lewis acid component of the SFE,

γ^{-} is the Lewis base component of the SFE, and

γ^{LW} is the LW component of the SFE.

This approach to analyzing SFE will be used to quantify the water affinity in this dissertation for three different Si-based surfaces: the PDMS silicone IOLs, and the Si(100) and quartz silica wafers before and after processing with the Herbots-Atluri clean and before applying a hydrophilic adsorbate.

The extraction of energies from the matrix derived from Equation (19) above was conducted by using the calculation software tool SurfTen 4.3 [119, 120] where the calculated uncertainty is computed via error propagation of the inverse of the matrix.

Since SFE measurements on unmodified quartz silica and PDMS silicone surfaces have been conducted and reported in the literature [66], the measurements obtained on the fused quartz silica and medical grade PDMS silicone samples used in the present work can be compared to these results before water affinity modification.

6.3 Selection of Liquids for Use in Determining SFE

Henceforth the three distinct liquids selected for these experiments are three of the liquids selected by reference [66] to facilitate the comparison. Selection of each respective liquid was determined using three distinct requirements.

The first and most critical requirement is to determine which SFE components each of the liquids possessed; the LW SFE component, the Lewis acid SFE component, and Lewis base SFE component. As these three SFE components are the three variables from Equation (19) above, the ideal respective liquid will be heavily weighted in one SFE component, and have minimal or zero weight in the other two SFE components. Thus, each liquid will ideally possess a large LW SFE component, large Lewis acid SFE component, or large Lewis base SFE component, respectively and exclusively. The second requirement, self imposed, was to select three liquids which have been used by other groups in

measuring the SFE components. This allows direct comparison of the liquids' SFE components and allows the starting point for the liquid selection process. As noted above, the three liquids were selected from an extensive list given in reference [66].

The third and final requirement was the respective liquid's toxicity and availability. With a constraint of working with these liquids in a laminar flow area, liquid toxicity needed to be minimized. The liquids had to be readily available with applicable material safety data sheets available and on hand.

The three liquids selected were DI water (18 MΩ cm), glycerin, and α-bromonaphthalene. Their respective SFE components are summarized in Table 6. below. α-bromonaphthalene meets the first requirement: both its Lewis acid and Lewis base SFE components are zero, while its LW SFE component is significant in magnitude at 44.4 mJ/m^2 [66]. Glycerin possesses significant electronegativity, and its Lewis base SFE component, equal to 57.4 mJ/m^2, dominates its very weak Lewis acid SFE component, equal to 3.92 mJ/m^2, and thus glycerin is selected because of its strong, electronegative polar nature. Finally, to fulfill the requirement of a liquid in possession of a significant Lewis acid SFE component, we turn to DI water (18 MΩ cm), whose respective SFE component is 25.5 mJ/m^2. Most liquids have a very minimal Lewis acid component, with an exception being sodium deoxycholate, with a Lewis acid component of 10.48 mJ/m^2. However, sodium deoxycholate's Lewis base component still dominates at 38.72 mJ/m^2, and hence DI water was selected as the liquid with the Lewis acid SFE component [121].

Table 6.

SFE of DI water, glycerin, and α-bromonaphthalene test liquids [121].

Test Liquid Type	Total SFE γ^{Total} (mJ/m^2)	LW Component of SFE γ^{LW} (mJ/m^2)	Base Component of SFE γ^{-} (mJ/m^2)	Acid Component of SFE γ^{+} (mJ/m^2)
DI Water	72.8	21.8	25.5	25.5
Glycerin	64	34	57.4	3.92
α-Bromonaphthalene	44.4	44.4	0	0

6.4 Experimental Design

6.4.1 Contact Angle Measurement Equipment Setup

Figure 51(a), (b), and (c) show the design and the picture of one of the platforms built in this work to conduct the data collection for the contact angle measurement experiment. Several characteristics of the setup have to be achieved.

First, the working environment, along with all surfaces in and around the contact angle measurement equipment setup ("the setup") must be as contaminant free and as inert as possible. Thus, all materials used are cleanroom grade, and are chemically stable on contact with all three liquids involved (DI water, glycerin, α-bromonaphthalene) used for the experiments. Only stainless steel, polypropylene, nylon, glass and Teflon are used to construct and manipulate the setup. All experiments are conducted in a class 10 laminar flow hood to avoid dust and particulate contamination of the liquids and surfaces measured.

Second, a stable, level platform must be instituted such that the sample surfaces can be systematically reproducibly aligned each time a set of contact angle measurements is collected. Note that subsequently the large uncertainty with respect to alignment of the non-planar surfaces such as IOLs will be addressed by using the Sessile drop method described below.

Third, the setup requires a fixed geometry with a consistent light source, a digital camera with its distance to the samples fixed, and a built in scale (implemented as a ruler in the setup) to be imaged with the droplets on the surface to maintain reproducible image capture conditions when collecting the contact angle data.

Fourth, but just as critical as the requirements above, is creating and maintaining the process and procedure for dispensing the liquid droplets as reproducibly as possible an optimized volume of the respective liquid on the target surface. This step required verifying a syringe's volume dispersal using an automated pipette liquid dispenser. The syringe was required due to the viscous nature of one of the three liquids, glycerin.

(a) (b)

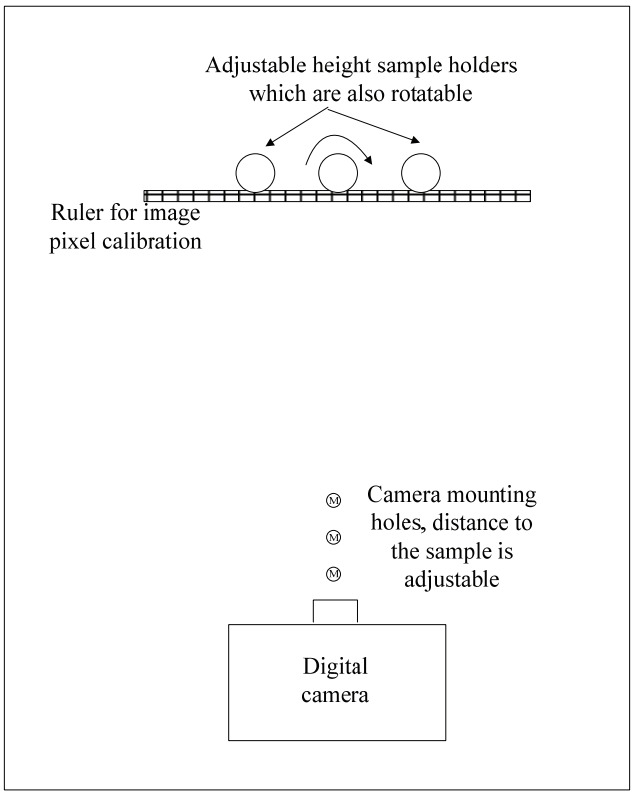

(c)

Figure 51.

Contact angle measurement equipment setup, which shows (a) platform made of polypropylene, which supports a digital camera, ruler used as a scale, and with back illumination from the lamp, (b) sample holder, (c) identifies, from a top down profile, the particular components of the contact angle measurement setup.

6.4.2 Using the Sessile Drop Method for Determining the Contact Angle

Next, the measurement method for the contact angle has to be selected for accuracy to minimize the uncertainty in how level the surface is, since the surface curvature of the IOL samples is significant (but unavoidable) and can vary with the dioptry (optical correction) and diameter (4 mm to 7 mm) of a given IOL.

The Sessile drop method [122] is used to conduct the contact angle measurement data collection (see Figure 52). The Sessile drop method was chosen over other static methods and dynamic methods because it is suitable for the small size and curvature of our PDMS silicone IOL samples. In this work, the contact angle is measured using computer fitting techniques on the digital images. Both droplet size and contact angle are computed via computer processing assuming equation for the droplet is $\frac{x^2}{a^2}+\frac{y^2}{b^2}=1$ with a and b being the semi major and minor axis respectively.

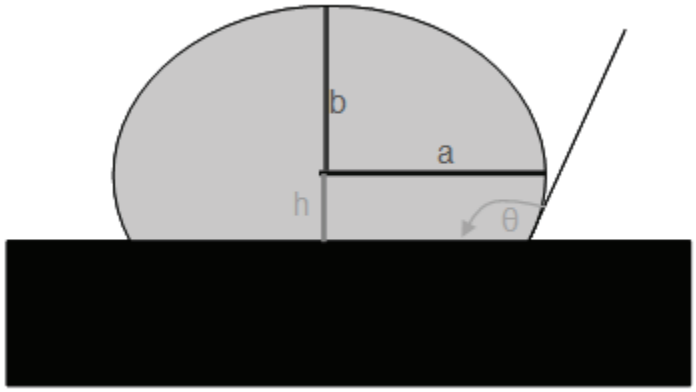

(a)

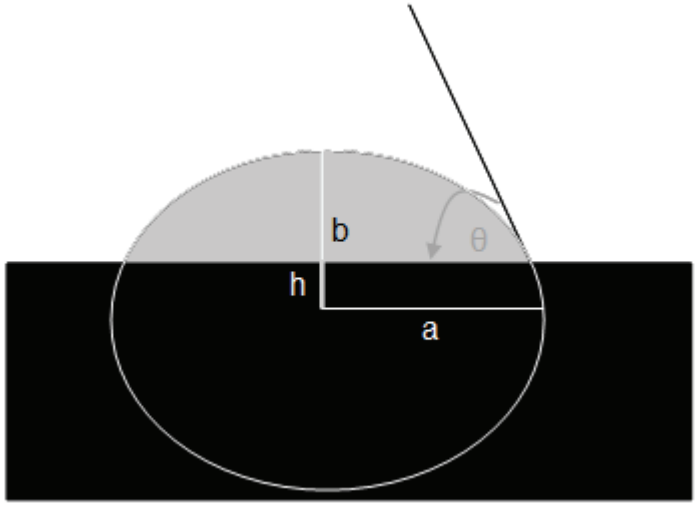

(b)

Figure 52.

Pictorial representation and geometry of Si-based substrate with a water droplet indicating (a) a hydrophobic surface, and (b) a hydrophilic surface.

The contact angle and droplet volume can be determined by the equations and analysis below,

$$\theta = \begin{cases} \tan^{-1}\left(\frac{b}{a}\sqrt{\frac{b^2}{h^2}-1}\right) \text{ when } 0 < h \le b \\ \frac{\pi}{2} \text{ when h = 0} \\ \pi - \tan^{-1}\left(\frac{b}{a}\sqrt{\frac{b^2}{h^2}-1}\right) \text{ when } -b \le h < 0 \end{cases} \quad (20)$$

$$V_{droplet} = \int_h^b \pi\left(1-\frac{y^2}{b^2}\right)\cdot a^2 dy = \pi a^2\left[\left(b-h\right)-\frac{b^3-h^3}{3b^2}\right] \quad (21)$$

where

a is the semi major axis,

b is the semi minor axis, and

h is the vertical offset coordinate.

A Java applet was developed during this work to do the calculation of θ and $V_{droplet}$.

Choosing the appropriate droplet size is critical for the ellipsoidal fit. According to the Young-Laplace equation,

$$\Delta P = \gamma \nabla \cdot \hat{n} \quad (22)$$

with

ΔP is the pressure difference at the liquid air interface,

γ is the SFE of the liquid, and

$\hat{n}$ is the unit of normalization vector to the liquid air interface.

If the force due to gravity is ignored, the droplet's shape becomes a sphere. However, the droplet is influenced by the liquid gravitational pressure of ρgh where ρ is the density of the liquid, g is the gravitational acceleration, h is the

depth of liquid; see Figure 53. When $\rho gh << \Delta P$, the droplet can be approximated to an ellipsoid and can also account for the effect that the surface is not perfectly flat. Therefore the liquid droplets chosen ranges in sizes from 0.2 μL to 10.0 μL and were delivered using a syringe with a 23 gauge cannula.

Droplet volume verification was done using the electronic pipette. Originally the electronic pipette was to be used to deliver the droplets of all three liquids (DI water, α-bromonaphthalene, and glycerin). However, there were technical difficulties encountered when delivering the specific droplet volumes. First, the electronic pipette had the propensity to "spit out" low volume droplets (e g. 2 μL), complicating the droplet application process. Also, the electronic pipette did not function properly in administering the highly viscous glycerin, as the glycerin droplets would bead up at the tip of the pipette due its viscosity and interfere with the application of the droplets. Thus, a syringe with a 23 gauge cannula was used to administer the droplets onto the sample surfaces. The size and precision of the cannula tip afforded a much more controlled application method for the respective droplets onto the samples.

However, the electronic pipette was used to validate the software developed to measure the volume of the droplets. The pipette was used to deliver 2 μL sized droplets, and then the method described below along with the uniquely developed software was used to measure the volume of the droplets and compared against the specified volume of the metered droplets. The accuracy in which the software and method calculated the volume was within 98% of the specified volume of the metered droplets; an error of less than 2%.

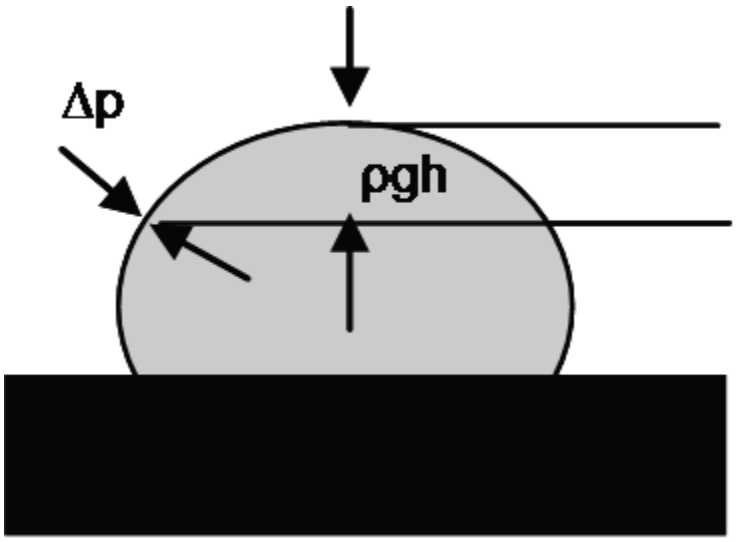

Figure 53.

Droplet pressure and curvature.

The surface may not be perfectly flat as shown in Figure 54 and Figure 55. Concave and convex surfaces using the ellipsoidal fit will need to account for the curvature of the solid-liquid interface. A cone approximation can be applied using the angle and volume correction to Equation (17) and (18), as shown below,

$$\Delta\theta = \tan^{-1}\left(\frac{i-h}{\sqrt{\left(1-\frac{h^2}{b^2}\right)a^2}}\right) \tag{23}$$

$$\Delta V = \frac{\pi}{3}\left(1-\frac{h^2}{b^2}\right)a^2 \cdot |i-h| \tag{24}$$

where

i is the vertical coordinate of the cone vertex.

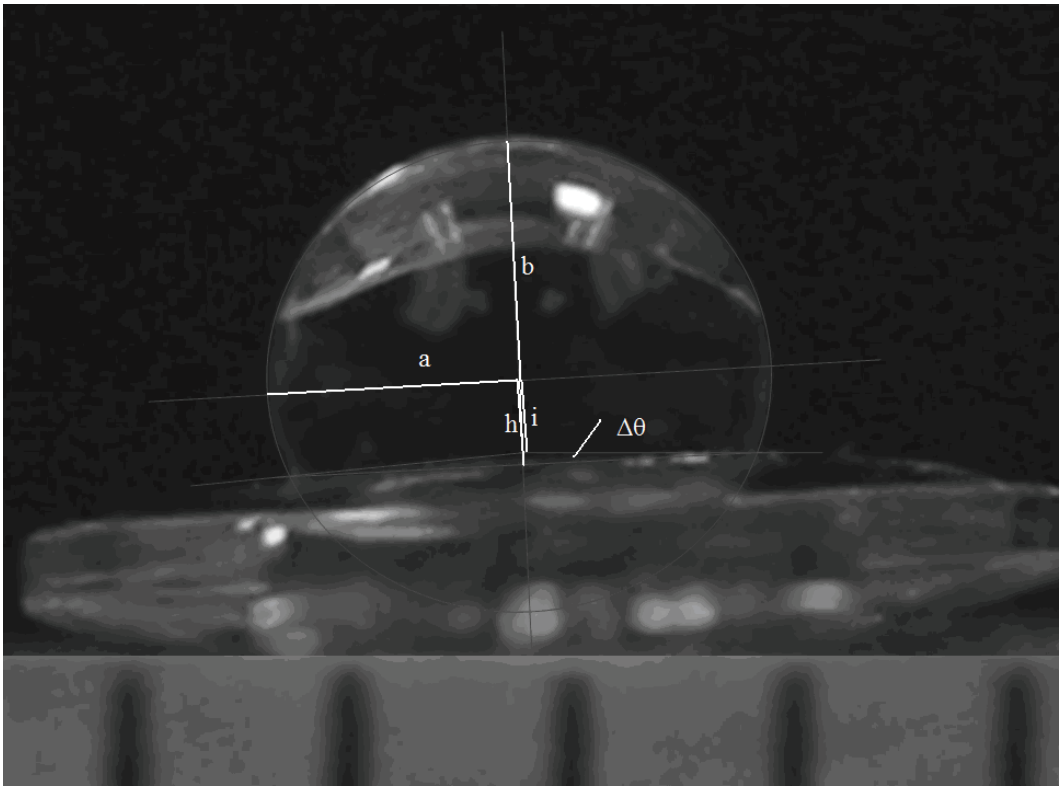

Figure 54.

Sessile drop on a convex hydrophobic surface of PDMS silicone IOL.

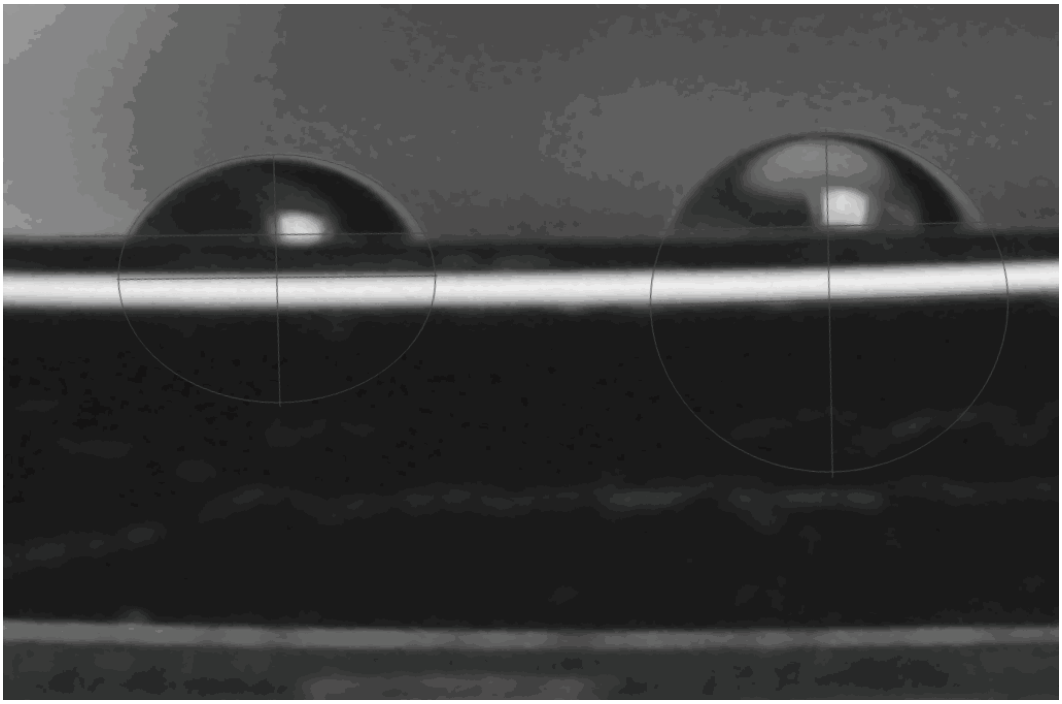

Figure 55.

Sessile drop on the concave hydrophilic surface of an visionwear sample.

In addition, the Sessile drop advances due to gravity on convex surfaces and recedes due to gravity on concave surfaces. As a result, it is noted that the droplet size for hydrophobic surfaces impacts the contact angle measurement to be larger, while the droplet size has an opposite effect for hydrophilic surfaces. As shown in Figure 56, hydrophobic PDMS silicone surface contact angle vs. droplet volume is found to have a linear correlation, with a linear regression p-value < 0.05, while the hydrophilic quartz silica surface has less correlation between the contact angle and droplet volume. Therefore, for hydrophobic surfaces, the contact angle extrapolated to zero droplet volume is recorded with uncertainty propagated from the linear regression while for hydrophilic surfaces, an average

value of the contact angles is determine, with the error of the mean uncertainty calculated.

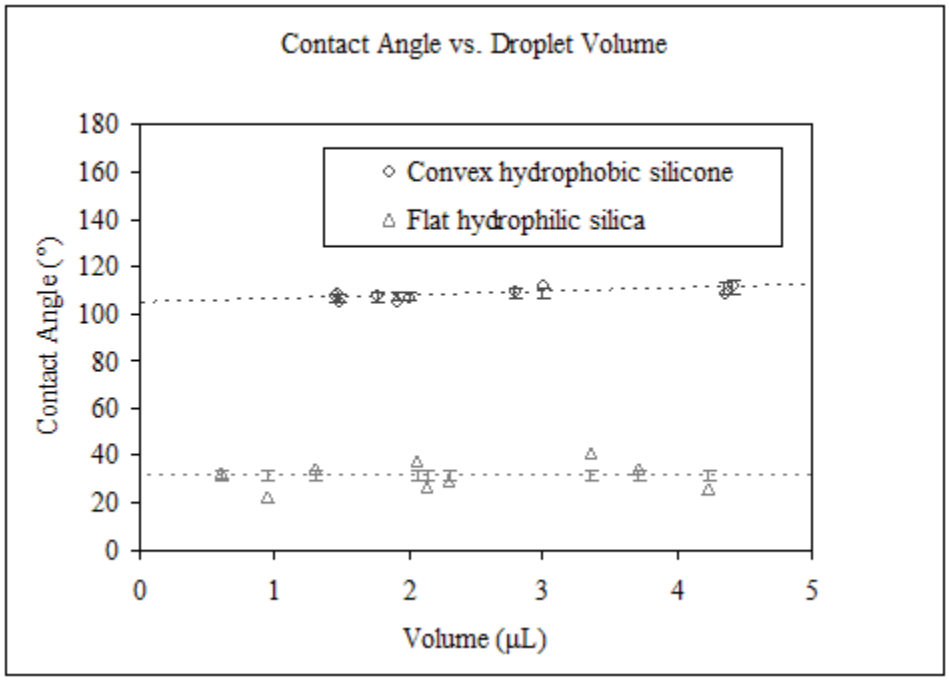

Figure 56.

Contact angle vs. droplet volume for PDMS silicone and quartz silica. Contact angles were measured and plotted versus volume to determine the relationship which the volume of the drop had on influencing the contact angle. Contact angle at zero angle was the extrapolation to the y axis.

The contact angles between water and surfaces including PDMS silicone and silica are measured using the above method. The consistency of the values obtained by our measurements are verified by comparing to existing publications [14, 15] and shown in Table 7.

Table 7.

Comparisons of water contact angles from existing publications and this work for PDMS silicone and silica wafer surfaces.

Surface Material	Contact Angle with Water from Publications $\theta°$	Contact Angle with Water from This Work $\theta°$
PDMS Silicone	107.2 [123]	104.7 ± 1.4
Silica Wafer	30.77[1]	32.2 ± 1.9

[1] Determined using Equation (18) and SFE from [20]

Table 8 and Table 9 show the measurements of contact angles and the determination of SFE of surfaces where no data has been reported in the literature. Detail sample description and analysis of these results are in later Chapter 8.

Table 8.

Contact angle measurements with three different test liquids, water, glycerin, and α-bromonaphthalene.

Surface Material	Contact Angle with Water $\theta°$	Contact Angle with Glycerin $\theta°$	Contact Angle with α-Bromonaphthalene $\theta°$
Glass Coating on Visor Concave Side	61.5 ± 1.4	54.7 ± 0.4	32.2 ± 1.6
Glass Coating on Visor Convex Side	74.5 ± 1.0	78.4 ± 1.7	36.7 ± 1.5
PDMS Silicone with IBMM	81.3 ± 2.6	82.8 ± 1.4	51.5 ± 2.9
Si(100) As-Received	38.0 ± 0.8	31.3 ± 0.5	19.9 ± 0.5
Si(100) Passivation-Sample	69.3 ± 0.5	60.9 ± 0.6	47.1 ± 0.8
Si(100) Anneal-Sample	100.2 ± 0.7	91.9 ± 0.4	58.9 ± 0.6
Si(100) As-Received-1 with IBMM	79.4 ± 0.6	77.7 ± 0.8	22.7 ± 0.5
Si(100) As-Received-2 with IBMM	80.2 ± 1.1	77.6 ± 1.0	24.2 ± 0.4
Si(100) Passivation-Sample-1 with IBMM	75.0 ± 1.1	75.0 ± 0.9	23.6 ± 0.9
Si(100) Anneal-Sample-1 with IBMM	69.1 ± 0.7	72.4 ± 0.7	29.3 ± 1.0

Table 9.

Determination of the SFE identified in the Van Oss theory and the Young-Dupré equation.

Surface Material	Total SFE γ^{Total} (mJ/m^2)	LW Component of SFE γ^{LW} (mJ/m^2)	Base Component of SFE γ^- (mJ/m^2)	Acid Component of SFE γ^+ (mJ/m^2)
Glass Coating on Visor Concave Side	40.6 to 49.7	37.8 ± 1.7	16.8 ± 5.3	0.7 ± 0.4
Glass Coating on Visor Convex Side	34.2 to 47.8	36.0 ± 1.8	18.0 ± 4.8	0.4 ± 0.5
PDMS Silicone with IBMM	31.5	29.2	13.4	0.1
Si(100) As-Received	57.3	41.8 ± 0.5	30.1 ± 3.4	2.0 ± 0.4
Si(100) Passivation-Sample	38.7	31.3 ± 1.3	12.5 ± 2.5	1.1 ± 0.5
Si(100) Anneal-Sample	26.0	25.5 ± 1.3	2.1 ± 1.4	0.03 ± 0.09
Si(100) As-Received-1 with IBMM	45.4	41.0 ± 0.4	10.8 ± 1.9	0.4 ± 0.2
Si(100) As-Received-2 with IBMM	44.3	40.6 ± 0.3	9.9 ± 3.1	0.4 ± 0.3
Si(100) Passivation-Sample-1 with IBMM	45.1	40.8 ± 0.7	14.0 ± 4.4	0.3 ± 0.3
Anneal-Sample-1 with IBMM	43.1	38.9 ± 1.0	20.0 ± 3.5	0.2 ± 0.2

CHAPTER 7

TAPPING MODE ATOMIC FORCE MICROSCOPY AND SURFACE TOPOGRAPHY ANALYSIS

7.1 Motivation and Requirements for Studying the Role of Topography during Wetting or Fogging on Hydrophobic and Hydrophilic Si-based Surfaces

After determining the three components of SFE, through Sessile drop contact angle measurements using three different liquids in the previous chapter, the next step in investigating condensation is to characterize the second key surface property which makes a surface hydrophobic or hydrophilic. This second fundamental property of surface phases is its nanoscopic geometry. Nanoscale geometry is controlled by both the molecular structure and the microstructure of the surface constituents and resulting topography. The foundational experiments that led to a phenomenological model of wetting enabled this research to identify the fundamental properties to be investigated in order to test this model in this dissertation, were described in Chapter 2.

Surface features and roughness impact both the curvature of droplets during nucleation, and provide heterogeneous nucleation sites which can either expedite or slow down the rate of condensation. Thus the technique used to determine topography has to enable for the characterization of the surface topography of Si-based surfaces, with and without a HPMC cellulose film, and to provide both descriptive and qualitative comparisons of the different physical attributes of each surface topography investigated. Mechanical contours of surfaces by AFM are one such characterization tool which enables quantitative

analysis of the surface topography at the nanoscale level. AFM has been widely used in studying surface topography and roughness from sub-nm to μm due to the ability to measure minute forces < 10^{-8} N near the surfaces [124, 125]. In particular, polymers and silica surface have been extensively and successfully characterized by AFM [126].

7.2 Overview of AFM, TMAFM, Roughness and Power Spectra Analysis

AFM is a surface characterization method that of measures topography at the atomic resolution using a mechanically based sharp tip that is rastered or scanned over a specific area, and was one of several iterations of scanning probes derived from the invention of the scanning tunneling microscope, a characterization tool which uses an electron beam as its scanning probe to obtain unprecedented resolution of the physical surface at the atomic level [127-129].

AFM microscopes have several modes of operation, including contact mode AFM and non-contact mode AFM, both of which were the predecessors of the so-called tapping mode AFM, [130, 131]. All AFM microscopes operate on the same basic principle of using a sharp probe mounted on a flexible cantilever which then scans the surface. In contact mode AFM, the tip is maintained into continuous physical contact with the surface, where physical contact is defined as measurable interaction with the surface atomic and intermolecular potentials. The tip is rastered in the x and y directions across the surface, achieved by using piezocrystals. A piezocrystal lengthens or shortens depending upon the voltage applied along one of crystal axes. Each piezocrystal requires a precise calibration procedure to correlate the crystal's motion relative to applied voltage. As the

cantilever deflects due to the rise or fall of the surface features, the laser moves correspondingly on the photodiode. The AFM system typically operates to keep this deflection to a minimum, therefore the system will have a feedback loop that moves the cantilever in the z height via another piezocrystal. The movement of the vertical z height piezocrystal is mapped as a function of the x and y lateral rastering to produce a three dimensional topographical map that corresponds to the atomic equipotential contours. Note that the tip is always in contact (interacting) with the surface as it contours out the surface's equipotential topography.

On the other hand, non-contact AFM involves no physical contact with the surface. Rather, the tip is oscillated as it is scanned over the surface at a particular frequency and amplitude and the tip then responds to the different force gradients through demonstrating a change in magnitude of oscillation or frequency [132]. However, as the tip has to generally respond to and record the gradient of the van der Waals force interactions between the tip and the sample surface, the tip frequently either oscillates out of range of the van der Waals force or can become trapped at the sample surface in liquid layers from adsorbed gases and water vapor, thus becoming unable to quantify the surface structure [132, 133].

TMAFM uses a cantilever with a tip similar to contact mode AFM, but the tip does not approach the surface in the same way as contact mode AFM does. Instead, an additional piezocrystal is integrated into the cantilever holding assembly. Before imaging and when the cantilever is tens of microns away from the sample surface, the extra piezocrystal is vibrated at various frequencies. The

piezocrystal vibration causes the cantilever to vibrate. The amplitude of the cantilever deflection is detected via a laser reflecting off the cantilever, using a photodiode. By plotting the amplitude of deflection versus the frequency, the user is able to determine the natural frequency. The user selects a frequency near this value, and the piezocrystal near the cantilever will then only be vibrated at that frequency.

As the tip nears the surface, the amplitude decreases. This reduced amplitude is then the new value used. As the tip is continuously oscillating above the surface, a significant benefit of TMAFM is that the cantilever is no longer in continuous contact with the sample, thereby reducing the horizontal friction force between the tip and the surface, and minimizing the lateral force of the tip along the surface. Any change in the sample's topography (i.e. feature height) increases or decreases the amplitude of vertical oscillation. Through the feedback loop, the maintenance of a constant amplitude and frequency oscillation of the tip is measured via the corrections needed, which then can be mapped as a contour of the topography.

TMAFM was chosen for the present research due to the microstructure, feature scale, and morphology of the topography of the different samples which needed characterization in this work:

(a) soft and easily damaged PDMS silicone IOLs,

(b) fused quartz silica samples cut from optically transparent 6" wafers,

(c) glass coated high impact polycarbonate Oakley visor, and

(d) hydrophilic HPMC cellulose.

Contact mode AFM is prone to damaging the surface of delicate or soft samples due to continuous physical contact of the tip with the surface and thus the effective “scratching” and “dragging” across the delicate surface and its adsorbate layers of molecules. The continuous contacting induces a shearing, friction force component that is potentially destructive to the surface morphology [131]. On the other hand, non-contact AFM may not be able to measure subtle potential gradient changes on the sample surface due to the oscillating tip’s lack of proximity to the surface.

TMAFM is essentially a combination of both the contact mode and non-contact mode AFM. The tip and cantilever are oscillated to a near resonant frequency and then brought into near contact to the surface. The tip then intermittently contacts the surface at the set frequency. Thus, destructive friction and shearing forces are largely avoided, which is the drawback of contact mode AFM, while the van der Waals forces are detected due to the tip’s oscillating proximity to the surface, while minimizing the drawback of non-contact AFM [134, 135].

Thus, with TMAFM, the complete range of topography found on the surfaces investigated in the present dissertation can be measured and data collected for each of the materials: flexible hydrophobic PDMS silicone, hydrophilic quartz silica, and slightly hydrophilic glass coated polycarbonate visor, with and without HPMC cellulose film, with and without IBMM.

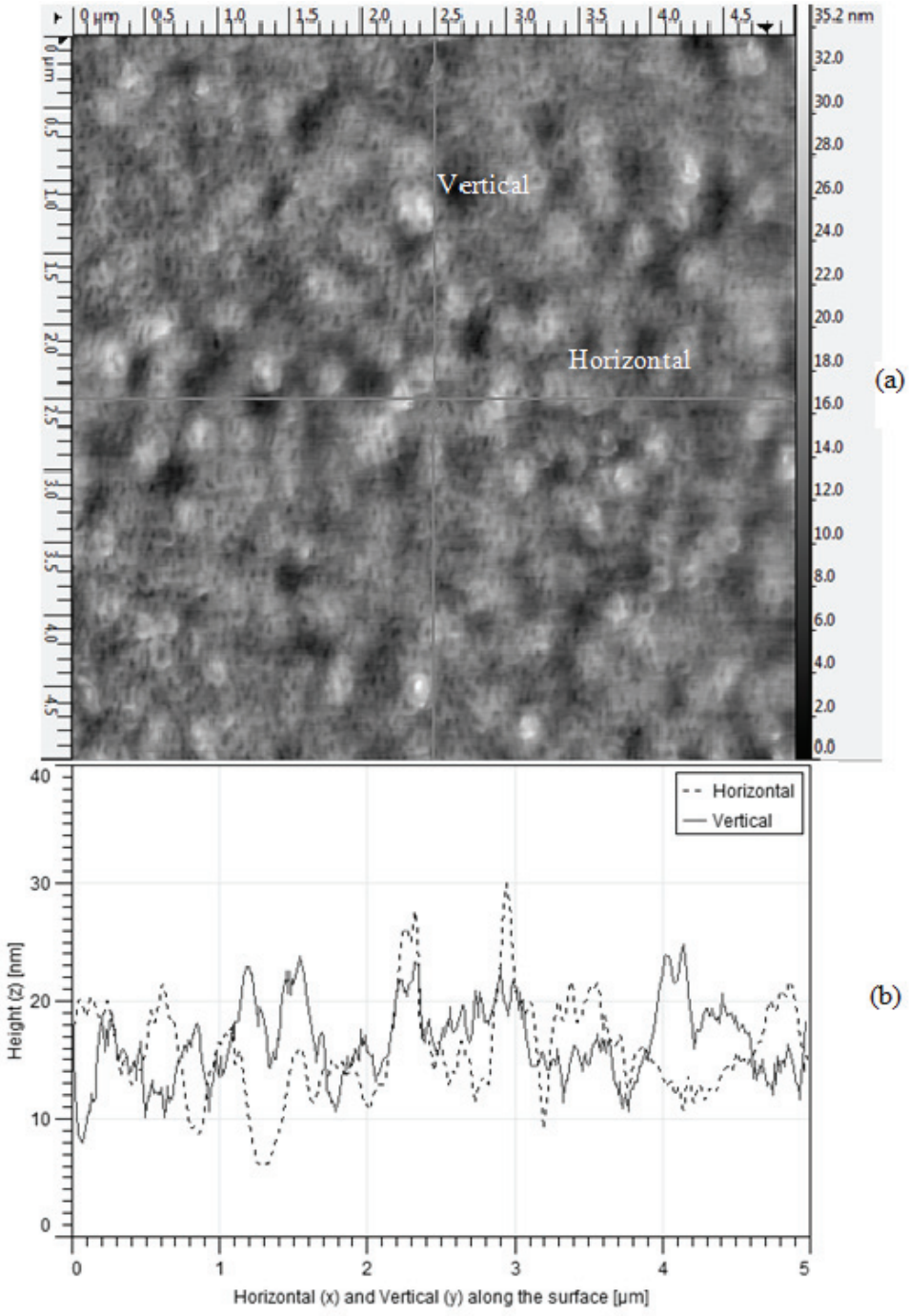

Figure 57.

(a) TMAFM 5 µm × 5µm image of PDMS silicone lens, (b) Topographical line scans contours height versus horizontal (dashed line) and height versus vertical direction cross sections of the surface.

A preliminary study to compare the topography between two types of optical surfaces, namely hydrophilic acrylic lenses and hydrophobic PDMS silicone lenses laid the groundwork for the present systematic investigation. It enabled our group to identify that the roughness and wavelength of both hydrophilic and hydrophobic medical grade IOLs used in cataract surgery can be characterized and compared by TMAFM. For an example, a PDMS silicone sample image and cross section is shown in Figure 57.

7.3 Experimental Apparatus and Procedure

All AFM measurements were conducted on an AFM PicoPlus manufactured by Agilent. This AFM was in each experiment always operated in ambient air with a silicon tip in AC mode. Samples with small surface area, such as the flexible PDMS silicone IOLs whose diameter range from 4 mm to 7 mm, required a special sample holder where glue is used on the mount to keep the sample securely attached during TMAFM characterization.

The piezocrystal vibration frequency is empirically optimized by trial and error by plotting the amplitude of the cantilever deflection as a function of the frequency, while the tip hovers about 100 μm to 200 μm from the tip. The typically initial resonance frequency to tune suggested by the manufacture is around 300 kHz. Actual experimental scan ranges from 250 kHz to 350 kHz. The optimal frequency is slightly different each time a sample is attached to the holder, and selected by maximizing the amplitude with an offset of -0.3 kHz.

The surface area is scanned by collecting a discrete map of 250,000 data points using a resolution of 512 pixel × 512 pixel regardless of the actual scanned

area. The scanned area can vary from 1 μm × 1 μm to 10 μm × 10 μm depending on feature size. For a 5 μm × 5 μm sample, the resulting lateral resolution is about 10 nm (per pixel). Selection of the size of the scanned area is based on the topography of the surface. If the area scanned is large, the lateral resolution is low and small size and wavelength features are missed. On the other hand, when the scanned area is too small, the lateral resolution increases, but at a cost of missing patterns with larger wavelength. For each image acquired, several initial scans are done to determine the optimal scan area based on a preliminary cross sectional analysis via two independent line-scans as described in the preliminary study discussed, as seen in Figure 57.

Large area samples such as 4" × 3" glass coated polycarbonate visors provided by Oakley Corp., and the 6" quartz silica wafers are cut to a size of roughly 1 cm × 1 cm before mounting them on the sample holder. The IOLs, being only a few mm in diameter, do not need to be cut before mounting. Because of both IOL and visor samples possess a significant degree of curvature, they are secured by gluing them to the sample holder magnetic disk. The quartz silica samples are mounted after cutting to the sample holder magnetic disc using double sided sticky tape. The magnetic sample holder is then attached to the sample holder and secured by the magnets.

7.4 Method for Quantitative AFM Data Analysis

Starting with the acquired AFM contour maps, the roughness parameters, and power spectral density function (PSDF) are extracted using specific software called Gwyddion [136].

7.4.1 Statistical Method for the Extraction of Topographical Roughness Parameters

The root mean square (RMS) roughness is easily defined by the quadratic root of the squared vertical deviations from the surface baseline divided by the number of data points minus 1,

$$R_{RMS} = \sqrt{\frac{\sum_{n=1}^{N}\left(z_n - \bar{z}\right)^2}{N-1}} \tag{25}$$

where

z_n is the vertical height of each sampled data point,

$\bar{z}$ is the average vertical position of the surface of z_n.

Thus the RMS roughness really represents the standard deviation of the surface height from its average [137].

The mean vertical slope of features in the surface profile is,

$$\Delta_a = \frac{1}{N-1}\sum_{n=1}^{N-1}\left|\frac{\partial z_n}{\partial x_n}\right| \tag{26}$$

where

z_n is the vertical height of each sampled point,

x_n is the horizontal position of each sampled point.

By calculating the average of all mean vertical slopes between each two successive points of the profile, we arrive at the equation expressing the average lateral distance of wavelength along which a full scale height variation is found or oscillation; this quantity is called average wavelength λ_a and can be computed

via the following expression, which is a simple statistical deviation average over N points,

$$\lambda_a = \frac{2\pi}{\Delta_a} \frac{\sum_{n=1}^{N} |z_n - \bar{z}|}{N} \tag{27}$$

where

z_n is the vertical height of each sampled point,

$\bar{z}$ is the average of z_n,

Δ_a is the mean slope as in Equation (26) above.

This calculates the lateral spacing between local peaks and valleys, and considers their relative amplitudes and individual spatial frequencies [137].

On each surface, the acquired contour map is analyzed systematically at four pre-set locations. The one dimensional RMS roughness, mean slope, and average wavelength are computed at these four different locations and this 4-point statistical mean are the values reported. The selection of the four locations where the topographical parameters are sampled is shown in Figure 58; a horizontal line centered in the image along the surface, labeled (1), the line vertical to the first, also centered in the image labeled (2), and two diagonal lines (3) and (4). Note that the sample horizontal and vertical topographies are symmetrically equivalent (Figure 62).

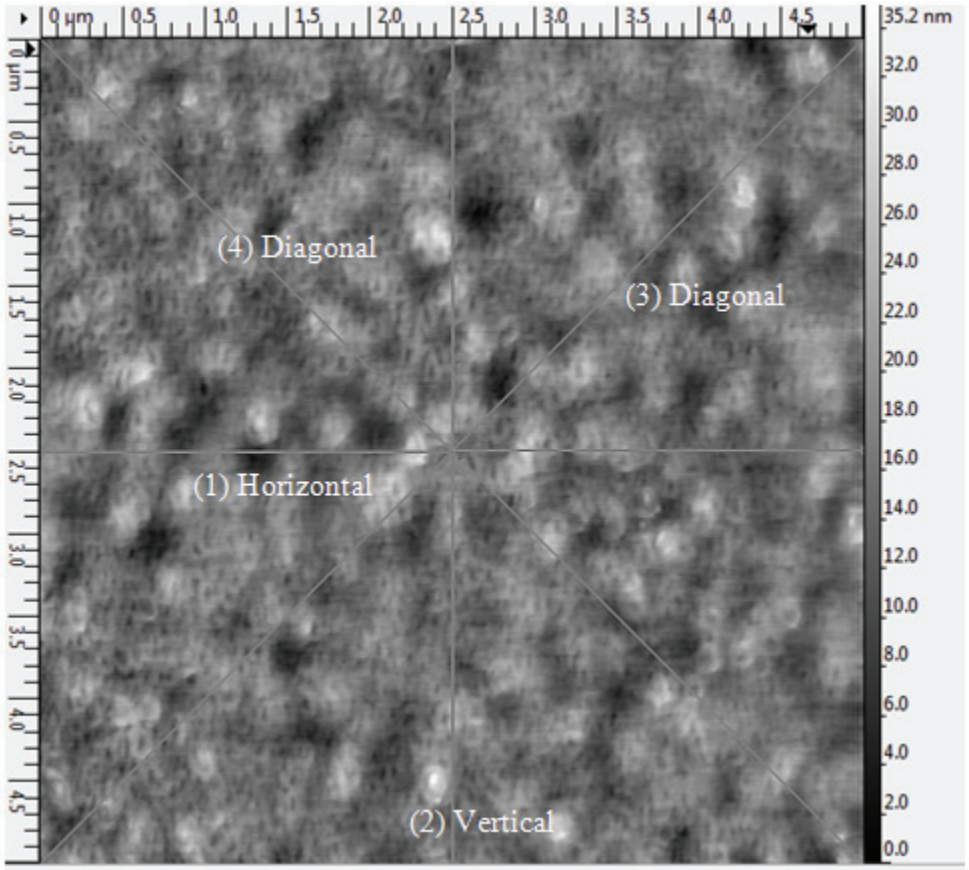

Figure 58.

TMAFM 5 µm × 5µm image of a PDMS silicone IOL. Line (1) to (4) depict four axes along which cross sectional analysis of the topography is performed and roughness parameters computed. All values reported in the present dissertation are a statistical average along these four lines.

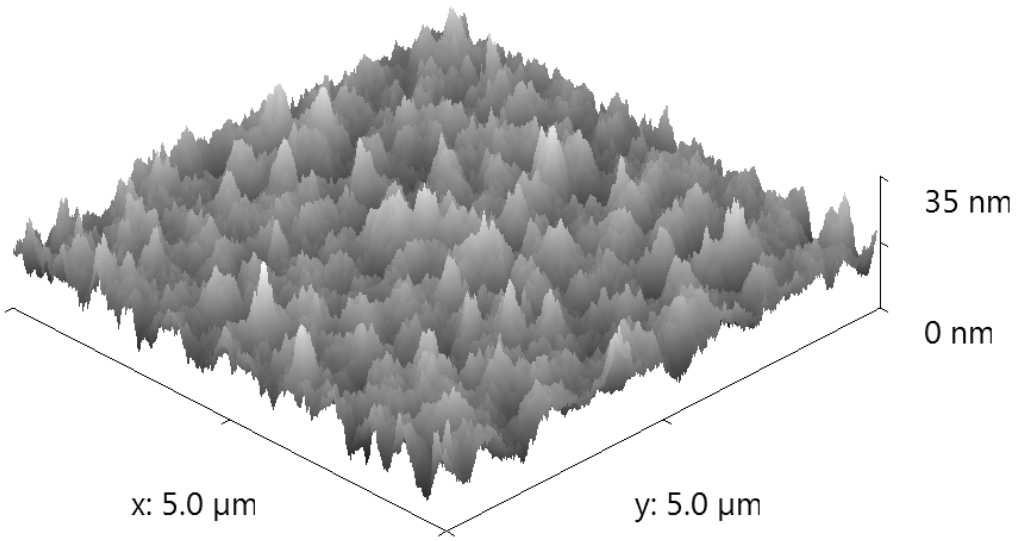

Figure 59.

TMAFM 5 µm × 5µm 3d image of the surface of flexible PDMS silicone IOL.

The three roughness parameters selected in this work to characterize the surface topography of Si-based surfaces are thus RMS, Δ_a and λ_a are extracted from the four lines statistical analysis discussed above. They are listed for each surface in Table 10. Their significance is below and discussed later in Chapter 8.

Table 10.

Roughness parameters extracted from TMAFM images on (a) PDMS silicone IOL, (b) 6" quartz silica wafer, and (c) glass coated polycarbonate visors provide by Oakley; before and after adsorption of hydrated HPMC cellulose film.

Surface Type	RMS Roughness R_{RMS} (nm)	Average Wavelength λ_a (μm)	Average Slope Δ_a
PDMS Silicone	3.7 ± 0.2	0.28 ± 0.03	0.067 ± 0.004
Silica Wafer	0.42 ± 0.05	0.22 ± 0.03	0.0094 ± 0.008
Glass Coating on Visor Concave Side	1.14 ± 0.09	0.27 ± 0.01	0.0201 ± 0.0008
Glass Coating on Visor Convex Side	1.49 ± 0.15	0.22 ± 0.02	0.032 ± 0.002
1% wt. HPMC on PDMS Silicone	0.31 ± 0.01	0.16 ± 0.01	0.0098 ± 0.0004
1% wt. HPMC on Silica Wafer	0.192 ± 0.009	0.16 ± 0.02	0.0064 ± 0.0007
0.2% wt. HPMC on Silica Wafer	0.34 ± 0.04	0.16 ± 0.02	0.0110 ± 0.0007
1% wt. HPMC on Visor Concave Side	0.25 ± 0.02	0.19 ± 0.02	0.0069 ± 0.0007
0.2% wt. HPMC on Visor Concave Side	1.77 ± 0.01	0.21 ± 0.02	0.055 ± 0.005

7.4.2 Topography Analysis via Power Spectral Density Functions

A PSDF is obtained from the Fourier transformation of the autocorrelation function with respect to the repeating pattern of surface features. A PSDF can be used to map the specific distribution of surface features as a function of their spatial frequency [126, 136]. In general extraction of PSDF maps have applications in several areas, including optics [138, 139], and the roughness of superconducting Niobium accelerators [140].

Because the samples are symmetrical in x direction and y direction along the surface, a unique one dimensional PSDF is used here. The presence of a maximum in the distribution, at a given wavelength indicates a repeating pattern of features at that wavelength along the surface.

As stated before, 5 μm × 5 μm scanned area are acquired in a 512 pixel × 512 pixel matrix, which resultsin a lateral spatial resolution along the surface of approximately $\frac{5\mu m}{512}$ or 10 nm. Therefore, the wave number k would range from $\frac{2\pi}{5\mu m}$ to $\frac{2\pi}{10nm}$ as shown in Figure 60 in a logarithmic scale.

The same concept is applicable to a 1 μm × 1 μm scanned area with 512 pixel × 512 pixel, which results in a lateral spatial resolution along the surface of approximately $\frac{1\mu m}{512}$ or 2 nm. This results in a wave number k range from $\frac{2\pi}{1\mu m}$ to $\frac{2\pi}{2nm}$ as shown in Figure 61. Therefore, to make a direct comparison between surfaces, a consistent scan area and spatial resolution is important. In this work, we ensure that all comparisons are made from identically-sized scanned areas.

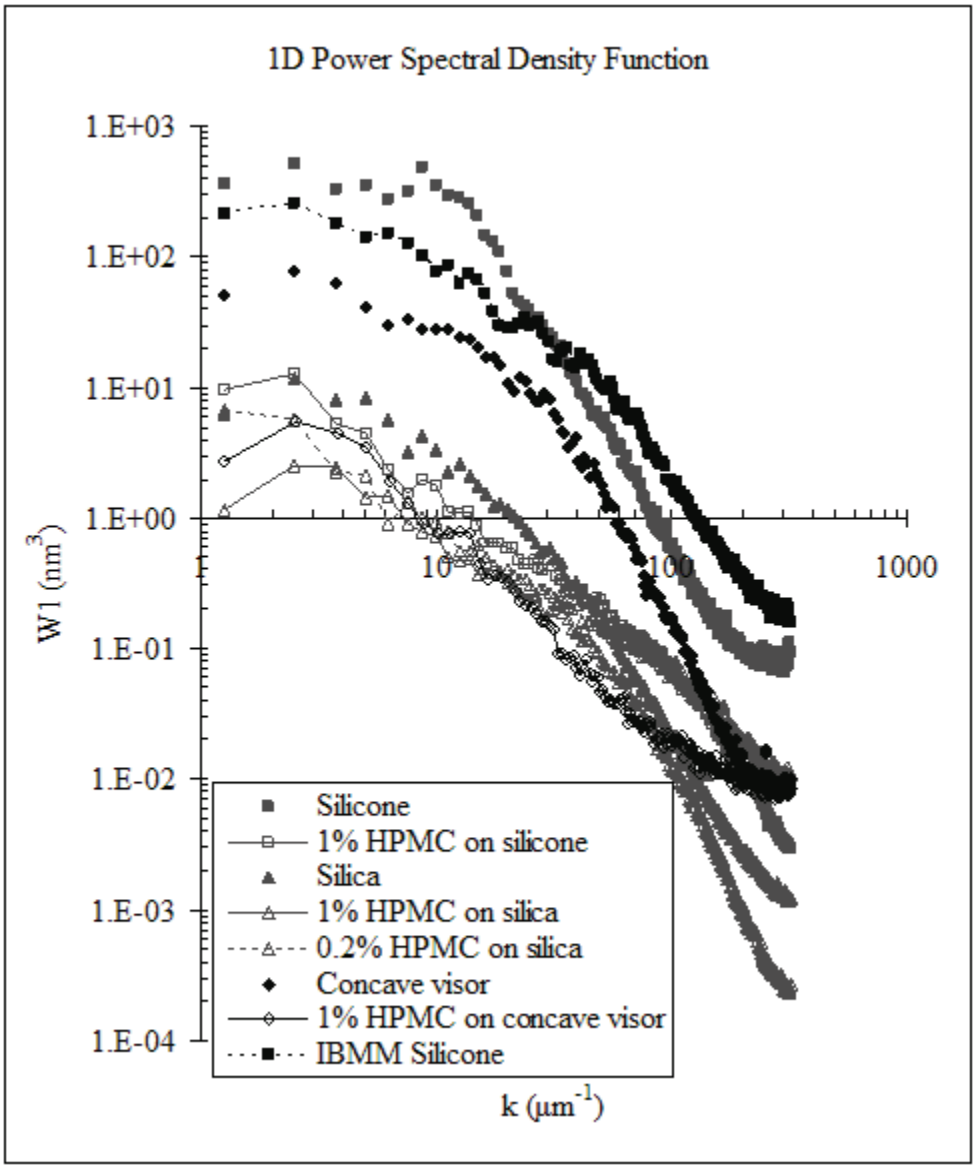

Figure 60.

PSDF on a 5 µm × 5 µm scan with a 512 pixel × 512 pixel. Surfaces compared are (1) PDMS silicone (2) 1 % wt. HPMC cellulose on silicone, (3) quartz silica, (4) 1% wt. HPMC cellulose on silica (5) 0.2% wt. HPMC cellulose on silica, (6) concave side of glass coated visor, (7) 1% wt. HPMC cellulose on concave side of glass coated visor and (8) IBMM PDMS silicone. Note that the intensity decreases by about two orders of magnitude after adsorption of cellulose.

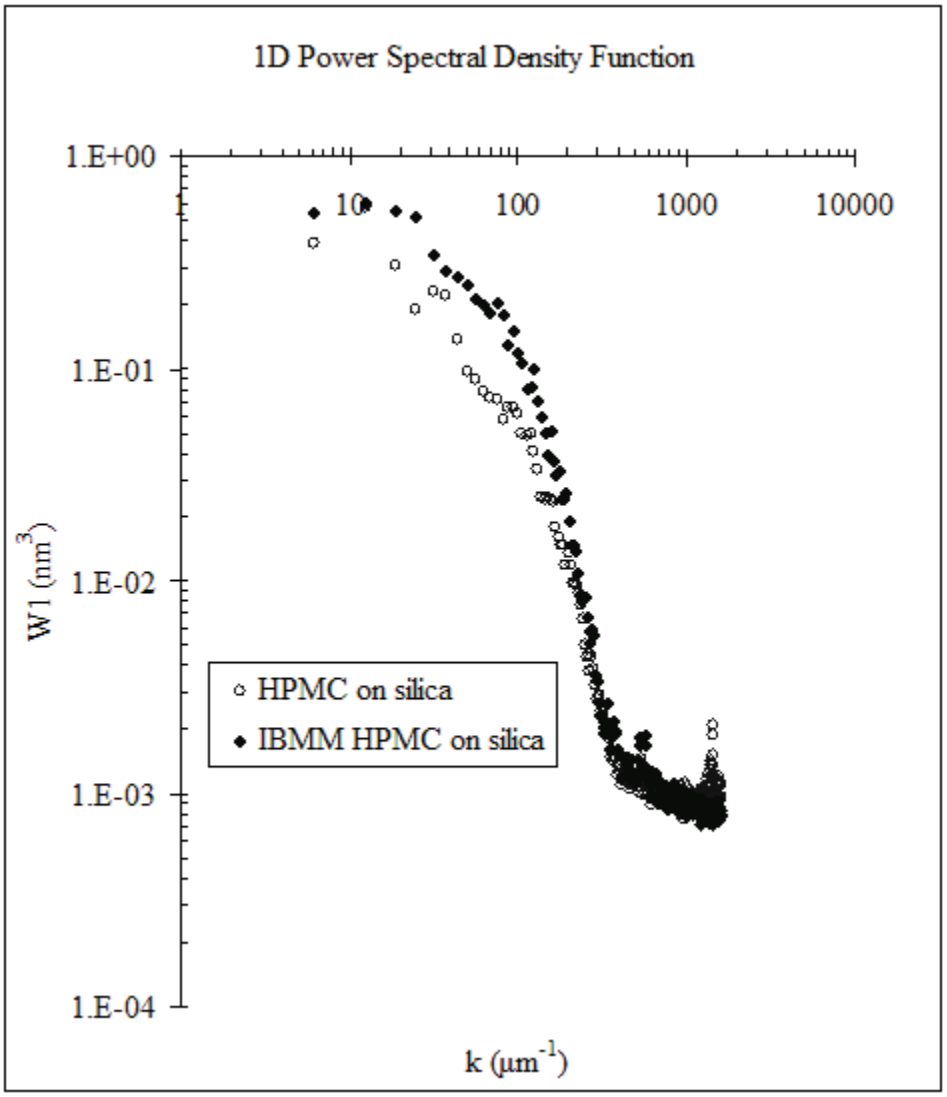

Figure 61.

PSDF on a 1 µm × 1 µm scan with a 512 pixel × 512 pixel. Surfaces compared were HPMC cellulose 1% wt. on silica prior to IBMM, and the same sample measured after IBMM.

CHAPTER 8

RESULTS AND DISCUSSION

8.1 Water Affinity and Condensation of Silica Wafer, PDMS Silicone, and Glass Coating

8.1.1 Verification of Contact Angle Measurements by Direct Comparison to Data Reported in the Literature

Systematic contact angle measurements using three different test liquids yields the three SFE components identified in the Van Oss theory, as were reported in the literature for generic silica and generic PDMS silicone, and listed in Table 11. The total SFE for hydrophilic generic silica reported in the literature is greater than that of generic PDMS silicone reported in the literature by nearly a factor of three, with PDMS silicone exhibiting a $\gamma^{Total} = 20.2$ mJ/m^2 while silica exhibiting a much higher $\gamma^{Total} = 59.1$ mJ/m^2. The source of such a difference between a silica wafer, with the SiO_2 being of electronic grade, and PDMS silicone $SiOC_2H_6$, can be attributed to the difference in value from the contribution of the polar component of the SFE, i.e. Lewis acid base combined polar component $2\sqrt{\gamma^+\gamma^-}$. While the difference in the contribution from LW intermolecular interaction to SFE is about a factor of two larger for silica than PDMS silicone, the contribution from the polar component in SiO_2 is 22 times that of PDMS silicone. This significant difference results in silica having a much higher SFE and thus a hydrophilic behavior while PDMS silicone has a much lower SFE and a hydrophobic behavior. This is also evident from their respective contact angles.

PDMS silicone similar to the one used in this research was reported to have a contact angle of 107.2°, close to the angle of 104.6° ± 1.4° measured in this work[123]. The values reported and the values we measured are within 2.5° or 2.5% of each other. Hence, these measurements are considered to be in good agreement with each other and thus establish that hydrophobic PDMS silicone can be quantitatively characterized. Similarly, the reported value for hydrophilic silica is 30.8°, while for this work an average value of 32.2° ± 1.9° was measured [20]. The error bar for the value measured overlaps the reported value, and is thus within 1.4° of each other. Though the measurement error for this smaller angle is larger, 5%, it is still quite accurate for an absolute measurement of contact angle.

Table 11.

SFE of PDMS silicone and silica wafer as reported in the literature. The corresponding reported contact angle with water is compared to the contact angle measured in this work. Close agreement is found between the reported values and this work that correspond to the hydrophobic and hydrophilic behaviors of these two surfaces. Hence this table establishes that water affinity can be properly and consistently characterized by the method and apparatus developed in the present dissertation.

Surface Material	Total SFE γ^{Total} (mJ/m^2)	LW Component of SFE γ^{LW} (mJ/m^2)	Base Component of SFE γ^- (mJ/m^2)	Acid Component of SFE γ^+ (mJ/m^2)	Contact Angle with Water θ°
PDMS Silicone	20.2 [123]	19.4 [123]	0.8 ($\gamma^{polar}=2\sqrt{\gamma^+\gamma^-}$) [123]		107.2 [123] 104.7 ± 1.4[1]
Silica Wafer	59.1 [20]	41.3 [20]	35.68 [20]	2.21 [20]	30.77[2] 32.2 ± 1.9[1]

[1] From this work
[2] Determined using Equation (18) and SFE from [20]

8.1.2 Contact Angle and SFE for Glass Coated Polycarbonate Visors

The contact angles and SFE of the polycarbonate visors coated with glass and provided by Oakley as examples of a glass coating with high impact resistance are shown in Table 12 and Table 13 respectively. The results for contact angle measurements with three different test liquids and the resulting SFE components and total SFE determined from these contact angles show that the visor samples are slightly hydrophilic. The values for the contact angles with water range between 60° and 75° and thus fall between the now well established

value for hydrophobic PDMS silicone and hydrophilic silica. Henceforth, both the total SFE measured for convex and concave glass coated polycarbonate visors provide by Oakley fall between hydrophobic PDMS silicone and hydrophilic silica. The total SFE is typically in the range of 40 mJ/m^2, thus about twice as large as hydrophobic PDMS silicone's total SFE, and about 30% lower than hydrophilic silica. The convex side of the glass coated polycarbonate visors provided by Oakley is slightly more hydrophobic by about 12° greater than the concave side in contact angle and 4 mJ/m^2 in total. This gives a sense on how the surface geometry and resulting surface tension on the silica coating affects the total SFE.

Table 12.

Contact angle measured for each of the three test liquids on glass coated polycarbonate visors provided by Oakley.

Surface Material	Contact Angle with Water $\theta°$	Contact Angle with Glycerin $\theta°$	Contact Angle with α-Bromonaphthalene $\theta°$
Glass Coating on Visor Concave Side	61.5 ± 1.4	54.7 ± 0.4	32.2 ± 1.6
Glass Coating on Visor Convex Side	74.5 ± 1.0	78.4 ± 1.7	36.7 ± 1.5

Table 13.

SFE determined from contact angle measurements for glass coated polycarbonate visors provided by Oakley.

Surface Material	Total SFE γ^{Total} (mJ/m^2)	LW Component of SFE γ^{LW} (mJ/m^2)	Base Component of SFE γ^{-} (mJ/m^2)	Acid Component of SFE γ^{+} (mJ/m^2)
Glass Coating on Visor Concave Side	40.6 to 49.7	37.8 ± 1.7	16.8 ± 5.3	0.7 ± 0.4
Glass Coating on Visor Convex Side	34.2 to 47.8	36.0 ± 1.8	18.0 ± 4.8	0.4 ± 0.5

8.1.3 Surface Topography and Fogging during Water Condensation

The surface topography of all three high quality surfaces were studied for their water affinity: PDMS silicone used for IOLs, silica samples from fused quartz silica wafers, and glass coated polycarbonates used for high impact visors, and were characterized by TMAFM and the method described in Chapter 7. The topography 3d images and roughness parameters chosen for extraction from TMAFM imaging and analysis are shown in Figure 62 and Table 14. The imaging areas were consistently kept to 5 μm × 5 μm. The method developed in this dissertation focused on extracting:

(a) the RMS roughness R_{RMS}, found to be in the nm range;

(b) the average wavelength λ_a, found to fall in the 100 nm range of the surface height, and describes the "width" of each full oscillation between surface peaks; and

(c) the average peak to peak slope Δ_a in the surface oscillation.

The approach of using these three roughness parameters is made possible by the consistent sample topography, which shows a fairly periodic surface pattern with evenly distributed oscillations of the surface heights akin to dunes on a beach. Table 14 lists a direct comparison of the three surfaces studied here using the same three topographical parameters selected to characterize quantitatively these three different surfaces. Most notably, the R_{RMS} of PDMS silicone used for the IOLs is 3.7 ± 0.2 nm, and thus an order of magnitude which is about 9 times greater than that of the silica which is only 0.42 ± 0.05 nm. The rate of change Δ_a of the PDMS silicone is found to be about 7 times greater since the oscillation wavelengths are similar. The R_{RMS} value of the concave side and the convex side of the glass coated polycarbonate visors differ from both the rougher PDMS silicone and the smoother silica wafer. Both concave and convex sides yield R_{RMS} of about 1 nm. However, the wavelength λ_a of each of the three materials fall consistently within the same range, which means fluctuations in height repeat on average every few hundreds of nm, ranging between 0.2 μm and 0.3 μm. Therefore, the PDMS silicone used for IOLs provides the most significant capillary features at the nanoscale level, while the silica surface is considered the most “flat”.

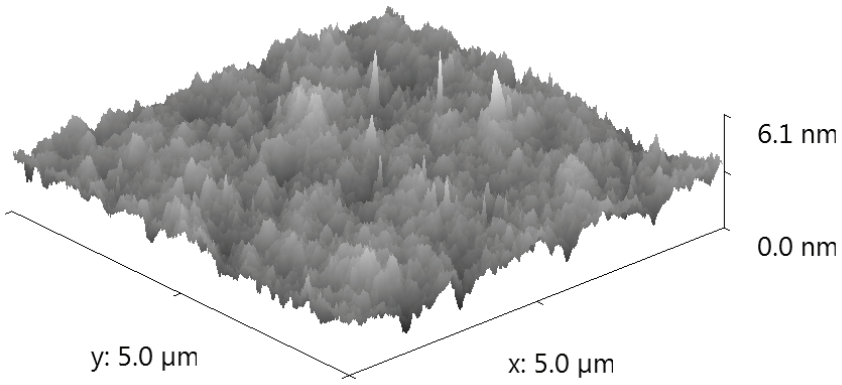
6.1 nm
0.0 nm
y: 5.0 µm
x: 5.0 µm

(a)

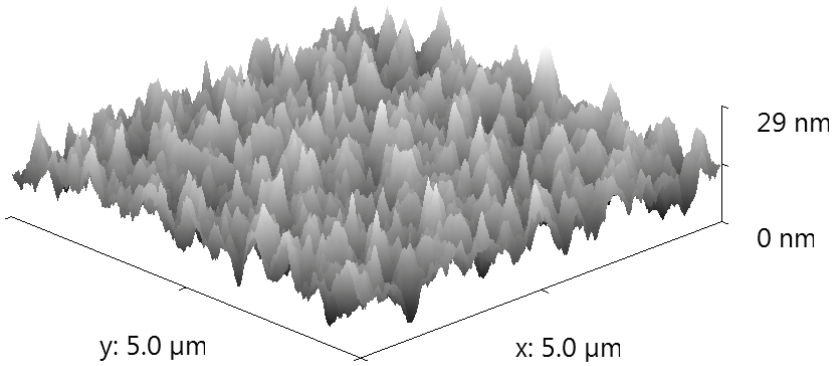
29 nm
0 nm
y: 5.0 µm
x: 5.0 µm

(b)

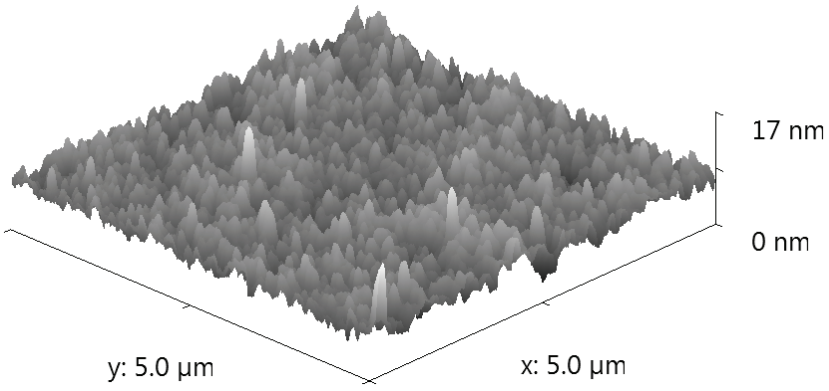
17 nm
0 nm
y: 5.0 µm
x: 5.0 µm

(c)

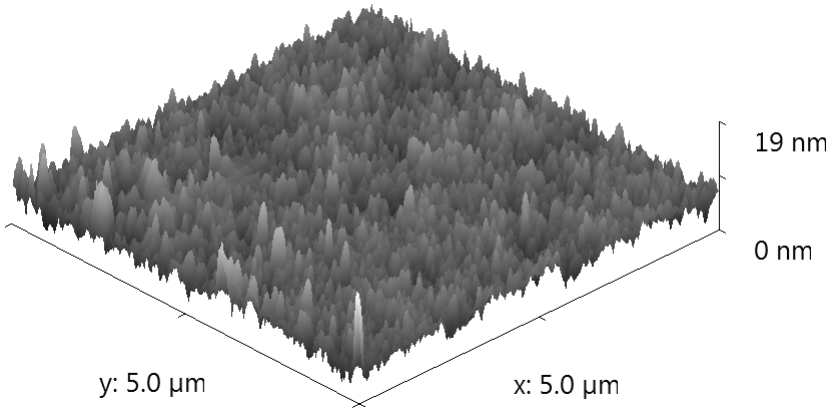

(d)

Figure 62.

TMAFM 5 µm × 5µm images of (a) hydrophilic Silica with a z-scale of 6 nm, (b) PDMS silicone with a z-scale of about 30 nm, (c) concave side of a glass coated polycarbonate visor with a z-scale of 17 nm, and (d) convex side of glass coated polycarbonate visor with a z-scale of 19 nm. The topography of each sample clearly demonstrates that all four surfaces exhibit a periodic surface pattern with evenly distributed oscillations of the surface heights akin to dunes on a beach, without multiple distributions of strongly differing features. The images also show that the average height of features varies strongly between each surface, with silica being the smoothest, as expected, PDMS silicone being the roughest, and glass coated polycarbonate falling in between the two, also expected from a glass coating (being relatively smooth) on a rough polymer surface. Table 14 tabulates the roughness parameters extracted from these images.

Table 14.

Roughness parameters extracted from TMAFM for PDMS silicone, silica wafer, and glass coated polycarbonate visors provide by Oakley.

Surface Type	RMS Roughness R_{RMS} (nm)	Average Wavelength λ_a (μm)	Average Slope Δ_a
PDMS Silicone	3.7 ± 0.2	0.28 ± 0.03	0.067 ± 0.004
Silica Wafer	0.42 ± 0.05	0.22 ± 0.03	0.0094 ± 0.008
Glass Coating on Visor Concave Side	1.14 ± 0.09	0.27 ± 0.01	0.0201 ± 0.0008
Glass Coating on Visor Convex Side	1.49 ± 0.15	0.22 ± 0.02	0.032 ± 0.002

The differences in the condensation behavior of PDMS silicone used for IOL and silica wafers can be explained by the morphology of their surfaces as measured by TMAFM and by the water affinity as characterized by the Sessile drop contact angle measurements reported above in Table 12 and Table 13.

The RMS roughness R_{RMS} and topography of optical quality PDMS silicone used for IOLs was characterized for the first time in this work. R_{RMS} of less then 4 nm was consistently observed over several hydrophobic PDMS silicone IOL samples, and each sample at different spots. This is compared to silica wafers, with an R_{RMS} of about 0.4 nm. This surface topography allows for rapid heterogeneous nucleation of water droplets observed typically within a few

seconds. Thus, almost immediate fogging during condensation is seen in Figure 63(c). However, because of the low SFE and water affinity, each individually nucleated condensed water droplet is spatially separated from each other. Hence it cannot easily coalesce into a continuous wet film or grow and diffuse rapidly into larger droplets. The average size of the nuclei after 3 seconds exposure to saturated water vapor at 38 °C is less than 0.05 mm, or less than 50 μm as seen in Figure 63(c). The PDMS silicone surface thus remains covered by fairly small droplets between time t = 0 and t = 3 seconds of growth during condensation. The optical image in Figure 63(d) is taken after further condensation for a total duration of 90 seconds, or a duration that is 30 times longer. It shows that the "fog" is formed by distinct water droplets. They have grown about 4 times larger to an average size of 0.2 mm after 90 seconds total of continuous exposure to a saturated water vapor at 38°C. Since the SFE of hydrophobic PDMS silicone is low compared to that of the hydrophilic silica wafers, the water does condense into spherical droplets with a well defined contact angle of 104.7 ± 1.4 ° as measured in this work and listed in Table 6. The droplet shape can thus be characterized as water "beads" with a radius of curvature of the same order as half their lateral size, about 0.2 mm above the surface.

The condensation behavior on silica wafers is quite different, as shown in Figure 63(a) after a condensation of 30 seconds and in Figure 63(b) after 90 seconds. Because these silica wafers are about an order of magnitude smoother than the PDMS silicone used for IOLs, much fewer heterogeneous nucleation sites are available.

The time elapsed to start observing the formation of a condensate on silica is much longer than for PDMS silicone. In other words, it takes about an order of magnitude longer duration, 30 seconds rather than 3 seconds, to observe optically the nucleation of water droplets of the same caliber. However, once these droplets are nucleated, due to the high surface free energy, the resulting condensation on the silica tends to coalesce faster than that on the silicone. As a result, instead of a fine mist like fog as seen on the silicone, the condensation rapidly takes on the form of "puddles" of water spaced over the silica.

The convex and concave sides of the visors with a root mean square roughness of up to1 nm provide nucleation sites for water condensation faster than silica but slower than silicone. A slightly hydrophilic surface will indicate that the surface condensation pattern will be puddle-like upon ripening.

We can explain the differences in the condensation behavior which the PDMS silicone and silica experience and further show how the morphology and water affinity affect condensation behavior. PDMS silicone is much rougher than silica, and hence one can imagine that each peak-valley-peak can be modeled as a capillary-like structure. This allows for almost immediate condensation as seen in Figure 63(c). However, because the roughness effectively isolates each condensed water drop, the total condensation area remains finely fogged from a macroscopic view, as seen in Figure 63(d). Since the SFE is relatively low compared to the silica, the condensed water drops tend to form water "beads". The condensation behavior on the silica is quite different, as seen in Figure 63(a) and Figure 63(b). Because of its smoothness, it takes much longer than the PDMS silicone for water

droplets to nucleate on its surface. However, once these droplets are nucleated, due to the high SFE, the resulting condensation on the silica tends to coalesce faster than that on the PDMS silicone. As a result, instead of a fine mist like fog as seen on the PDMS silicone, the condensation rapidly takes on the form of "puddles" of water spaced over the silica.

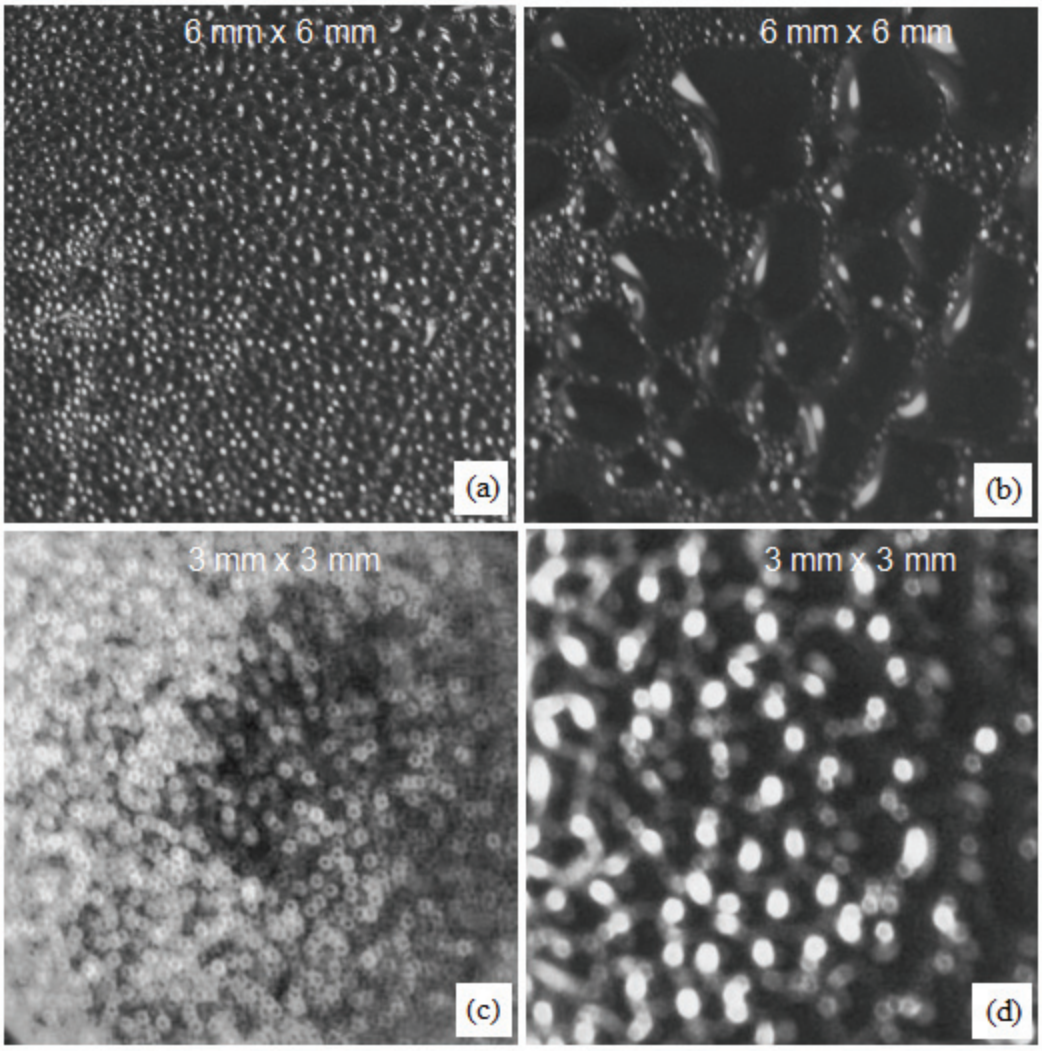

Figure 63.

Condensation test comparing silica and PDMS silicone, with the water temperature at 70 °C. (a) 30 seconds after the silica is placed over the hot water. (b) 90 seconds after silica placement. (c) 3 seconds after PDMS silicone is placed over the hot water. (d) 90 seconds after PDMS silicone placement. Though initial nucleation on PDMS silicone occurs faster than on silica, the nucleated drops tend to remain in place and coalescence is now much slower when compared to coalescence on silica.

8.2 HPMC Cellulose Film on Si-based Surfaces Eliminates Fogging during Water Condensation by Complete Wetting

8.2.1 HPMC Cellulose Film Composition with High SFE and Water Affinity

HPMC cellulose film was used to alter the water affinity of silica, PDMS silicone, and the visor glass coating.

The HPMC cellulose film stoichiometry near the film's surface, measured by 4.265 MeV $^{12}C(\alpha, \alpha)^{12}C$ and 3.045 MeV $^{16}O(\alpha, \alpha)^{16}O$ nuclear resonance scattering combined with ERD of hydrogen, is determined to be $N_C : N_O : N_H = 1.60 : 1.00 : 2.70$, compared to the HPMC bulk stoichiometric ratio of $C_{32}O_{19}H_{60} = 1.68 : 1.00 : 3.16$. This result confirms that the surface composition has taken on the HPMC stoichiometry regardless of substrate type.

HPMC cellulose is a water hydratable polymer which forms a water cage around its polymer chain via hydrogen bonding [70]. The hydratable polymer mesh provides high water affinity which will enhance the coalescence of the nucleated droplets. Indeed, HPMC cellulose has a total SFE γ^{Total} ranging from 39.9 mJ/m^2 to 42.8 mJ/m^2, which is about twice as much as PDMS silicone; the SFE components based on Van Oss theory: γ^{LW} is between 35.8 mJ/m^2 to 37.5 mJ/m^2 which is also twice of PDMS silicone, γ^+ is between 0.15 mJ/m^2 to 0.21 mJ/m^2, and γ^- is between 27.2 mJ/m^2 to 32.3 mJ/m^2 gives combined polar component about 6 times as much as PDMS silicone [141]. Therefore we expect high SFE and water affinity of such HPMC cellulose film on Si-based substrates.

8.2.2 HPMC Cellulose Areal Density Correlates to Wetting

8.2.2.1 Visual Clarity during Water Condensation Correlates to HPMC Cellulose Film Areal Density and Gel Concentration

The HPMC cellulose film was characterized by areal density measurements via ion beam energy loss in conjunction with the respective damage curve extrapolation as shown in Table 2 of Chapter 4. Comparing with the condensation results, and linking the results with the areal densities listed in Table 15, it is shown that a HPMC cellulose film with an areal density ranging from 10^{18} atom/cm^2 to 10^{19} atom/cm^2 on silica and PDMS silicone surfaces can effectively prevent fogging on the silica and PDMS silicone surfaces by forming a complete wetting layer to improve visual clarity. A film that is too thick will cause visual distortion, while too thin of a film may have a wide range of effects, from merely experiencing initial heavy fogging and then clearing, to not being effective at all due to complete fogging, or a combination of these effects.

Table 15.

Visual clarity, HPMC cellulose gel concentration during the preparation of dried films, and areal density of dried films determined using RBS on silica wafer and PDMS silicone substrates.

Substrate Type	Gel Concentration (% wt.)	Visual Clarity	Film Areal Density (10^{15} atom/cm^2)
Silica Wafer	2%	No	.
Silica Wafer	1% Sample #1	Yes	8920 ± 620
Silica Wafer	1% Sample #2	Yes	9680 ± 210
Silica Wafer	1% Sample #3	Yes	8350 ± 700
Silica Wafer	0.33%	Yes	3100 ± 310
Silica Wafer	0.25%	Yes	1087 ± 25
Silica Wafer	0.2%	Yes	1086 ± 55
Silica Wafer	0.1%	No	-
PDMS Silicone	2%	No	-
PDMS Silicone	1%	Yes	6570 ± 250
PDMS Silicone	0.33%	Yes	2730 ± 380
PDMS Silicone	0.25%	Yes	-
PDMS Silicone	0.2%	Yes	-
PDMS Silicone	0.1%	No	-

Note that, even prepared under the same condition, areal density may vary slightly from sample to sample. For an example, three samples prepared using HPMC cellulose gel concentration 1% wt., dried HPMC cellulose film areal density is 8920 ± 620 (10^{15} atom/cm^2), 9680 ± 210 (10^{15} atom/cm^2), and 8350 ± 700 (10^{15} atom/cm^2) respectively. The differences however, are within 15% of each other, estimated from the higher and lower values.

Also note that different substrates may adsorb different amounts of HPMC cellulose prepared using the same gel concentration. For an example, prepared with 1% wt. gel concentration, the HPMC cellulose film areal density on silica wafer is 37% higher than PDMS silicone; prepared with 0.33% wt. gel concentration, the difference is less.

8.2.2.2 Two Independent Methods Confirm the HPMC Cellulose Film Areal Density

Results from the PIXE method as shown in Table 5 of Chapter 5 provide an alternative method for measuring the areal density; the results of which are shown in Table 16. The measurements further confirm that the areal density derived from PIXE is in agreement with the areal density derived from the RBS method for the HPMC cellulose film on silica wafer substrates. For both HPMC cellulose film prepared with 0.5% wt. and 0.4% wt. gel concentration, the two measurements are in agreement with each other.

However, although the areal density measurement is of the same order for the visor glass coating substrates, we observed a discrepancy. This discrepancy may be related to the stoichiometric variations in the glass coating of the visor

samples. In Chapter 5, a stoichiometric variation of $SiO_2C_{2.5}$ to SiO_3C_3 was detected using RBS and RUMP, indicating slight compositional fluctuations. The PIXE method relies on the substrate Si element to be stable in the substrate compound. If the sample substrate is different than the bare calibration substrate, there will be an error as a result. Therefore, the PIXE method performs better on uniform substrates. On the other hand, the RBS method relies on the top most layer of Si detection, and is therefore more accurate when the substrate is not uniform, i.e. as long as the top layer of Si is detected, we can measure the energy loss and determine the areal density of the film. It is also possibly due to the fact that visor concave side has a slight curvature, causing the HPMC cellulose areal density to vary during sample preparation procedure. However, the respective areal density differences caused by the substrate curvature are not fully understood and needs to be explored further.

Table 16.

HPMC cellulose gel concentration during the preparation of the dried film vs. areal density of the dried film determined using PIXE and RBS.

Substrate Type	Gel Concentration (% wt.)	Film Areal Density via PIXE (10^{15} atom/cm^2)	Film Areal Density via RBS (10^{15} atom/cm^2)
Silica Wafer	1.00% wt.	7500 ± 500	-
Silica Wafer	0.50% wt.	4270 ± 560	5000 ± 1000
Silica Wafer	0.40% wt.	3040 ± 580	2700 ± 700
Silica Wafer	0.33% wt.	2100 ± 600	-
Glass Coating on Visor Concave Side	1.00% wt.	16560 ± 170	-
Glass Coating on Visor Concave Side	0.50% wt.	9430 ± 150	6500 ± 500
Glass Coating on Visor Concave Side	0.33% wt.	1430 ± 170	2400 ± 400
Glass Coating on Visor Concave Side	0.20% wt.	1640 ± 160	2000 ± 300

On the Oakley visor glass coating, similar results show that the HPMC cellulose film with an areal density ranging from 10^{18} atom/cm^2 to 10^{19} atom/cm^2

can also effectively prevent fogging on the visor surfaces by forming a complete wetting layer to improve visual clarity. However, initial fogging is more noticeable while the wetting layer is forming. It was also observed that the HPMC cellulose film on the visor surface had a larger wavelength than the HPMC cellulose film on the silica wafer or PDMS silicone. After the initial fogging, rehydration of the polymer forms a complete wetting layer and no further fogging is observed afterwards.

8.2.3 Surface Topography Correlates to Complete Wetting during Water Condensation

TMAFM was used to determine how the HPMC cellulose film modified the surface topography of the respective silica wafer and PDMS silicone substrate as shown in Figure 64. Regardless of different types of substrate, HPMC cellulose film shows a similar, evenly distributed oscillating surface pattern much different than that of the substrate.

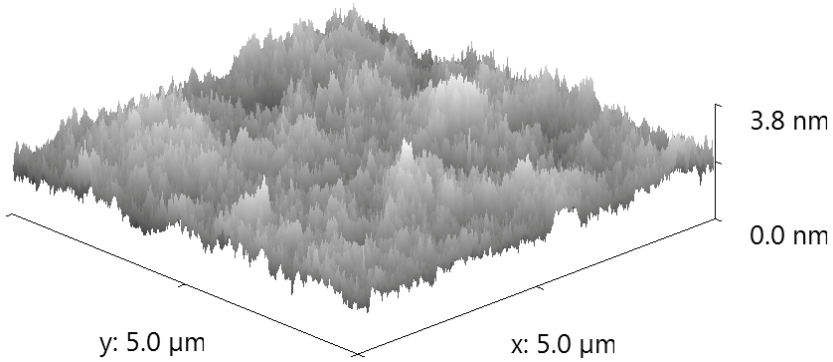
3.8 nm
0.0 nm
y: 5.0 µm
x: 5.0 µm

(a)

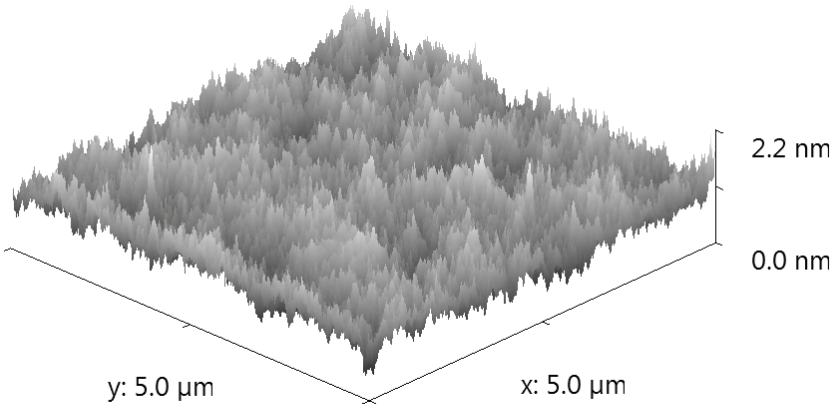
2.2 nm
0.0 nm
y: 5.0 µm
x: 5.0 µm

(b)

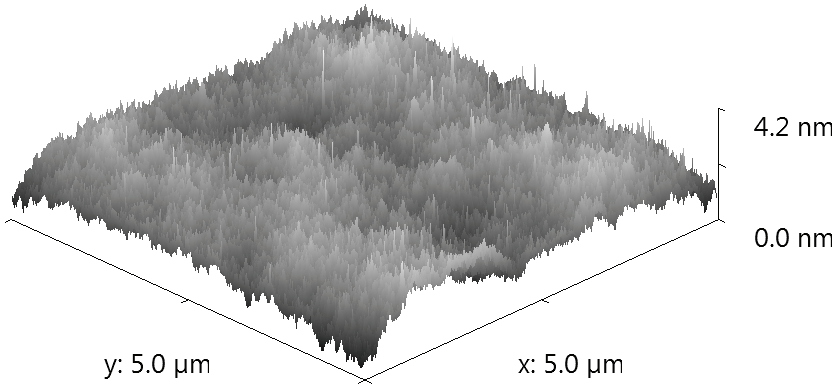
4.2 nm
0.0 nm
y: 5.0 µm
x: 5.0 µm

(c)

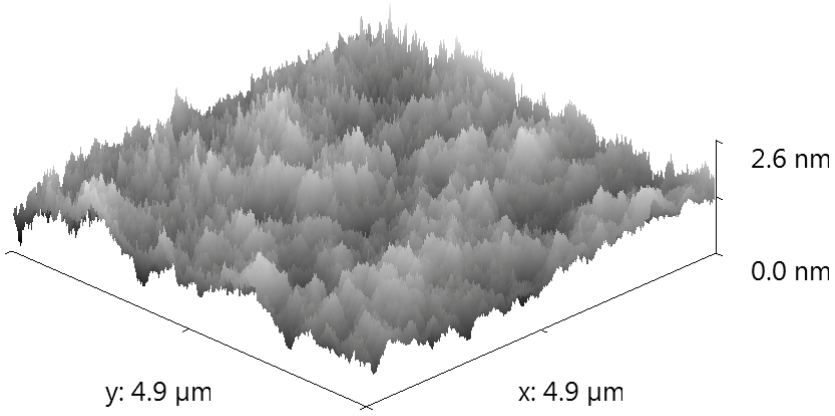

(d)

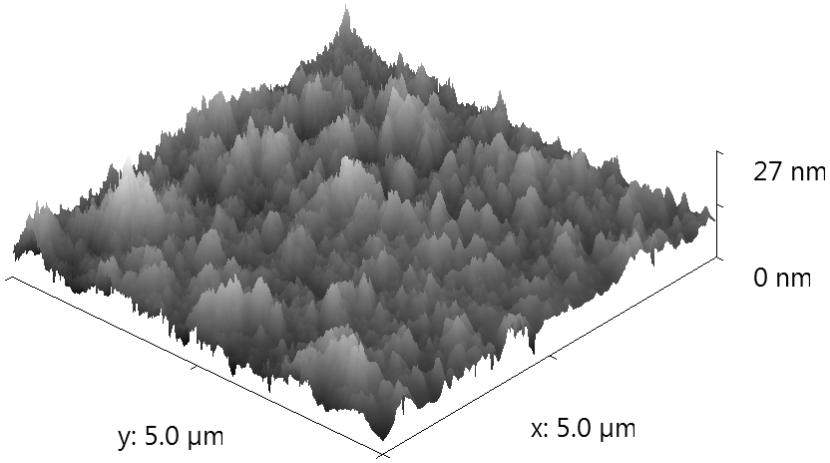

(e)

Figure 64.

TMAFM of 5 µm × 5µm images of (a) 1% wt. HPMC on PDMS silicone, (b) 1% wt. HPMC on silica, (c) 0.2% wt. HPMC on silica, (d) 1% wt. HPMC on the concave side of glass coated visor (e) 0.2% wt. HPMC on the concave side of glass coated visor. Notice the similarity of the topography of 1% wt. HPMC on all three substrates.

The roughness parameters in Table 17 demonstrate that the wavelength λ_a was reduced significantly with the HPMC cellulose film applied when compared to the bare substrate. The HPMC cellulose film on silica and PDMS silicone has a wavelength of 0.16 μm. The HPMC cellulose film on the Oakley visor glass coating has a wavelength of about 0.2 μm. With the exception of 0.2% wt. HPMC on visor glass coating, R_{RMS} converges to 0.2 nm to 0.3 nm.

Table 17.

Roughness parameters extracted from TMAFM for HPMC cellulose film on substrates of PDMS silicone, silica wafer, and glass coated polycarbonate visors provide by Oakley.

Surface Type	RMS Roughness		Average Wavelength		Average Slope	
	R_{RMS}^{film} (nm)	$\frac{R_{RMS}^{film}}{R_{RMS}^{substrate}}$	λ_a^{film} (μm)	$\frac{\lambda_a^{film}}{\lambda_a^{substrate}}$	Δ_a^{film}	$\frac{\Delta_a^{film}}{\Delta_a^{substrate}}$
1% wt. HPMC on PDMS Silicone	0.31 ± 0.01	0.08	0.16 ± 0.01	0.57	0.0098 ± 0.0004	0.15
1% wt. HPMC on Silica Wafer	0.192 ± 0.009	0.46	0.16 ± 0.02	0.72	0.0064 ± 0.0007	0.68
0.2% wt. HPMC on Silica Wafer	0.34 ± 0.04	0.81	0.16 ± 0.02	0.72	0.0110 ± 0.0007	1.17
1% wt. HPMC on Visor Concave Side	0.25 ± 0.02	0.22	0.19 ± 0.02	0.70	0.0069 ± 0.0007	0.34
0.2% wt. HPMC on Visor Concave Side	1.77 ± 0.01	1.55	0.21 ± 0.02	0.78	0.055 ± 0.005	2.74

Figure 60 in Chapter 7 which is the one dimensional PSDF shows the spatial distribution change with and without the HPMC cellulose adsorbates, and thus confirms the HPMC cellulose film alters the surface topography significantly.

Furthermore, three types of substrate have local peaks of spatial frequency around k = 20 μm^{-1} which corresponds λ_a = 0.3 μm without the HPMC cellulose film. Figure 65 focused in around the average spatial frequency at k = 40 μm^{-1} which corresponds to λ_a = 0.16 μm with the HPMC cellulose film made with 1% wt. gel. It is obvious where the local peaks of frequency distribution are observed.

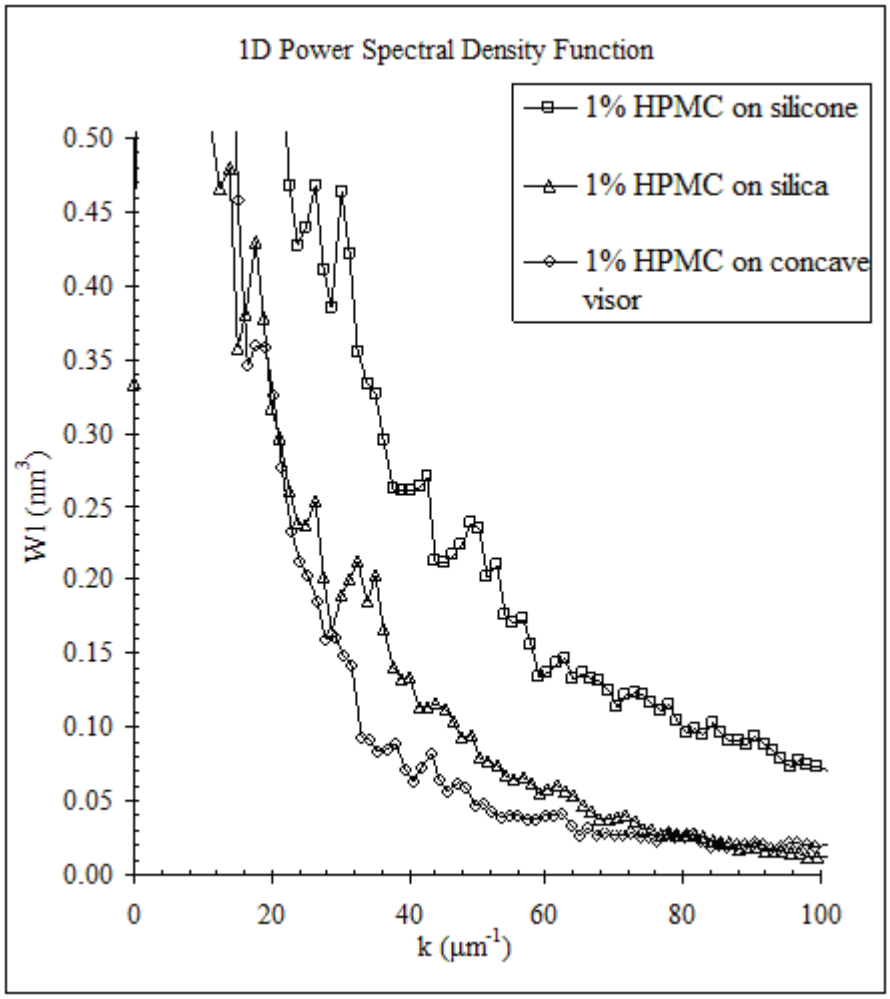

Figure 65.

One dimensional PSDF of HPMC cellulose film made with 1% wt. gel, on substrates of silica (triangles), PDMS silicone (squares), and the glass coated visor (diamond).

R_{RMS} , at the nanoscale level, will provide ample nucleation sites, which induces rapid condensation. The combined topography of the aforementioned characteristics leads to a rapid condensation which is immediately followed by coalescence, and the subsequent elimination of the fogging. The condensation layer rapidly forms a complete wetting layer as shown in Figure 66 and Figure 67.

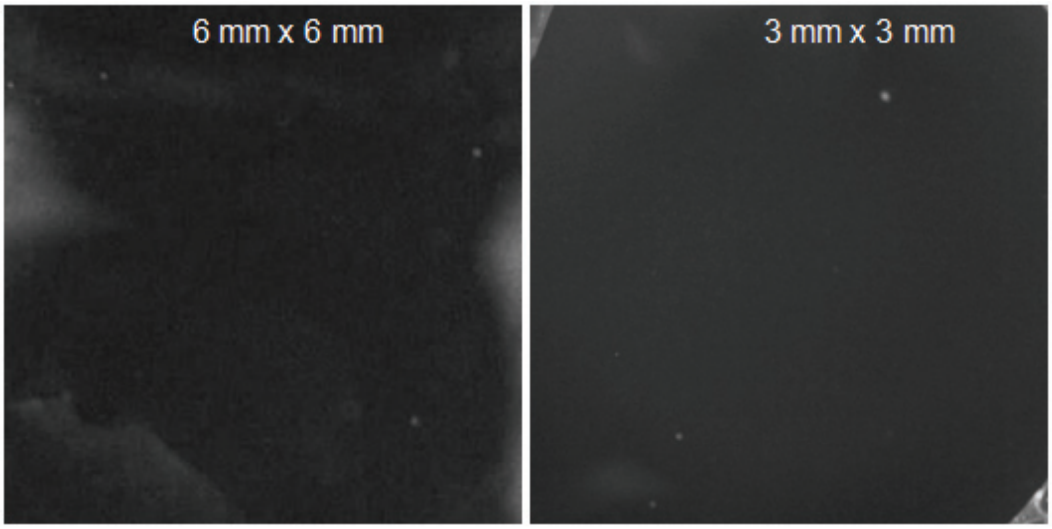

(a) (b)

Figure 66.

Condensation test. The water temperature is 70 °C. (a) HPMC cellulose 1% wt. gel coated silica over the hot water. (b) HPMC 1% wt. gel coated PDMS silicone over the hot water. The HPMC cellulose coating allows for a complete wetting layer to form evenly over the sample and remains optically clear after 30 minutes.

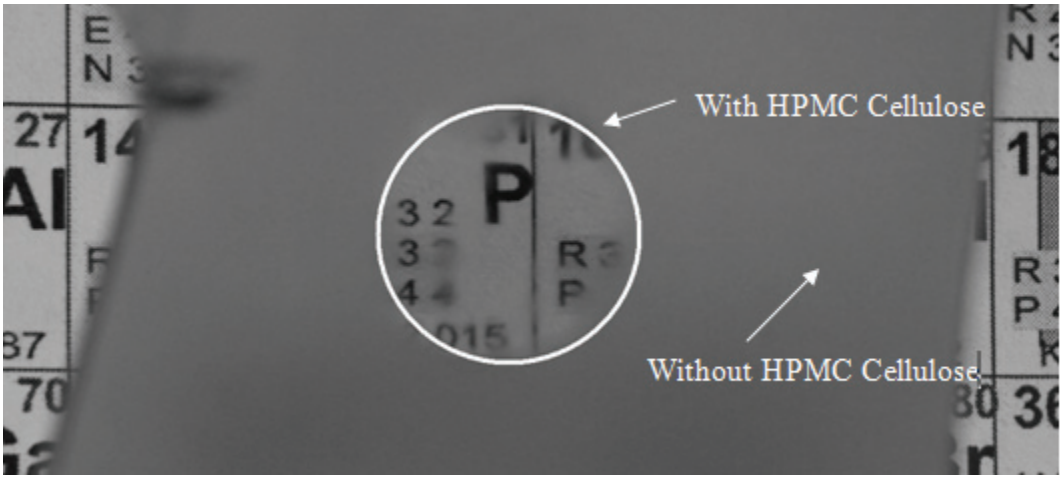

Figure 67.

Combination: HPMC cellulose 1% wt. gel coated glass coated polycarbonate in the center, with no coating outside of the white circle outline. The condensation behavior on the HPMC cellulose film differs when compared to the non-polymer film area, with the HPMC cellulose coated area removing any fogging, while surrounding the white outlined circle is precipitous fogging.

8.3 IBMM of PDMS silicone Surface

8.3.1 Polymer Structural Change of PDMS Silicone during IBMM Characterized by IBA

Figure 33 shows the change in the amount of PDMS silicone surface oxygen during nuclear resonance scattering, via the resonated oxygen signals as a function of the flux of the ion beam. The loss of oxygen is significant and occurs rapidly, and at an incident flux of 22 $\mu C/mm^2$, the amount of oxygen is reduced by more than 80%. This rapid loss of oxygen is due to the oxygen's highly electronegative characteristic coupled with being ionized by the He^{++} [142]. As the PDMS silicone backbone is composed of alternating silicon and oxygen atoms,

the He^{++} are effectively ionizing the oxygen in the PDMS silicone backbone and breaking these PDMS silicone chains into smaller chains as shown in Figure 68.

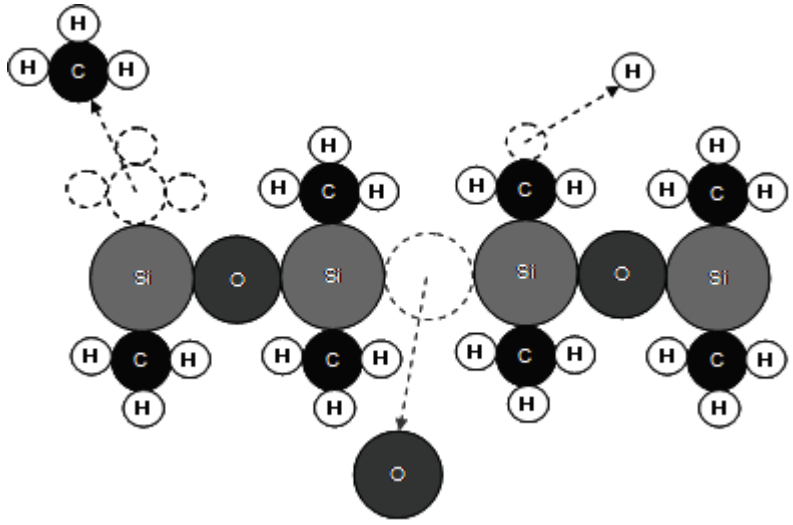

Figure 68.

IBMM of PDMS silicone polymer chain. Severe loss of oxygen breaks the backbone chain of the alternating –Si–O–Si–O– chain, cuts the chain shorter.

Figure 34 shows a loss in carbon is initially observed but the loss rate decreases and stabilizes near 10 μC/mm^2 He^{++} flux, with roughly half of the surface carbon being lost. Subsequent ion beam impingement results in no further carbon loss. As carbon exists in the form of the CH_3 radical attached to the silicon atom, loss of carbon does not break the polymer chain, but instead removes the CH_3 radical.

On the PDMS silicone IOL, ERD was used to determine the ion beam's effect on hydrogen. Figure 69 shows consecutive ERD of hydrogen spectra taken on the same PDMS silicone lens sample. Note that for each sequential spectrum taken, it demonstrates that the PDMS silicone lens experienced a loss of hydrogen at a comparable amount. This occurs throughout the entire depth profiling and is

not limited to just the surface. Figure 70 quantifies the hydrogen count from ERD, with hydrogen loss increase occurring in PDMS silicone lenses being proportional to the He^{++} flux.

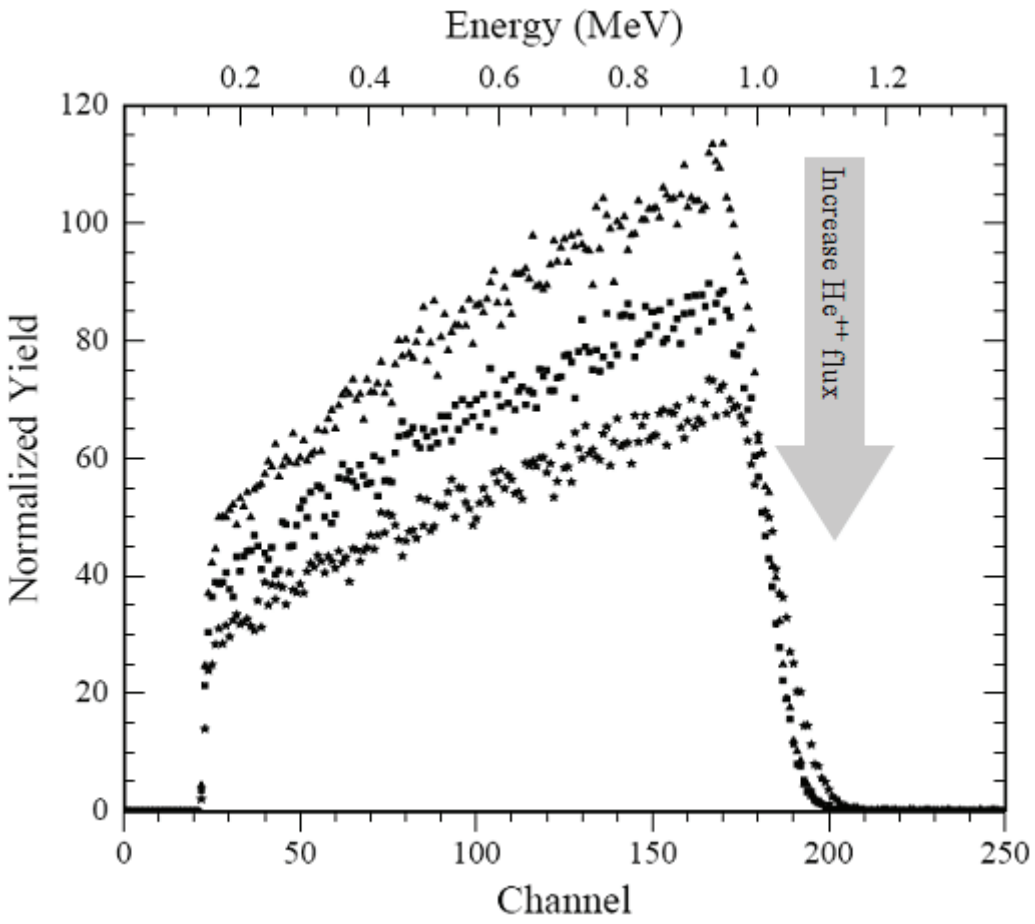

Figure 69.

Consecutive ERD spectrum (using He^{++}) obtained on PDMS silicone every 1.15 $\mu C/mm^2$ He^{++} flux. Notice that with each consecutive spectrum, proceeding from the dark line to the light line, the amount of H yield decreases proportionally throughout the PDMS silicone, not just at the surface.

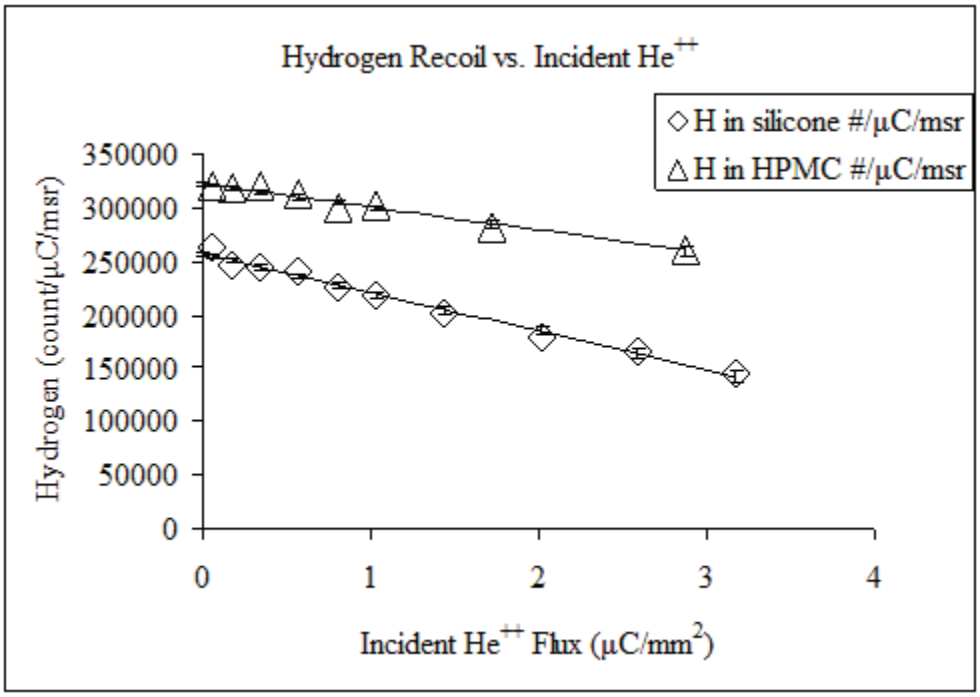

Figure 70.

ERD of hydrogen count of IBMM using HPMC cellulose 1% wt. film on silica and PDMS silicone. As He^{++} flux increases, showing the loss of hydrogen is proportional to the He^{++} flux.

The initial carbon and oxygen surface counts can be extrapolated back to zero ion beam flux via the y-intercept with the x-axis, and can be combined with the He^{++} ERD of hydrogen counts, which allows for a calculation of the stoichiometry to be conducted. Surface silicon need not be extrapolated, but is used to normalize the carbon and oxygen spectra. The surface composition via calculation is $N_{Si} : N_O : N_C : N_H = 1.00 : (0.85 \pm 0.16) : (1.80 \pm 0.25) : (3.50 \pm 0.05)$ with $N_{Si} : N_O$ being close to 1:1 and $N_{Si} : N_C$ close to 1:2 which is the composition of the PDMS silicone polymer chain backbone. However, hydrogen

is lower than the stoichiometric ratio, and it is suspected that the hydrogen loss is due to ion beam damage as shown in Figure 69.

8.3.2 Surface Topography Change of PDMS Silicone during IBMM

Looking at the TMAFM images in Figure 71, Figure 71(a) shows the PDMS silicone surface topography before IBMM, while Figure 71(b) shows a distinct hole, crater type surface topography experienced on the PDMS silicone surface and is due to IBMM. After IBMM, the PDMS silicone surface regarding the larger features with spatial distribution $k < 10$ μm^{-1} is flattened (see Figure 61). On the other hand, the smaller features with spatial distribution $k > 30$ μm^{-1} become more significant. Furthermore, Figure 72 focused in around spatial frequency k from10 μm^{-1} to 100 μm^{-1}. It is obvious that many local peaks of frequency distribution occur between 20 μm^{-1} to 80 μm^{-1} which correspond to λ_a between 0.08 μm to 0.31 μm. However, overall λ_a is around 0.249 μm, which is not enough to stop fogging during condensation.

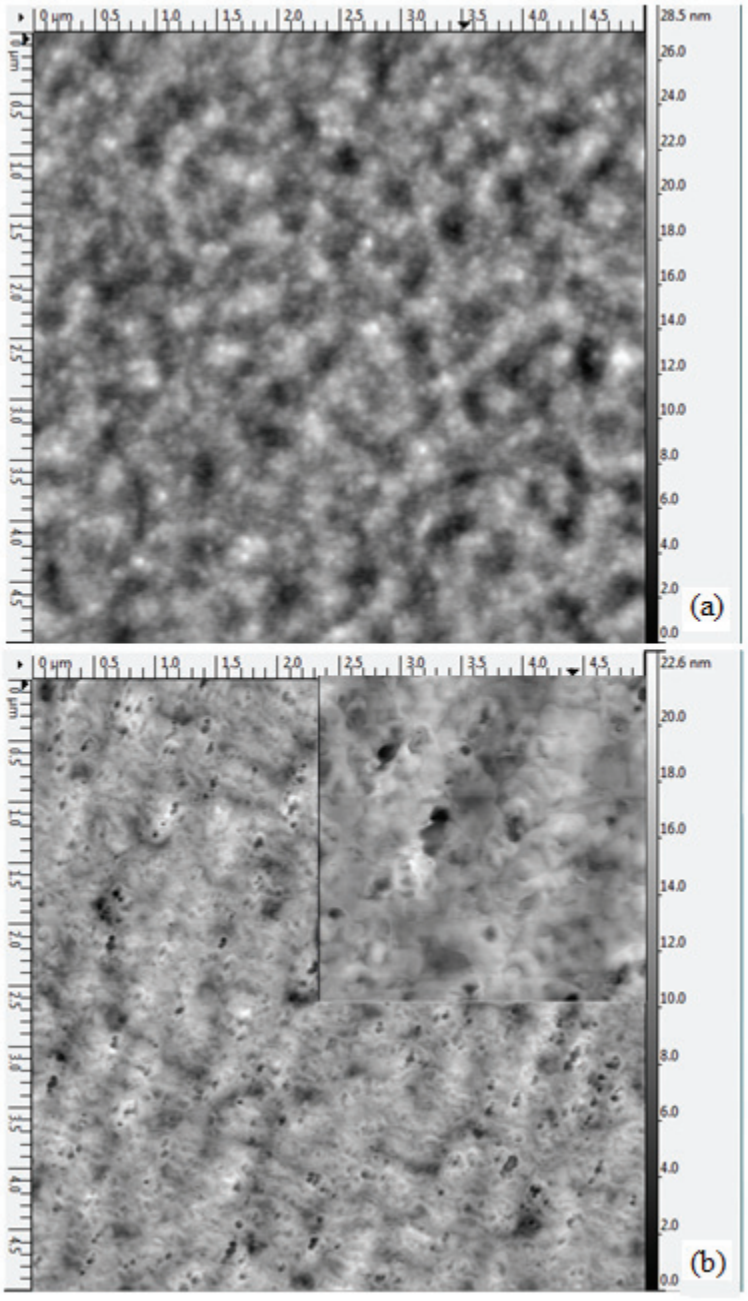

Figure 71.

AFM images of PDMS silicone polymer (a) before and (b) after IBMM. A distinct topographical change has taken place after IBMM, as noted by the hole and crater type features in (b) after 2.8 MeV He^{++} flux of 3 $\mu C/mm^2$, and the insert at the upper right corner is a 5 time enlargement of that area.

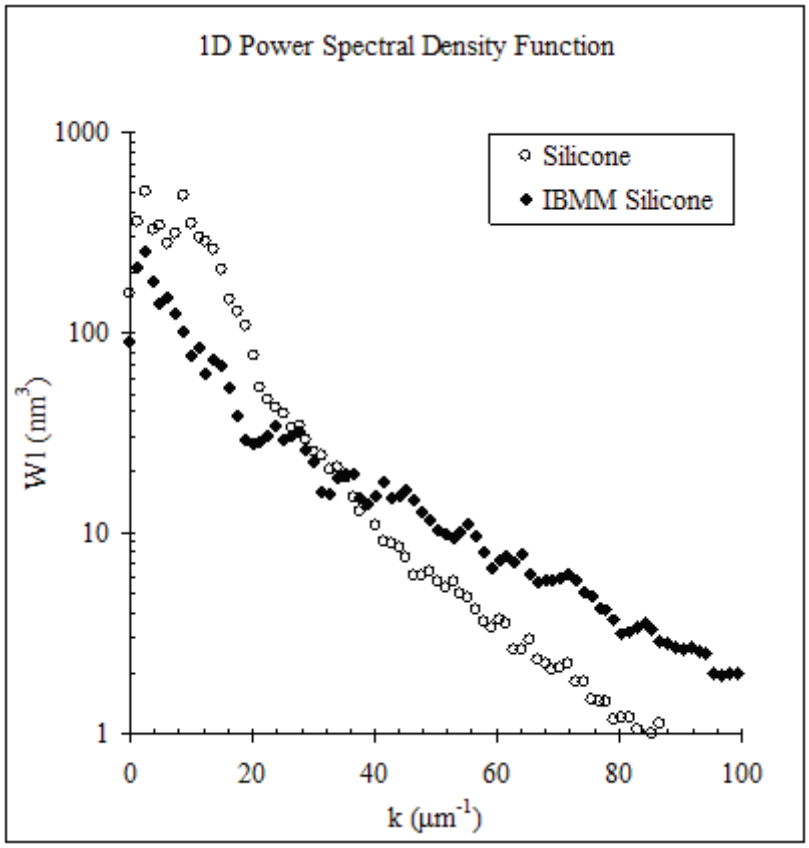

Figure 72.

One dimensional PSDF of PDMS silicone polymer before and after IBMM. Note the smoothness of the PSDF before IBMM. After IBMM is conducted, various frequency peaks become apparent where k is between 20 μm^{-1} and 80 μm^{-1} after 2.8 MeV He^{++} flux of 3 $\mu C/mm^2$.

8.3.3 Water Affinity and SFE Changes of PDMS Silicone during IBMM

The Sessile drop method measured how the ion beam exposure increased the water affinity of the PDMS silicone surface. The contact angle using water droplets was reduced from 104.7°, prior to IBMM, to 81.3° showing that the surface changed from hydrophobic to slightly hydrophilic. The contact angle and SFE change is shown in Table 18 and Table 19 after 2.8 MeV He^{++} flux of 3

$\mu C/mm^2$. This SFE change can be interpreted as a result of the loss of oxygen and CH_3 radicals due to interactions with the He^{++} beam.

Table 18.

Contact angle measured for each of the three test liquids on PDMS silicone before and after IBMM.

Surface Material	Contact Angle with Water $\theta°$	Contact Angle with Glycerin $\theta°$	Contact Angle with α-Bromonaphthalene $\theta°$
PDMS silicone	104.7 ± 1.4	-	-
PDMS silicone with IBMM	81.3 ± 2.6	82.8 ± 1.4	51.5 ± 2.9

Table 19.

SFE of PDMS silicone before and after IBMM.

Surface Material	Total SFE γ^{Total} (mJ/m^2)	LW Component of SFE γ^{LW} (mJ/m^2)	Base Component of SFE γ^- (mJ/m^2)	Acid Component of SFE γ^+ (mJ/m^2)
PDMS Silicone	20.2 [123]	19.4 [123]	0.8 ($\gamma^{polar} = 2\sqrt{\gamma^+\gamma^-}$) [123]	
PDMS Silicone with IBMM	31.5	29.2	13.4	0.1

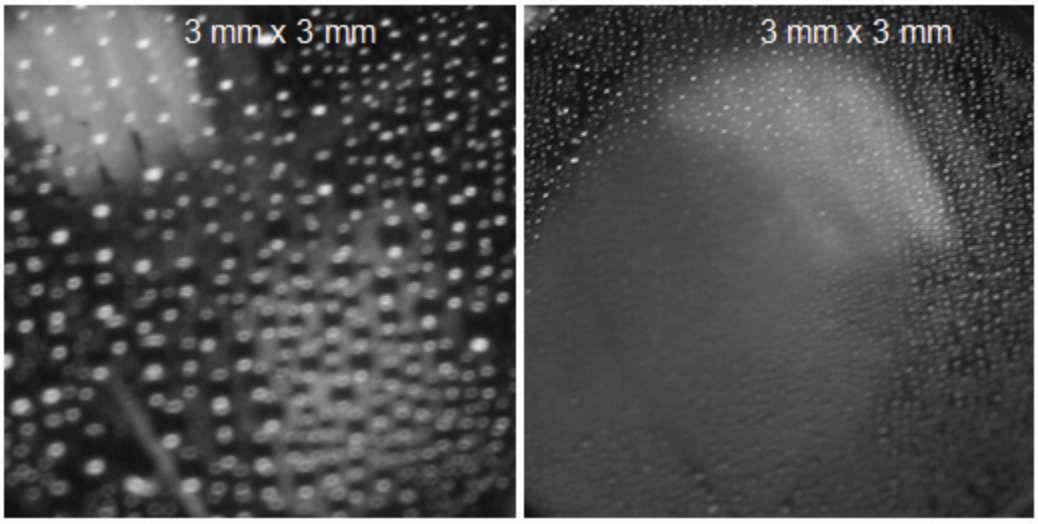

(a) (b)

Figure 73.

Condensation test of PDMS silicone after IBMM. The water temperature is 70 °C. (a) 3 seconds after IBMM of PDMS silicone is placed over the hot water. (b) 90 seconds after IBMM of PDMS silicone placement. The SFE has increased when compared to non IBMM PDMS silicone, since we now see much more coalescence on the IBMM PDMS silicone than on the PDMS silicone experiencing no IBMM (Figure 63(c) and (d)).

Another indication that the PDMS silicone SFE has changed is that the water condensation and coalescence behavior changes when the PDMS silicone experiences IBMM. Figure 73 shows water condensing and coalescing after the PDMS silicone was exposed to the ion beam rather than forming isolated water beads prior to IBMM as Figure 63(c) and Figure 63(d) show. Note that the water temperature and time elapse from the PDMS silicone's initial exposure to the

fogging conditions is the same for Figure 63(c) and Figure 73(a), at 3 seconds, and Figure 63(d) and Figure 73(b) at 90 seconds.

8.4 IBMM of HPMC Cellulose Film

8.4.1 Polymer Structural Change of HPMC Cellulose during IBMM Characterized by IBA

HPMC cellulose films were applied to the PDMS silicone substrates and quartz silica substrates using similar techniques as described above. IBA was used to examine the composition and modification via IBMM. However, the results were quite different. Figure 29 and Figure 30 of Chapter 4 show the nuclear resonance scattering results of oxygen and carbon yield change as a result of the ion beam flux. The silicon substrate silicon signal height is observed to be stable, so it is chosen to normalize the oxygen and carbon signals to ensure the comparability from spectrum to spectrum. However, because of the HPMC cellulose film on the substrate, the beam energy at the substrate is less compared to the incident He^{++} at the film surface. The cross section σ at the substrate is larger than that of the HPMC cellulose film at the surface. Therefore, the Si signal height is slightly larger than expected. However, considering the energy range (3 MeV to 4.3 MeV) combined with the areal density of the film (10^{18} atom/cm^2 to 10^{19} atom/cm^2) and the substrate type, this effect is only a few percent and makes this effect small when calculated. As shown in Figure 29 of Chapter 4, loss of oxygen is again significant and occurs rapidly, and at an incident flux of 30 μC/mm^2, the amount of oxygen was reduced by about 80% due to the high electro negativity of the oxygen atom. However, Figure 30 shows the change of surface

carbon as slightly linear and increasing rather than experiencing an initial loss as the carbon in bare PDMS silicone experienced. This behavior is likely due to the combination of the lack of rigidness of the HPMC chain and the rapid loss of oxygen atoms which effectively concentrates the carbon near to the surface and therefore shows an increase in the carbon signal.

ERD was used on the HPMC cellulose film to determine the ion beam's effect on hydrogen. Figure 74 shows consecutive ERD of hydrogen spectra taken on the same HPMC cellulose film on the silica base. Figure 70 quantifies the hydrogen count using ERD, with hydrogen loss occurring in the HPMC cellulose film showing the loss of hydrogen as proportional to the He^{++} flux. Note that for each sequential spectrum taken, the amount of hydrogen decreases for the lower energy portion of the spectrum, but there is minimal change at the high energy part of the spectrum, which indicates that the HPMC cellulose film experiences a loss of hydrogen not at the surface, but instead from within the film and towards the substrate. This behavior also seems to be in agreement with the effect of the rapid oxygen loss at the surface which equivalently increases hydrogen closer to the surface. Deeper within the film, where HPMC keeps its oxygen, the loss of hydrogen is more obvious. However, this behavior cannot be fully explained and understood until the depth profiling of carbon and oxygen is also researched, and remains a future goal and experiment. This behavior also provides the foundation that measuring the surface hydrogen composition is not impacted by ion beam damage. The study of IBMM of the HPMC cellulose film shows it is possible to take IBA measurements of polymers which are easily damaged during IBA.

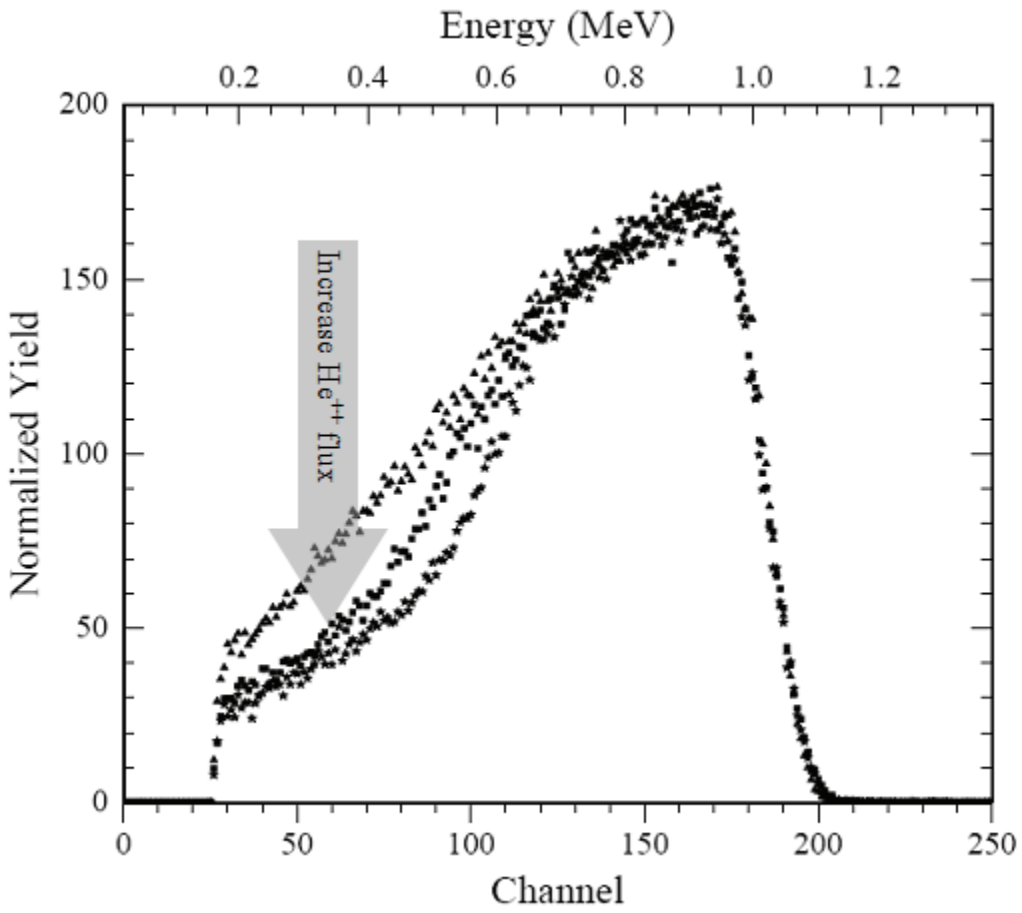

Figure 74.

Consecutive ERD spectrum of HPMC cellulose 1% wt. film on silica at 1.15 $\mu C/mm^2$ He^{++} flux intervals, emulating IBMM. Notice that at the surface of the film (at the highest He^{++} incident energy), there is no loss of H, but as HPMC cellulose 1% wt. film is penetrated, H loss begins to occur and grow proportionally.

8.4.2 Surface Topography Change of HPMC Cellulose during IBMM

The HPMC topography as measured by TMAFM changed slightly from pre IBMM to post IBMM by indicating a slight increase in roughness and slight dimpling, but much less obvious than that experienced by the PDMS silicone

polymer chain (see Figure 75). After IBMM, the HPMC cellulose surface regarding the spatial distribution k ranging from 20 μm^{-1} to 200 μm^{-1} (see Figure 61). Furthermore, Figure 76 zoomed in around spatial frequency around above mentioned k range which corresponds to λ_a ranging between 0.03 μm and 0.31 μm.

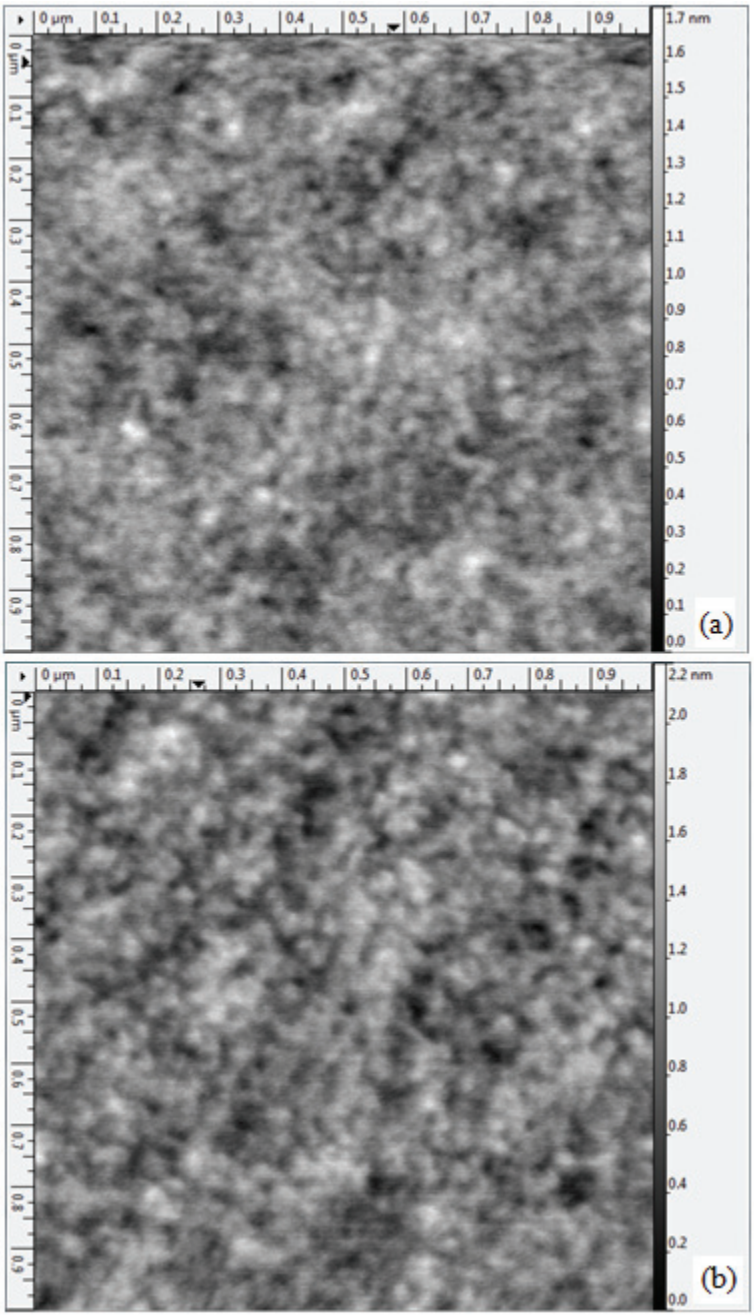

Figure 75.

TMAFM images of HPMC cellulose 1% wt. film on silica (a) before and (b) after IBMM. The topography change initiated by IBMM is still apparent with the observed slight increase in dark dimpling after 2.8 MeV He^{++} flux of 3 $\mu C/mm^2$.

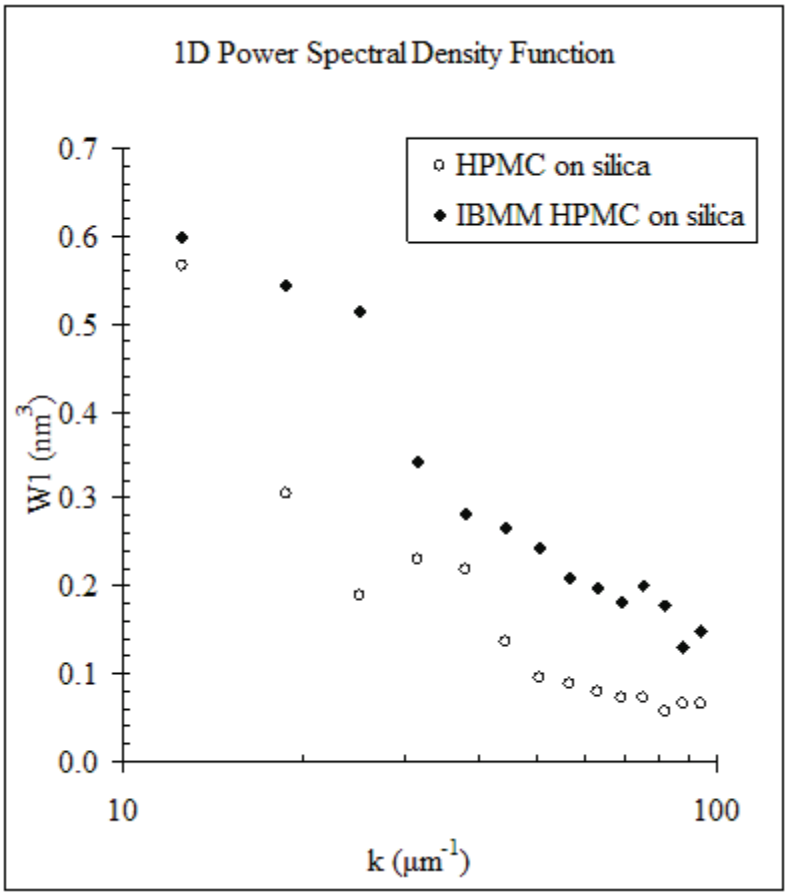

Figure 76.

One dimensional PSDF of the HPMC cellulose 1% wt. film on silica before and after IBMM. Again, we see a more distinct k distinguishable between 20 μm^{-1} to 100 μm^{-1}.

8.5 IBMM of Si(100)-SiO_2 Interphase

8.5.1 Surface Order Disruption of Si(100)-SiO_2 Interphase during IBMM

As shown in Figure 77, the passivated sample's channeling oxygen areal density along the <111> direction was extrapolated to 1.4×10^{15} atom/cm^2 at zero ion incidence, which is less than the rotating random oxygen areal density which was extrapolated to 2.1×10^{15} atom/cm^2 via nuclear resonance scattering,

indicating an ordering of the oxygen atoms. As the He^{++} incident flux increases, the channeling oxygen areal density increases and ultimately converges to that of the rotating random oxygen areal density, indicating that any ordering that was initially present has since been disrupted. When the He^{++} flux reaches 55 $\mu C/mm^2$, both rotating random and channeled yields are no longer distinguishable from each other, indicating that the ordering of oxygen has disappeared. Similarly, Si surface peak measurements taken elsewhere of channeling in the <111> and <100> directions have resulting spectra which also experience an uptrend in oxygen areal density as the He^{++} beam flux increased [24]. Both of these results support the conclusion that the ordered Si(100)-SiO_2 interphase will eventually become amorphous as the He^{++} flux increases beyond the point where the channeling and rotating random oxygen areal density convergence.

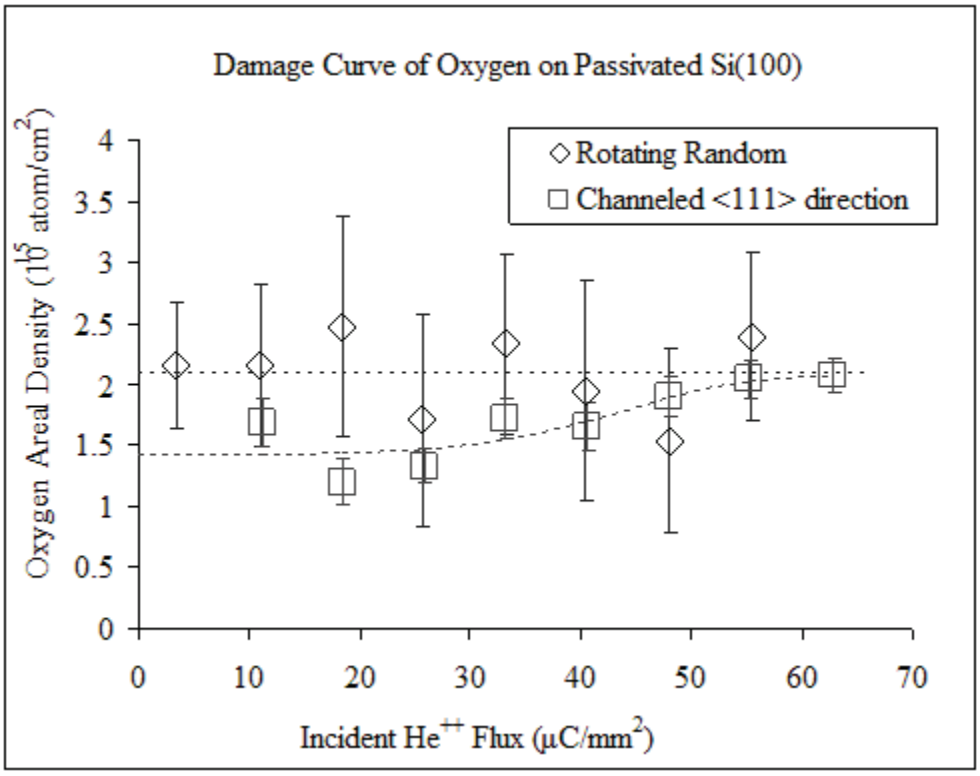

Figure 77.

Damage curve of Oxygen on passivated Si(100). The top curve represents the oxygen areal density collected during the rotating random, the goal of which is to randomize the orientation of the crystalline Si(100) sample so as to not align the beam to any one of the crystalline axes. The bottom curve represents the oxygen areal density collected while channeled in the <111> direction; the goal of which is to align the ion beam to the Si(100) <111> crystalline axis. The ordering of the silicon surface is initially apparent, as the oxygen areal density is initially less than the oxygen areal density of the Rotating Random. As the incident flux of He^{++} increases, the oxygen areal density of the <111> direction converges with the Rotating Random oxygen areal density, which occurs at 55 μC/mm^2. Raw data from [24].

8.5.2 SFE Convergence of Si(100)-SiO_2 Interphase during IBMM

Table 20 and Table 21 show that the passivated Si(100) surfaces (Passivation-Sample and Anneal-Sample) have less water affinity than the as-received control samples (As-Received) after He^{++} flux of about 55 $\mu C/mm^2$. One can attribute this behavior to the SFE and intermolecular interaction between water molecules and solid surfaces [17, 66]. Since passivated surfaces have lower SFE, interaction between water molecules and the sample surface is smaller, therefore the water affinity is also smaller compared to the as-received control samples. The As-Received sample possessed the highest total SFE and therefore was the most hydrophilic of the three pre-IBMM samples. This high SFE is due to the native oxide which was allowed to grow and other possible contaminants which may have settled on the surface together with dangling bonds. From Table 20 and Table 21, the contact angle measurements and resultant SFE measurement of 57.3 mJ/m^2 validates this assessment. Passivation-Sample underwent the Herbots-Atluri clean. Due to the cleaning and passivating process, Passivation-Sample's surface is more inert than that of sample As-Received, and Passivation-Sample's SFE is thus considerably lower, at 38.7 mJ/m^2. As the contact angle analysis shows, the surface of Passivation-Sample is not nearly as hydrophilic in nature as the As-Received sample. Finally, Anneal-Sample underwent the same Herbots-Atluri clean treatment as Passivation-Sample, but then was annealed for 24 hours at 200 °C. An anneal has the effect of removing or smoothening out defects that may be present in the bulk or at the surface [143]. As defects on the surface are being removed, this further passivates the surface and renders it more

inert. Referring to Table 21, Anneal-Sample had the lowest total SFE of all the samples and was equal to 26.0 mJ/m^2. Contact angle analysis indicates that Anneal-Sample is hydrophobic.

Furthermore, referring again to Table 20, the Anneal-Sample is the only sample in the entire group that has minimal contributions from both Lewis acid and Lewis base SFE components, and thus its total SFE is completely dominated by the LW SFE component. Also of note is the Anneal-Sample's LW SFE component relative to all of the other samples' LW SFE components, which is significantly lower; 25.5 mJ/m^2 compared to 31.3 mJ/m^2 for the Passivated-Sample and at least 40 mJ/m^2 for the other samples. As this sample, Anneal-Sample, has undergone a 24 hour, 200 °C anneal, we can now observe the importance of the anneal process in regards to generating an inert, low defect free surface through observing the sample's SFE components.

Table 20.

Contact angles of Si(100) before and after IBMM.

Type of Si(100)	Contact Angle with Water $\theta°$	Contact Angle with Glycerin $\theta°$	Contact Angle with α-Bromonaphthalene $\theta°$
As-Received	38.0 ± 0.8	31.3 ± 0.5	19.9 ± 0.5
Passivation-Sample	69.3 ± 0.5	60.9 ± 0.6	47.1 ± 0.8
Anneal-Sample	100.2 ± 0.7	91.9 ± 0.4	58.9 ± 0.6
As-Received-1 with IBMM	79.4 ± 0.6	77.7 ± 0.8	22.7 ± 0.5
As-Received-2 with IBMM	80.2 ± 1.1	77.6 ± 1.0	24.2 ± 0.4
Passivation-Sample-1 with IBMM	75.0 ± 1.1	75.0 ± 0.9	23.6 ± 0.9
Anneal-Sample-1 with IBMM	69.1 ± 0.7	72.4 ± 0.7	29.3 ± 1.0

Table 21.

SFE of Si(100) before and after IBMM.

Type of Si(100)	Total SFE γ^{Total} (mJ/m^2)	LW Component of SFE γ^{LW} (mJ/m^2)	Base Component of SFE γ^- (mJ/m^2)	Acid Component of SFE γ^+ (mJ/m^2)
As-Received	57.3	41.8 ± 0.5	30.1 ± 3.4	2.0 ± 0.4
Passivation-Sample	38.7	31.3 ± 1.3	12.5 ± 2.5	1.1 ± 0.5
Anneal-Sample	26.0	25.5 ± 1.3	2.1 ± 1.4	0.03 ± 0.09
As-Received-1 with IBMM	45.4	41.0 ± 0.4	10.8 ± 1.9	0.4 ± 0.2
As-Received-2 with IBMM	44.3	40.6 ± 0.3	9.9 ± 3.1	0.4 ± 0.3
Passivation-Sample-1 with IBMM	45.1	40.8 ± 0.7	14.0 ± 4.4	0.3 ± 0.3
Anneal-Sample-1 with IBMM	43.1	38.9 ± 1.0	20.0 ± 3.5	0.2 ± 0.2

After IBMM, the SFE of sample As-Received-1 decreased from 57.3 mJ/m^2 to 45.4 mJ/m^2 while the SFE of the passivated wafer sample Passivation-Sample-1 and the Anneal-Sample increased from 38.7 mJ/m^2 to 45.1 mJ/m^2 and from 26.0 mJ/m^2 to 43.1 mJ/m^2, respectively. According to Van Oss, the LW component of the surface tension relates to the long range dispersion, apolar force between the water molecule and the surface while the Lewis acid base component relates to the strength of the polar electro-chemical bonding when interacting with

water [144]. Thus, changing the Lewis acid base components of the SFE is equivalent to changing the surface's electro-chemical properties.

Table 22 is a combination of Table 3 and Table 4 from Chapter 4. The observation of the SFE behavior did not correlate to hydrocarbon contamination in this case. The as-received control sample #1 (As-Received-1) and the as-received control sample #2 (As-Received-2) have significantly different carbon areal densities after IBMM (see Table 22), but possess the same SFE as shown in Table 21. On the other hand, the hydrogen areal density remains similar on all samples prior to IBMM, while the SFE and water affinity vary widely. After IBMM, the hydrogen areal density of sample As-Received-1 and sample Anneal-Sample-1 increased in an almost parallel manner with each other with increasing He^{++} ion beam flux, as shown in Figure 78, while the SFE of As-Received-1 decreased and Anneal-Sample-1 SFE increased. This behavior indicates that the increase in hydrogen is not correlated to the change of the SFE.

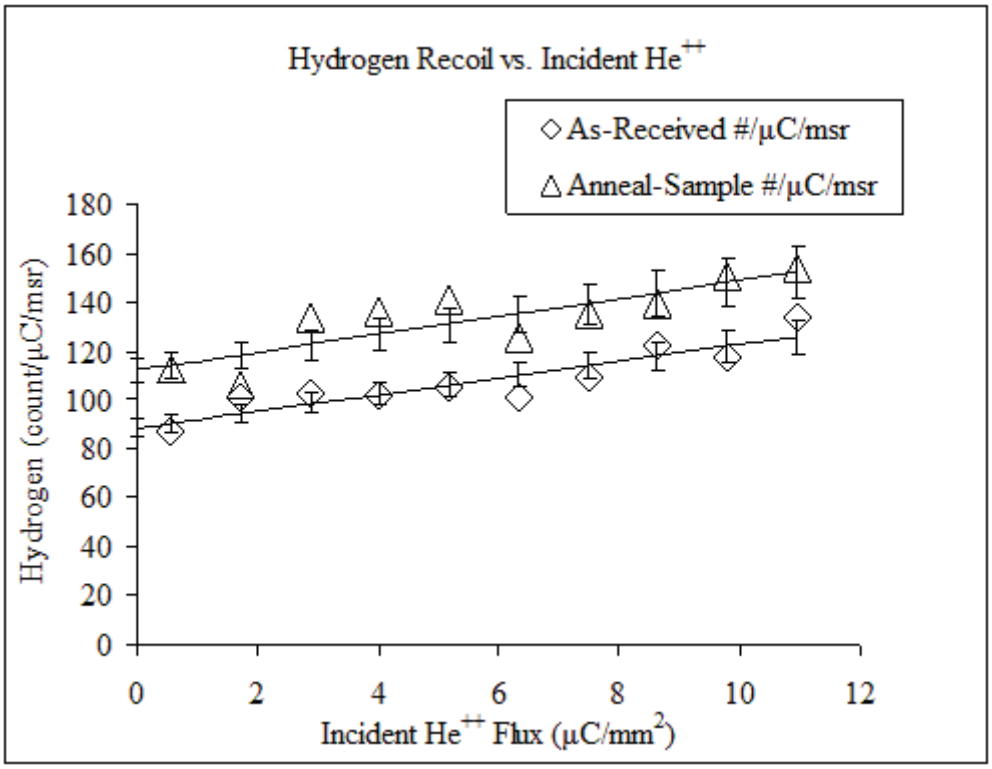

Figure 78.

Hydrogen count detected via ERD versus He^{++} ion beam flux. Both sample As-Received and Anneal-Sample have increasing hydrogen areal density with increasing incident He^{++} flux, indicating damage is being done to the ordered structure of which hydrogen is a part of. The uncertainty is obtained from error propagation of linear regression modeling uncertainties.

Table 22.

Areal densities of silicon, oxygen, carbon were obtained via channeling along the <100> axis at 2 MeV, 3.045 MeV, and 4.265 MeV (respectively), and calibrated using the rotating random silicon signal height. Hydrogen areal density was obtained using ERD at 2.8 MeV analyzed utilizing RUMP.

Type of Si(100)	Si Surface Peak Areal Density (10^{15} atom/cm^2)	O Areal Density (10^{15} atom/cm^2)	C Areal Density (10^{15} atom/cm^2)	H Areal Density (10^{15} atom/cm^2)
As-Received-1 with IBMM	-	7.196	7.300	-
As-Received-2 with IBMM	16.366	4.659	2.190	-
Passivation-Sample-1 with IBMM	17.686	3.025	4.010	-
Anneal-Sample-1 with IBMM	15.426	4.300	2.434	-
As-Received-3	-	-	-	5.0
Passivation-Sample-2	-	-	-	4.4
Anneal-Sample-2	-	-	-	4.0

CHAPTER 9

CONCLUSION

9.1 Understanding of the Water Affinity, Nucleation, and Condensation on Si-based Surfaces

Water affinity of Si-based surfaces is quantified via contact angle measurement using the Sessile drop method and the determination of the SFE using three different test liquids coupled with the Van Oss theory and the Young Dupré equation. Water affinity and SFE explain the water condensation and nucleation pattern. First, we demonstrated that the contact angle measurement and determination of SFE agrees with existing publications on quartz silica and PDMS silicone. We then correlated the observed condensation pattern of glass coated polycarbonate visors provided by Oakley to the water affinity characterization via contact angles and SFE from this work. It was henceforth shown that for a hydrophobic surface with lower SFE, the condensation pattern forms isolated water beads, while for a hydrophilic surface with higher SFE, the condensation pattern forms coalescing water puddles.

Surface topography analysis using TMAFM demonstrated that nanoscale capillary features expedite the condensation speed, and therefore confirmed that the Kelvin equation (Equation (1)) is applicable to the nucleation of the water droplets at the nanoscale level. The surface topographical roughness parameters, root mean square of roughness, average wavelength, and average slope representing the rate of change in the height of the surface peak vs. the distance along the surface, can be used to predict the speed of nucleation and condensation.

Surfaces with an average wavelength of more than 200 nm exhibit initial fogging while an average wavelength of less than 200 nm allows for wetting without fogging during condensation.

9.2 Controlling the Water Affinity, Nucleation, and Condensation on Si-based Surfaces via Polymer Adsorbates

HPMC cellulose adsorption on Si-based surfaces forms a thin film that changes the SFE and morphology of the respective surface, resulting in a change in behavior of the water condensation. We achieved this by understanding that water condensation will dominate evaporation as long as the vapor pressure in the surrounding gaseous environment exceeds the saturation vapor pressure. Therefore, instead of attempting to prevent water condensation, we took a different approach which was to lead the condensation pattern to complete wetting to eliminate fogging, thus resolving the problem during retinal surgeries which was confirmed by collaborating ophthalmologists and successful experiments conducted on artificial eyes.

Our approach to optimize an HPMC cellulose film layer for the purpose to suppress fogging is systematically summarized. First, HPMC cellulose film is characterized by RBS via incident ion (He^{++}) energy loss. The correlation of HPMC cellulose film with an areal density between 10^{18} atom/cm^2 to 10^{19} atom/cm^2 is a working range to control fogging during water nucleation and condensation. The same areal density is also shown to be the result of using a HPMC cellulose gel in concentrations ranging from 0.2% wt. to 1% wt. during

HPMC cellulose adsorption on Si-based surfaces such as silica, PDMS silicone, and glass coated polycarbonate visors.

Second, 4.265 MeV $^{12}C(\alpha, \alpha)^{12}C$ and 3.045 MeV $^{16}O(\alpha, \alpha)^{16}O$ nuclear resonance scattering, and 2.8 MeV He^{++} ERD of hydrogen confirmed that the HPMC cellulose surface composition maintains the bulk stoichiometric ratio of $C_{32}H_{60}O_{19}$ and explained the high water affinity and SFE on the HPMC cellulose film.

Next, TMAFM analysis of the HPMC cellulose film was correlated to the resulting change in behavior of water condensation and the formation of a wetting layer on the HPMC cellulose surface. Regardless of the different types of Si-based substrates used (silica, PDMS silicone, or glass coated polycarbonate visor provided by Oakley), the HPMC cellulose film shows a similar, evenly distributed oscillating surface pattern much different than that of the substrate. A surface wavelength of 0.16 μm allows for the wetting layer to form during water nucleation and condensation without "fogging" and without impeding the original visual clarity of the substrate.

Finally, the differential PIXE method is used to characterize the areal density of carbon, oxygen, and hydrogen based polymers such as HPMC cellulose film on Si-based substrate for the first time. Areal density measurements using He^{++} PIXE was used to successfully characterize the HPMC cellulose film on Si based surfaces. The silicon substrate allowed for the generation of a reference spectrum based on incident He^{++} energy, which was then applied to the areal density determination. This concept extends the differential PIXE method and

demonstrates an agreement of results between RBS and PIXE, especially for uniform compound substrates such as the silica wafer.

9.3 IBMM of PDMS Silicone and HPMC Cellulose

IBMM of polymers, such as PDMS silicone, was explained via the loss of highly electro-negative oxygen and light weight, positive hydrogen atoms. First, the PDMS silicone polymer chain is shortened during IBMM by removing a large fraction of the oxygen through scission, which forms half of the Si–O backbone of the PDMS silicone chain. The CH_3 radical also experiences losses as observed in the amount decreases of carbon and hydrogen. The change of composition from the IBMM during IBA also gives insight into the modification of SFE due to a change in Lewis acid base SFE components via ionization, which in turn affects the water affinity. A surface morphology change is also observed during IBA, which further enabled us to explain the IBMM effects on water condensation and nucleation behavior.

We have also used IBA to study easily damaged polymers such as HPMC cellulose and PDMS silicone. By looking at the yield change of oxygen and carbon over the amount of ion beam flux on the sample, i.e. the damage curve, we have used extrapolation of the oxygen and carbon yield to zero ion beam flux to account for changes due to IBMM. The damage curve enables the use of IBA despite IBMM and we effectively characterized both HPMC cellulose and PDMS silicone accurately despite the damage these polymers experienced during the measurement process.

Furthermore, He^{++} ERD of hydrogen allows us to look at the hydrogen depth profiling of polymers such as PDMS silicone and HPMC cellulose, and their respective change over the incident ion flux was explored for the first time. Understanding the depth profiling change is essential: for PDMS silicone, loss of hydrogen occurs throughout the entire depth profiling and is not limited to just the surface. On the contrary, HPMC cellulose experiences a loss of hydrogen not at the surface, but instead from within the film and towards the substrate. This behavior provides the foundation that measuring the HPMC cellulose surface hydrogen composition will not be impacted by ion beam damage, unlike the PDMS silicone.

9.4 IBMM of Si(100)-SiO_2 Interphase

Through IBA we reaffirmed the existence of order at the Si(100)-SiO2 interface. Furthermore, through the process of IBMM, as the impinging ion beam flux increases, the order at this interface was found to be systematically disrupted and the order reduced until the areal density (of oxygen) of the ordered interface equaled the areal density of a rotating random data collection of a silicon oxide grown on silicon at a particular ion beam flux amount. Beyond this limit, the disruption of order did not continue to increase, but equaled that of an amorphous layer of silicon oxide.

We were able to consistently extract the SFE and its components using contact angle analysis on a variety of Si(100) samples, as-received, passivated, and annealed. Regardless of the initial SFE values of the three respective categories of samples noted above, the effect of the IBMM on the SFE was to

drive the SFE to a mid range value common to all samples. After IBMM, all samples had very similar, mid range SFE values which were neither truly hydrophobic nor hydrophilic. The contact angle analysis method is thus demonstrated to detect with good sensitivity the degree of initial ordering and passivation of the surface and how IBMM consistently modifies the surface water affinity and SFE to the same state irrespective of the initial surface passivation. This demonstrates that the initial surface preparation and reaction do not provide any resistance to modification from the ion beam to an unpassivated state. Another significant observation was that the Anneal-Sample's Lewis acid and Lewis base components of SFE were negligible compared to its LW component of SFE. It is essential to take this behavior into account in understanding the changes occurring at the surface during analysis and processing.

In summary, the present research is led by results, laboratory methods, observations and models of Si(100) and SiO_2 surfaces, where our research group has been modifying water affinity, surface topography and composition, and hydrophobic and hydrophilic properties for more than a decade. Using the results of the present work, both eye surgeons were able to modify the water affinity of such IOLs and inhibit condensation during retinal surgery by using the benign surface modification we developed in our laboratory after successfully reproducing their surgical conditions and solve their problems in our research laboratory. One patent application was filed and one patent was issued from the research discussed in this work [1, 3]. Three papers are in print, three oral

conference presentations, and three poster conference communications have been given [38, 95, 109].

9.5 Future Work

The understanding of water nucleation and condensation behavior vs. water affinity and SFE has many other potential industrial applications, controlling "fogging" of visionwear or where ever fogging becomes an issue. The exploration may include:

(a) Condensation wetting model surface limitations of 1) R_{RMS} under 0.25 nm remains uninvestigated, which is close to the water's R_{RMS} of 0.21 nm, 2) R_{RMS} above 1.5 nm is also uninvestigated, 3) tested on hydrophilic surfaces only, 4) surfaces with more than one oscillation frequency are more complex.

(b) Modifying SFE and surface morphology has many ways beyond polymer adsorption for further exploration.

The SFE study exposed us and prepared us for future studies of intermolecular interaction in general, which not just limited to water condensation behavior. SFE differentiation of Si(100)-SiO_2 interphase may open doors to understand semiconductor behavior at the Si(100)-SiO_2 interface (e.g. the channel of a MOSFET). Understanding this SFE differentiation may also lead to a better understanding of bonding at the atomic level.

Several techniques using IBA have been developed for the characterization of polymers. Further exploration needs to be done to refine and enhance these characterization tools.

REFERENCES

1. N. Herbots, J. D. Bradley, M. Hart, D. A. Sell, S. Whaley, and Q. Bradley, US patent application filed: Nov. 9, 2010, pending, M10-028P.

2. N. Herbots, J. D. Bradley, J. M. Shaw, R. J. Culbertson, and V. Atluri, US patent No. 7,851,365 (2010).

3. N. Herbots, R. J. Culbertson, J. Bradley, M. A. Hart, D. A. Sell, and S. Whaley, US patent application filed: April 30, 2009, pending, M9-035P.

4. R. Porter, Ophthalmology, 107 (4), 778-782 (2000).

5. Y. Yuriko, Japanese Journal of Ophthalmic Surgery, 18 (3), 383-386 (2005).

6. T. H. Levin, A New, Simple Technique to Prevent Water Condensation on Intraocular Lenses During Vitrectomy. NASA Technical Reports Server, Jet Propulsion Laboratory. NASA (2001).

7. Matticus78, File:Diagram of eye evolution.svg, Wikipedia, last updated Oct 27, 2006 http://en.wikipedia.org/wiki/File:Diagram_of_eye_evolution.svg Retrieved on March 6, 2011.

8. Permission granted under GNU Free Documentation License, Version 1.2 http://commons.wikimedia.org/wiki/Commons:GNU_Free_Documentation_License_1.2, Retrieved March 7, 2011.

9. National Eye Institute, Photos, Images and Videos, Last modified October 2010, Retrieved on March 10, 2011 from http://www.nei.nih.gov/photo/keyword.asp?match=any&conditions=Cataract&conditions=Normal+Eye+Images&conditions=Eye+Disease+Images&conditions=Surgery

10. National Eye Institute, Privacy Policy, Last modified October 2008, Retrieved on March 10, 2011 from http://www.nei.nih.gov/tools/policies.asp#copyright

11. D. A. Schaumberg, M. R. Dana, W. G. Christen, and R. J. Glynn, Ophthalmology, 105 (7), 1213-1221 (1998).

12. E. P. Steinberg, J. C. Javitt, P. D. Sharkey, A. Zuckerman, M. W Legro, G. F. Anderson, E. B. Bass, and D. O'Day, Archives of Ophthalmology, 111 (8), 1041-1049 (1993).

13. P. Ranta, P. Tommila, and T. Kivela, Journal of Cataract and Refractive Surgery, 30 (1), 58-66 (2004).

14. A. M. Eaton, G. J. Jaffe, B. W. McCuen II, and G. J. Mincey, Ophthalmology, 102 (5), 733-736 (1995).

15. D. P. Hainsworth, S. N. Chen, T. A. Cox, and G. J. Jaffe, Ophthalmology, 103 (9), 1410-1418 (1996).

16. D. J. Browning and C. M. Fraser, American Journal of Ophthalmology, 139 (4), 740-742 (2005).

17. D. Lee, M. F. Rubner and R. E. Cohen, Nano Letters, 6 (10), 2305-2312 (2006).

18. M. Ma and R. M. Hill, Journal of Colloid and Interface Science, 11, 193-202 (2006).

19. K. A. Wier and T. J. McCarthy, Langmuir, 22, 2433-2436 (2006).

20. A. Zdziennicka, K. Szymczyk, and B. Janczuk, J. of Colloid and Interface Science, 340, 243-248 (2009).

21. V. Atluri, Hydrogen Passivation of Silicon (100) Used as Templates for Low Temperature Epitaxy and Oxidation, Ph. D Dissertation, Arizona State University (1998).

22. Q. B. Hurst, Ordering at the Silicon (001) – Silicon Dioxide Interface as Studied by Ion Beam Analysis, Ph.D. Dissertation, Arizona State University (2000).

23. J. D. Bradley, A New Heteroepitaxial Silicon Dioxide Nanophase on OH-(1x1) Silicon (100) Identified via 3.05 MeV Ion Channeling and the New 3-D Multistring Code, Ph.D. Dissertation, Arizona State University (2006).

24. J. M. Shaw, Ordered Interfaces and Atomic Registry of Silicon(100) Surfaces and Silicon Dioxide, Ph.D. Dissertation, Arizona State University (2006).

25. M. Bjorkqvist, J. Paski, J. Solonen, and V. P. Lehto, IEEE Sensors Journal, 6 (3), 542-547 (2006).

26. N. Herbots, V. Atluri, J. Xiang, J. D. Bradley, S. Banerjee, and Q. B. Hurst, U.S. patent No. 6,613,677 (2003).

27. N. Herbots, J. M. Shaw, Q. B. Hurst, M. P. Grams, R. J. Culbertson, D. J. Smith, V. Atluri, P. Zimmerman, and K. T. Queeney, Materials Science and Engineering, B87, 303-316 (2001).

28. J. D. Bradley, A New Heteroepitaxial Silicon Dioxide Nanophase on OH – (1x1) Silicon (100) Identified via 3.05 MeV Ion Channeling and the New 3-D Multistring Code, Ph.D. Dissertation, Arizona State University (2006).

29. N. Herbots, J. D. Bradley, R. Culbertson, J. Shaw, and V. Atluri, Characterization of Oxide/Semiconductor Interfaces for CMOS Technologies, Edited by Y. Chabal, A. Esteve, N. Richard, and G. Wilk, Mater. Res. Soc. Symp. Proc. Volume 996E, Warrendale, PA, 2007, 0996-H05-13.

30. J. D. Bradley, N. Herbots, R. Culbertson, J. Shaw, and V. Atluri, Characterization of Oxide/Semiconductor Interfaces for CMOS Technologies, Edited by Y. Chabal, A. Esteve, N. Richard, and G. Wilk, Mater. Res. Soc. Symp. Proc. Volume 996E, Warrendale, PA, 2007, 0996-H05-14.

31. K. T. Queeney, N. Herbots, J. M. Shaw, V. Atluri, Y. J. Chabal, Appl. Phys. Lett., 84 (10), 493-495 (2004).

32. J. M. Shaw, N. Herbots, Q. B. Hurst, D. Bradley, R. J. Culbertson, and V. Atluri, J. of Appl. Phys., 100, 104109 (2006).

33. P. A. Levkin, F. Svec, and J. Frechet, Adv. Funct. Mater. 19 (12), 1993-1998 (2010).

34. D. Bozukova, C. Pagnoulle, M. C. De Pauw-Gillet, S. Desbrief, R. Lazzaroni, N. Ruth, R. Jerome, and C. Jerome, Biomacromolecules, 8, 2379-2387 (2007).

35. Y. Zhang, C. Y. Won, and C. C. Chu, Journal of Polymer Science: Part A, 37, 4554-4569 (1999).

36. P. Frantz and S. Granick, Langmuir, 8, 1179-118 (1992).

37. K. Furusawa, T. Dobashi, S. Morishita, M. Oyama, T. Hashimoto, N. Shinyashiki, S. Yagihara, and N. Nagasawa, Physica A, 353, 9-20 (2005).

38. N. Herbots, Q. Xing, M. Hart, J. D. Bradley, D. A. Sell, R. J. Culbertson, B. J. Wilkens, 2010 Proceedings of Nucl. Instr. and Meth. in Phys. Reseach B, IBMM 2010.

39. M. P. de Jong, L. J. van IJzendoorn, and M. J. A. de Voigt, Nucl. Instr. And Meth. In Phys. Research B.,161, 207-210 (2000).

40. T. Kaneko, M. Watamori, H. Makita, C. Araujo, and G. Kano, Nucl. Instr. And Meth. In Phys. Research B.,219-220, 236-240 (2004).

41. K. Furusawa, T. Dobashi, S. Morishita, M. Oyama, T. Hashimoto, N. Shinyashiki, S. Yagihara, and N. Nagasawa, Physica A, 353, 9-20 (2005).

42. A. Ben-Na'im, "Hydrophobic Interaction", Plenum Press : New York, pp301 (1980).

43. F. London, Z. Phys., 63, 245 (1930).

44. F. London, Trans. Faraday Soc., 33, 8 (1937).

45. R. H. French, K. I. Winey, M. K. Yang, and W. Qiu, Aust. J. Chem., 60, 251-263 (2007).

46. E. M. Lifshitz, Zh. Eksp. Teor. Fiz., 29, 94 (1955).

47. J. N. Israelachvili, "Intermolecular and Surface Forces". 2nd Edition. 1991, London: Academic Press

48. W. H. Keesom, Physikalishe Zeitschrift, 22, 643-644 (1921).

49. W. H. Keesom, Physikalishe Zeitschrift, 22, 129-141 (1921).

50. P. Debye, Physikalishe Zeitschrift, 21, 178-187 (1920).

51. P. Debye, Physikalishe Zeitschrift, 22, 302-308 (1921).

52. C. J. van OSS, "Interfacial Forces in Aqueous Media", 1994, NY: Marcel Dekker.

53. C. J. van Oss, M. K. Chaudhury, and R. J. Good, Chem. Rev., 88, 927-941 (1988).

54. J. F. Padday and N. D. Uffindell, Journal of Physical Chemistry, 72 (5), 1407-1414 (1968).

55. S. M. Rystov, Theory of Electric Fluctuations and Thermal Radiations, Moscow Academy and Science Press: Moscow, 1953.

56. J. N. Israelachvili, Quarterly Reviews of Biophysics, 6 (4), 341-387 (1974).

57. C. J. van OSS and R. F. Giese, "Colloid and Surface Properties of Clay and Related Minerals", (2002), New York: Marcel Dekker.

58. L. A. Grifalco and R. J. Good, Journal of Physical Chemistry, 61, 904-909 (1957).

59. F. M. Fowkes, Journal of Physical Chemistry, 67, 2538-2541 (1963).

60. F. M. Fowkes, “Physicochemical Aspects of Polymer Surfaces”, Ed. K. L. Mittal, 2, 583, New York: Plenum Press (1983).

61. F. M. Fowkes and M. A. Mostafa, Industrial and Engineering Chemistry Research – Product Research and Development, 17 (1), 3-7 (1978).

62. Maňas, M. , File:3D model hydrogen bonds in water.jpg, Wikipedia, last updated Dec 3, 2007, http://en.wikipedia.org/wiki/File:3D_model_hydrogen_bonds_in_water.jpg Retrieved on March 7, 2011.

63. M. K. Chaudhury, Short Range and Long Range Forces in Colloidal and Macroscopic Systems, Ph.D. Dissertation, SUNY: Buffalo (1984).

64. International Union of Pure and Applied Chemistry (IUPAC). Chemical Compendium of Terminology, 2nd Ed. Eds A. D. McNaught and A. Wilkinson. Blackwell Scientific Publications: Oxford (1997).

65. H. Gouin, J. Phys. Chem. B, 102 (7), 1212-1218 (1998).

66. A. Carre, J. Adhesion Sci. Technol., 21 (10), 961-981 (2007).

67. J. E. McDonald, American Journal of Physics, 30(12), 870-877 (1962).

68. J. E. McDonald, American Journal of Physics, 31(4), 31-41 (1963).

69. U. Devgan, Understanding and Using the Full Spectrum of OVDs. Review of Ophthalmology, 16 (4) (2009).

70. M. T. Sykes and M. Levitt, Proceedings of the National Academy of Sciences, 104 (30), 12336-12340 (2007).

71. Permission granted under the Rights and Permissions, Copyright and License to Publish of the Proceedings of the National Academy of Sciences of the United States of America, last updated July 2010, Copyright 2011 by National Academy of Sciences http://www.pnas.org/site/misc/rightperm.shtml Retrieved March 7, 2011.

72. P. J. Mills, P. F. Green, C. J. Palmstrom, J. W. Mayer, and E. J. Kramer, Appl. Phys. Lett., 45 (9), 957-959 (1984).

73. R. de Bettignies, J. Leroy, M. Firon, C. Sentein, S. Bailly and S. Guillerez, “Ageing Process in Organic Photovoltaic Solar Cell: Accelerated Lifetime and RBS Measurements”, European Conference on Hybrid and Organic Solar Cells (2006).

74. M. Parizek, N. Kasalkova, L. Bacakova, P. Slepicka, V. Lisa, M. Blazkova, and V. Svorcik, Int. J. Mol. Sci., 10, 4352-4374 (2009).

75. A. J. Morse, S. Edmondson, D. Dupin, S. P. Armes, Z. Zhang, G. J. Leggett, R. I. Thompson, and A. L. Lewis, Soft Matter, 6, 1571-1579 (2010).

76. R. J. Culbertson and B. J. Wilkens, Short Course on Ion Beam Analysis, Tempe: Arizona State University, 2009, pp. 166.

77. J. W. Mayer and E. Rimini, Ion Beam Handbook for Material Analysis, Academic Press, New York (1977).

78. J. A. Leavitt, L. C. McIntyre, Jr., P. Stoss, J. G. Oder, M. D. Ashbaugh, B. Dezfouly-Arjomandy, Z. M. Yang, and Z. Lin, Nucl. Instr. And Meth. In Phys. Research B. 40/41 776-779 (1989).

79. J. A. Leavitt, L. C. McIntyre, Jr., M. D. Ashbaugh, J. G. Oder, Z. Lin, and B. Dezfouly-Arjomandy, Nucl. Instr. And Meth. In Phys. Research B. 44 260-265 (1990).

80. L. C. Feldman, J. W. Mayer, and S. T. Picraux, Materials Analysis by Ion Channeling – Submicron Crystallography, Academic Press, NY, (1982).

81. V. L. Levshunova, G. P. Pokhil, D. I. Tetel'baum, and P. N. Chernykh, Journal of Surface Investigation. X-Ray, Synchrotron, and Neutron Techniques, 4, 515-517 (2010).

82. W. A. Lanford, Nucl. Instr. and Meth. in Phys Research B, 66, 65-82 (1992).

83. B. J. Wilkens, Materials Characterization by Ion Beam Analysis, Internal Report, Center for Solid State Science, Arizona State University, Tempe, Arizona.

84. J. L'Ecuyer, et al., Journal of Applied Physics, 47 (1), 381 (1976).

85. B. L. Cohen, et al., Journal of Applied Physics, 43 (1), 19 (1972).

86. H. Salah and B. Touchrift, Radiation Effects and Defects in Solids, 159, 181-194 (2004).

87. V. Atluri, N. Herbots, D. Dagel, S. Bhagvat, and S. Whaley, Nucl. Instr. and Meth. in Phys. Research B, 118, 144-150 (1996).

88. F. L. Martinez, M. Toledano, E. San Andres, I. Martil, G. Gonzalez-Diaz, W. Bohne, J. Rohrich, and E. Strub, Thin Solid Films, 515, 695-699 (2006).

89. W. Bohne, W. Fuhs, J. Rohrich, B. Selle, I. Sieber, A. del Prado, E. San Andres, I. Martil, and G. Gonzalez-Diaz, Surface and Interface Analysis, 34, 749-753 (2002).

90. Z. Hulek, Z. Cespiro, R. Salomonovic, M. Setvak, and J. Voltr, Vacuum, 41, 1853-1855 (1990).

91. M. P. de Jong, L. J. van IJzendoorn, and M. J. A. de Voigt, Nucl. Instr. And Meth. In Phys. Research B.,161, 207-210 (2000).

92. W. Bohne, W. Fuhs, J. Rohrich, B. Selle, I. Sieber, A. del Prado, E. San Andres, I. Martil, and G. Gonzalez-Diaz, Surface and Interface Analysis, 34, 749-753 (2002).

93. N. Herbots, V. Atluri, Q. Hurst, J. M. Shaw, S. Banerjee, J. D. Bradley, R. J. Culbertson, and D. J. Smith, Materials Research Society Symp. Proc., 510, 157 (1999).

94. K. Saravanan, B. K. Panigrahi, S. Amirthapandian, and K. G. M. Nair, Nucl. Instr. And Meth. In Phys. Research B., 266 1502-1506 (2008).

95. Q. Xing, N. Herbots, M. Hart, J. D. Bradley, B. J. Wilkens, D. A. Sell, C. Sell, H. M. Kwong, Jr., R. J. Culbertson, S. D. Whaley. CAARI 2010 to be published.

96. P. Trouslard, S. Pellegrino, and L. Beck, Nucl. Instr. and Meth. in Phys. Research B. 240 381-385 (2005).

97. T. Lowe, Q. Chen, Q. Fernando, R. Keith, and A. Gandolfi, Environmental Health Perspectives, 101 (4) 302-308 (1993).

98. N. D. Skelland, Nucl. Inst. and Meth. in Phys. Research B., 84 361-367 (1994).

99. J. H. Arps and R. A. Weller, Nucl. Instr. and Meth. in Phys. Research B, 79, 539-544 (1993).

100 W. A. Lanford, Nucl. Instr. and Meth. in Phys. Research B, 66 65-82 (1992).

101. V. Darakchieva, K. Lorenz, N. P. Barradas, E. Alves, B. Monemar, M. Schubert, N. Franco, C. L. Hsiao, L. C. Chen, W. J. Schaff, L. W. Tu, T. Yamaguchi, and Y. Nanishi, Applied Physics Letters, 96 (8) 081907 (2010).

102. R. D. Verda, C. J. Maggiore, J. R. Tesmer, A. Misra, T. Hoechbauer, M. Nastasi, and R. W. Bower, Nucl. Instr. and Meth. in Phys. Research B, 183, 401-412 (2001).

103. F. L. Martinez, M. Toledano, E. San Andres, I. Martil, G. Gonzalez-Diaz, W. Bohne, J. Rohrich, and E. Strub, Thin Film Solids, 515, 695-699 (2006).

104. L. R. Doolittle, Nucl. Instr. and Meth. in Phys. Research B, 9, 344-351 (1985)

105. B. Nsouli, M. Roumie, K. Zahraman, J. P. Thomas, M. Jaksic, Z. Pastuovic, P. Dole and M. Nasredine, Nucl. Instr. And Meth. In Phys. Research B, 198, 201-207 (2002).

106. E. A. Preoteasa, C. Ciortea, B. Constantinescu, D. Fluerasu, S. E. Enescu, D. Pantelica, F. Negoita and E. Preoteasa, Nucl. Instr. And Meth. In Phys. Research B, 189, 426-430 (2002).

107. H. Kabir, "Particle Induced X-ray Emission (PIXE) Setup and Quantitative Elemental Analysis", Ph.D. Dissertation, Kochi University of Technology, 2007.

108. J. L. Campbell, G. K. Czamanske, L. MacDonald, and W. J. Teesdale, Nucl. Instr. and Meth. in Phys. Research B, 130, 608-616 (1997).

109. Q. Xing, M. A. Hart, R. J. Culbertson, J. D. Bradley, N. Herbots, B. J. Wilkens, D. A. Sell, and C. F. Watson, Accepted for publication in the 2010 21st International Conference on the Application of Accelerators in Research and Industry (CAARI 2010) Proceedings.

110. G. Demortier and J. L. Ruvalcaba-Sil, Nucl. Instr. and Meth. in Phys. Research B, 118, 352-358 (1996).

111. G. Demortier, S. Mathot, and B. Van Oystaeyen, Nucl. Instr. and Meth. in Phys. Research B, 49, 46-51 (1990).

112. I. Brissaud, J. P. Frontier, and P. Regnier, Nucl. Instr. and Meth. in Phys. Research B, 12, 235-244 (1985).

113. J. Miranda, Nucl. Instr. and Meth. in Phys. Research B, 118, 346-351 (1996).

114. H. C Kaufmann and J. Steenblik, Nucl. Instr. and Meth. in Phys. Research B, 3, 198-202 (1984).

115. G. Demortier, S. Mathot, and B. Van Oystaeyen, Nucl. Instr. and Meth. in Phys. Research B, 49, 46-51 (1990).

116. W. J. Teesdale, J. A. Maxwell, A. Perujo, J. L. Campbell, L. Van der Zwan, and T. E. Jackman, Nucl. Instr. and Meth. in Phys. Research B, 35, 57-66 (1988).

117. J. A. Maxwell, J. L. Campbell, and W. J. Teesdale, Nucl. Instr. and Meth. in Phys. Research B, 43, 218-230 (1989).

118. R. S. Faibish, J. Colloid and Interface Sci., 256, 341-350 (2002).

119. C. Della Volpe and S. Siboni, Calculations of Acid base Surface Tension Components: SurfTen 4.3, University of Italy, 2004: Retrieved from the Internet on July 28, 2010 from http://devolmac.ing.unitn.it:8080/mathpad4.html

120. C. Della Volpe, D. Maniglio, M. Brugnara, S. Siboni, and M. Morra, Nucl. Instr. And Meth. In Phys. Research B, 271, 434-453 (2004).

121. P. E. Luner, E. Oh, Colloids and Surfaces A: Physicochemical and Engineering Aspects, 181, 31-48 (2001).

122. E. Rame, J. Colloid and Interface Sci., 185 (1), 245-251 (1997).

123. Diversified Enterprises, Critical Surface Tension and Contact Angle with Water for Various Polymers (2009).

124. S. N. Magonov and D. H. Reneker, Annual Review of Material Science, 27, 175-222 (1997).

125. G. Binnig, c. F. Quate, and Ch. Gerber, Phys. Rev. Lett., 56 (9), 930-933 (1986).

126. R. F. M. Lobo, M. A. Pereira-da-Silva, M. Raposo, R. M. Faria, and O. N. Oliveira Jr., Nanotechnology, 14, 101-108 (2003).

127. G. Binning, H. Rohrer, C. Gerber, and E. Weibel, Phys. Rev. Lett., 50, 120-123 (1983).

128. H. K. Wickramasinghe, Scientific American, 10, 98-105 (1989).

129. H. K. Wickramasinghe, J. Vac. Sci. Technol. A, 8 (1), 363-368 (1990).

130. Digital Instruments, Atomic Force Microscopy, A Current Perspective, Digital Instruments Nanotips, Journal for Nanoscope Users, 5 (1). Editor M. Thompson, Published by Digital Instruments, Inc., Santa Barbara, CA.

131. C. B. Prater, Y. E. Strausser, Defect Recongnition and Image Processing in Semiconductors and Devices, Institute of Physics Conference Series, 135, 69-72 (1994).

132. Y. Martin, C. C. Williams, and H. K. Wickramasinghe, Journal of Applied Physics, 61 (10), 4723-4729 (1987).

133. B. Drake, C. B. Prater, A. L. Weisenhorg, S. A. C. Gould, T. R. Albrecht, C. F. Quate, et al., Science, 243 (4898), 1586-1589 (1989).

134. C. B. Prater and Y. E. Strausser, Tapping Mode Atomic Electron Microscopy – Applications to Semiconductor, Technical Note, Digital Instruments, Inc., Santa Barbara, CA

135. C. B. Prater, P. G. Maivald, K. J. Kjoller and M. G. Heaton, TappingMode™ Imaging – Applications and Technology, Technical Note, Digital Instruments, Inc., Santa Barbara, CA.

136. P. Klapetek, D. Necas, and C. Anderson. Gwyddion User Guide. Version 2009-11-11. GNU Free Press.

137. M. Raposo, Q. Ferreira, and P. A. Ribeiro. "A Guide for Atomic Force Microscopy Analysis of Soft-Condensed Matter." Modern Research and Educational Topics in Microscopy. Vol.1, 1st Ed. A. Mendez-Vilas and J. Diaz. Badajoz, Spain: Formatex Research Institute, 2007. 758-769.

138. J. K. Lawson, C. R. Wolfe, K. R. Manes, J. B. Trenholme, D. M. Aikens, and R. E. English Jr., "Specification of Optical Components Using the Power Spectral Density Function.", Eds Proc. SPIE 2536 (38) (1995).

139. W. Chen, H. Yao, F. Wu, S. Wu, and Q. Chen, Front. Optoelectron. China., 1 (1-2), 197-200 (2008).

140. A. L. Schmadel, Power S pectral Analysis of Niobium Surfaces, Undergraduate Dissertation, The College of William and Mary (2009).

141. P. E. Luner and E. Oh, Colloids and Surfaces A: Physicochem. Eng. Aspects, 181, 31-48 (2001).

142. P. K. Narayanan, E. H. Goodwin, and B. E. Lehnert, Cancer Research, 57, 3963-3971 (1997).

143. N. Bhat, A. W. Wang, and K. C. Saraswat, IEEE Transactions on Electron Devices, 46 (1), 63-69 (1999).

144. P. K. Sharma and K. H. Rao, Advances in Colloid and Interface Science, 98, 341-463 (2002).

APPENDIX A

GLOSSARY OF ACRONYMS

AB	Acid Base
AFM	Atomic Force Microscopy
DI	Deionized
ERD	Elastic Recoil Detection
HPMC	Hydroxypropyl Methylcellulose
IBA	Ion Beam Analysis
IBMM	Ion Beam Modification of Materials
IOL	Intraocular Lens
LW	Lifshitz-van der Waals
PDMS	Polydimethylsiloxane
PIXE	Particle Induced X-ray Emission
PSDF	Power Spectral Density Function
RBS	Rutherford Backscattering Spectrometry
RMS	Root Mean Square
SFE	Surface Free Energy
TMAFM	Tapping Mode Atomic Force Microscopy